PACIFIC EARTHQUAKE ENGINEERING
RESEARCH CENTER

The 21st Working Conference of the IFIP Working Group 7.5 on Reliability and Optimization of Structural Systems (IFIP WG7.5 2024)

Ziqi Wang and Jungho Kim

Department of Civil and Environmental Engineering
University of California, Berkeley, California

PEER Report No. 2024/10
Pacific Earthquake Engineering Research Center
Headquarters at the University of California, Berkeley
August 2024

PEER 2024/10
August 2024

The 21st Working Conference of the IFIP Working Group 7.5 on Reliability and Optimization of Structural Systems (IFIP WG7.5 2024)

August 19-21, 2024

University of California, Berkeley, USA

Edited by Ziqi Wang and Jungho Kim

PEER Report No. 2024/10
Pacific Earthquake Engineering Research Center
Headquarters, University of California, Berkeley
August 2024

PREFACE

These are the proceedings of the twenty-first working conference of the International Federation of Information Processing (IFIP) Working Group 7.5 on Reliability and Optimization of Structural Systems, which took place at the University of California, Berkeley, USA, on August 19–21, 2024. This volume contains 15 selected papers from the 20 presentations delivered at the conference.

The conference was supported by Pacific Earthquake Engineering Research (PEER) Center, and by the University of California, Berkeley, which provided outstanding facilities in the conference venue and remarkable logistic support throughout the event.

The purpose of the WG7.5 Working Group is to promote modern theories and methods of structural and system reliability and optimization, to stimulate research, development, and applications in these areas, to foster the dissemination and exchange of information, and to encourage education on those subjects.

The main themes of the conference included structural reliability methods, engineering risk and re-silience analysis, Bayesian methods, reliability-based design optimization, and sensitivity analysis, along with their applications in civil engineering, dynamics, and natural hazards. The conference facilitated engaging discussions among participants, both during and after the technical sessions. Notably, a significant number of presentations were delivered by promising young researchers, who contributed fresh perspectives and innovative ideas to the field.

We are grateful to all the participants for their valuable contributions and active engagement, which made the conference a successful and memorable event. We also extend our thanks to the organiz-ing committee, the scientific committee, and all those who contributed to the smooth execution of the conference.

We look forward to future IFIP WG7.5 conferences and continued collaboration in advancing the field of structural reliability and optimization.

Ziqi Wang and Jungho Kim
May 6th, 2025

SCIENTIFIC COMMITTEE

Armen Der Kiureghian	University of California, Berkeley, USA
Marco Broccardo	University of Trento, Italy
Paolo Gardoni	University of Illinois at Urbana-Champaign, USA
Terje Haukaas	The University of British Columbia, Canada
Chul-Woo Kim	Kyoto University, Japan
Iason Papaioannou	Technical University of Munich, Germany
Kostas Papakonstantinou Matteo	The Pennsylvania State University, USA
Pozzi	Carnegie Mellon University, USA
Junho Song	Seoul National University, Republic of Korea
Seymour Spence	University of Michigan, USA
Daniel Straub	Technical University of Munich, Germany
Bruno Sudret	ETH Zurich, Switzerland

ORGANIZING COMMITTEE

Ziqi Wang (Chair)
Khalid Mosalam
Amarnath Kasalanati
Zulema Lara
Christina Bodnar-Anderson
Erika Donald
Gabriel Vargas

PREVIOUS PROCEEDINGS

Results from previous conferences have been published in the following proceedings:

1. Reliability and Optimization of Structural Systems, 1987. Proc. of the first IFIP WG 7.5 Working Conference, Aalborg, Denmark, May. 6-8, 1987 (Ed. P. Thoft-Christensen).Lecture Notes in Engineering, Vol.33, Springer-Verlag, Berlin Heidelberg New York.

2. Reliability and Optimization of Structural Systems, 1988. Proc. of the second IFIP WG 7.5 Working Conference, London, UK, Sept. 26-28, 1988 (Ed. P. Thoft-Christensen). Lecture Notes in Engineering, Vol.48, Springer-Verlag, Berlin Heidelberg New York.

3. Reliability and Optimization of Structural Systems, 1990. Proc. of the third IFIP WG 7.5 Working Conference, Berkeley, California, USA, Mar. 26-27, 1990 (Eds. A. Der Kiureghian & P. Thoft-Christensen). Lecture Notes in Engineering, Vol.61, Springer-Verlag, Berlin Heidelberg New York.

4. Reliability and Optimization of Structural Systems, 1991. Proc. of the fourth IFIP WG 7.5 Working Conference, Munich, Germany, Sept. 11-13, 1991 (Eds. R. Rackwitz & P. Thoft-Christensen). Lecture Notes in Engineering, Vol. 76, Springer-Verlag, Berlin Heidelberg New York.

5. Reliability and Optimization of Structural Systems, 1993. Proc. of the fifth IFIP WG 7.5 Working Conference, Takamatsu, Kagawa, Japan, Mar. 22-26, 1993 (Eds. P. Thoft-Christensen & H. Ishikawa). IFIP Transactions B-12, Applications in Technology, Elsevier Science Publishers B.V., Amsterdam.

6. Reliability and Optimization of Structural Systems, 1994. Proc. of the sixth IFIP WG 7.5 Working Conference, Assissi, Italy, Sept. 7-9, 1994 (Eds. R. Rackwitz, G.Augusti & A. Bori). Chapman & Hall, London.

7. Reliability and Optimization of Structural Systems, 1996. Proc. of the seventh IFIP WG 7.5 Working Conference, Boulder, Colorado, USA, April 2-4, 1996 (Eds. D. M. Frangopol, R. B. Corotis & R. Rackwitz). Pergamon, Elsevier.

8. Reliability and Optimization of Structural Systems, 1998. Proc. of the eighth IFIP WG 7.5 Working Conference, Krakow, Poland, May 11-13, 1998 (Eds. A. S. Nowak & M. M. Szerszen), Univ. of Michigan, Ann Arbor, MI, USA.

9. Reliability and Optimization of Structural Systems, 2000. Proc. of the ninth IFIP WG 7.5 Working Conference, University of Michigan, Ann Arbor, Sept. 25-27, 2000 (Eds. A. S. Nowak & M. M. Szerszen), Univ. of Michigan, Ann Arbor, MI, USA.

10. Reliability and Optimization of Structural Systems, 2002. Proc. of the tenth IFIP WG 7.5 Working Conference, Kansai University, Osaka, Japan, Mar. 25-27, 2002 (Eds. H. Furuta, M. Dogaki & M. Sakano), A. A. Balkema Publishers.

11. Reliability and Optimization of Structural Systems, 2003. Proc. of the eleventh IFIP WG7.5 Working Conference, Banff, Canada, Nov. 2-5, 2003 (Eds. M. A. Maes & L. Huyse), A. A. Balkema Publishers.

12. Reliability and Optimization of Structural Systems, 2005. Proc. of the twelfth IFIP WG 7.5 Working Conference, Aalborg, Denmark, May 2-25, 2005 (Eds. J. D. Sorensen & D. M. Frangopol), A. A. Balkema Publishers.

13. Reliability and Optimization of Structural Systems, 2006. Proc. of the thirteenth IFIP WG 7.5 Working Conference, Kobe, Japan, Oct. 12-14, 2006 (Eds. J. D. Sorensen & D. M. Frangopol), A. A. Balkema Publishers.

14. Reliability and Optimization of Structural Systems, 2008. Proc. of the fourteenth IFIP WG7.5 Working Conference, Toluca, Mexico, August 6-9 2008, CD ROM, Compiler: Luis Esteva.

15. Reliability and Optimization of Structural Systems, Proc. of the fifteenth IFIP WG 7.5 Working Conference, TUM, Munich, Germany, April 7-10, 2010 (Ed. D. Straub), CRC press, ISBN:978-0-415-88179-1.

16. Reliability and Optimization of Structural Systems, Proc. of the sixteenth IFIP WG 7.5 Working Conference, Yerevan, Armenia, June 24-27, 2012 (Eds. Der Kiureghian & Hajian), ISBN: 978-0-9657429-0-0.

17. Reliability and Optimization of Structural Systems, Proc. of the seventeenth IFIP WG 7.5 Working Conference, Huangshan, China, July 3-7, 2014 (Eds. Y. Zhao, J. Li & Z. Lu), ISBN: 978-7-03-044789-0.

18. Reliability and Optimization of Structural Systems, Proc. of the eighteenth IFIP WG 7.5 Working Conference, Carnegie Mellon University, PA, USA, May 18-20, 2016. (Eds. M. Pozzi, J. Bielak, D. Straub).

19. Reliability and Optimization of Structural Systems, Proc. of the nineteenth IFIP WG 7.5 Working Conference, ETH Zurich, Switzerland, June 26-29, 2018. (Eds. Eds. B. Sudret & S. Marelli), ISBN: 978–3–906916–56–9.

20. Reliability and Optimization of Structural Systems, Proc. of the twentieth IFIP WG 7.5 Working Conference, Kyoto University, Japan, September 19-20, 2022. (Eds. C.W. Kim & K.C. Chang)

Participants of the 21st IFIP WG7.5 Conference at UC Berkeley, USA

Participants of the 21st IFIP WG7.5 Conference at UC Berkeley, USA

Participants of the 21st IFIP WG7.5 Conference at UC Berkeley, USA

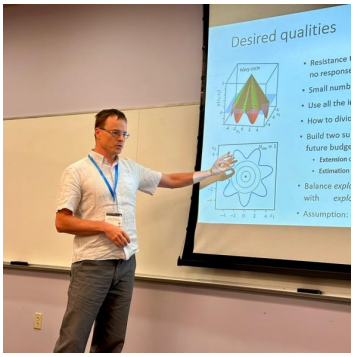

Participants of the 21st IFIP WG7.5 Conference at UC Berkeley, USA

Participants of the 21st IFIP WG7.5 Conference at UC Berkeley, USA

Participants of the 21st IFIP WG7.5 Conference at UC Berkeley, USA

CONTENTS

Addressing correlation in stochastic emulation of seismic response

Sang-ri Yi
Department of Civil & Environmental Engineering, University of California, Berkeley, United States

Alexandros A. Taflanidis
Department of Civil & Environmental Engineering & Earth Sciences, University of Notre Dame, Notre Dame, United States

ABSTRACT

Stochastic emulation techniques are used to surrogate forward simulations involving non-deterministic input-output relationships. Their objective is to address the stochastic uncertainty sources by directly predicting the output distribution for a given parametric input. An example of such application, and the focus of this contribution, is the estimation of structural response (engineering demand parameter) distribution in seismic risk assessment. In this case, the stochastic uncertainty originates from the aleatoric variability in the seismic hazard description. The key challenge in stochastic emulation pertains to addressing heteroscedasticity in the output variability. Relevant approaches to-date for addressing this challenge have focused on scalar outputs. In contrast, this paper focuses on the multi-output stochastic emulation problem and presents a methodology for predicting the output correlation matrix, while fully addressing heteroscedastic characteristics. This is achieved by introducing a Gaussian Process (GP) regression model for approximating the components of the correlation matrix, and coupling this approximation with a correction step to guarantee positive definite properties for the resultant predictions. For obtaining the observation data to inform the GP calibration, different approaches are examined, relying-or-not on the existence of replicated samples for the response output. When available, replicated samples can be readily used to obtain observation for the response statistics (correlation or covariance) to inform the GP development. An alternative approach is to obtain noisy observations of covariance using the sample deviations from a primitive mean approximation. These different observation variants lead to different GP variants that are compared within a comprehensive case study. A computational framework for integrating the correlation matrix approximation within the stochastic emulation for the marginal distribution approximation of each output component is also discussed, to provide the joint response distribution approximation.

1 INTRODUCTION

Surrogate models, also referred to as metamodels or emulators, have shown great promise in improving accuracy of risk assessment for many natural hazards engineering applications (Jung et al., 2023, Li and Spence, 2023, Cabanzo et al., 2023), especially in the field of seismic vulnerability estimation (Kim et al., 2023, Gidaris et al., 2015, Zhu et al., 2023, Ning et al., 2024, Gentile and Galasso, 2022). This estimation needs to consider various types of uncertainties for the seismic hazard and the infrastructure models (Baker and Cornell, 2008), while for improved accuracy, it should be based on nonlinear response history analysis (NLRHA) utilizing high-fidelity finite element models (Goulet et al., 2007, Haselton et al., 2008). Surrogate models can efficiently reduce the cost of utilizing NLRHA within seismic risk assessment by establishing a data-driven approximation for the structural response, developed using a small number of judicially chosen simulations. However, an important challenge in establishing this approximation (Gidaris et al., 2015) is the treatment of the aleatoric variability

associated with the seismic hazard description. This variability in hazard is typically expressed as a combination of parametric uncertainty and high-dimensional or non-parametric uncertainty (Jalayer et al., 2012, Baker and Cornell, 2008, McGuire, 2004), and the latter poses challenges to conventional surrogate modeling techniques (Gramacy, 2020). Essentially, the prediction of structural response, given all parametric inputs, becomes non-deterministic. Such non-deterministic simulation models are encountered in multiple engineering applications and have incentivized specialized surrogate modeling techniques called *stochastic emulation* (Baker et al., 2022, Ankenman et al., 2008, Zhu and Sudret, 2021, Binois et al., 2019), which aim to approximate the distribution of the output for a given simulation input. A key challenge in stochastic emulation is how to efficiently establish heteroscedastic predictions for the distribution parameters describing the stochastic output variability (Binois et al., 2018, Zhu and Sudret, 2021). Multiple variants have been proposed to accomplish this objective, however, existing stochastic emulation frameworks have predominantly focused on scalar response outputs.

This paper revisits the multi-output stochastic emulation problem and presents a methodology for predicting the output correlation matrix, while fully addressing heteroscedastic characteristics. This is achieved by introducing a GP regression model for approximating the components of the correlation matrix and introducing a correction for achieving positive-definite predictions, whereas a parallel GP calibration (Gu and Berger, 2016) is promoted to minimize the instances for having to deploy this correction. Different variants are examined for the problem formulation, relying or not on the existence of replication data. It is also shown how the established correlation predictions can be subsequently combined with existing stochastic emulation approaches for approximating the marginal distribution of each output component to characterize the joint distribution of the output vector. Though the developments are general and can, in principle, be applied to any stochastic emulation problem, they are couched within a specific application of interest: the approximation of the engineering demand parameter (EDP) joint distribution for seismic risk assessment.

2 PROBLEM FORMULATION FOR MULTI-OUTPUT STOCHASTIC EMULATION AND CONNECTION TO SEISMIC EDP DISTRIBUTION APPROXIMATION

Let $\mathbf{z} \in \mathbb{R}^{n_z}$ denote the n_z dimensional output of a stochastic computer simulation model $\mathbf{z} = \mathbf{F}(\mathbf{x};\mathbf{w})$, where $\mathbf{x} \in \mathbb{R}^{n_x}$ denote the n_x dimensional input vector, and $\mathbf{w}$ represent the source of stochastic randomness in the simulation model. Note that depending on the application of interest, $\mathbf{w}$ may represent high-dimensional or non-parametric uncertainties impacting the simulation model (Kyprioti and Taflanidis, 2022, Baker et al., 2022). The objective is to establish an approximation for the joint distribution of $\mathbf{z}$ as a function of $\mathbf{x}$ under the influence of the randomness described by $\mathbf{w}$. This distribution is characterized herein by the probability density function $p(\mathbf{z}|\mathbf{x})$. Subscript l will be used to distinguish the different components of a vector, with $z_l \in \mathbb{R}$ representing the lth response output.

For seismic risk assessment applications, the output vector $\mathbf{z}$ corresponds to the engineering demand parameters (EDPs) of interest, and the simulation model to NLRHA performed for a specific structural model using some ground motion representing the seismic hazard. The stochastic randomness in the simulation outcome originates from the aleatoric randomness in the description of this hazard. The uncertainties associated with this hazard can be broadly divided into two classes (Baker and Cornell, 2008). The first class pertains to key seismicity characteristics (such as moment magnitude) and/or ground motion features (such as arias intensity and significant duration). This class represents the parametric explanatory input variables that may be used to describe the dominant hazard features, and are included in input vector $\mathbf{x}$. The second class originates from the complex physical mechanism in propagation/generation of earthquakes, which precludes the complete description of the seismic excitation through the parametrized explanatory variables (Jalayer et al., 2012, Baker and Cornell, 2008, McGuire, 2004). Depending on the modeling approach for describing the seismic excitation (Jalayer and Beck, 2008), it might correspond to latent features of the excitation model, or to a high-dimensional stochastic sequence. Ultimately, this uncertainty class needs to be treated as inherent randomness in the simulation model output given the values of the seismic hazard explanatory variables. Note that the

structural model utilized within the NLRHA might have its own uncertain parameters, such as material and geometric properties (Gentile et al., 2021, Kazantzi et al., 2014), that need to be additionally used as input variables and included in $\mathbf{x}$. The objective of the stochastic emulation in this context is to establish a mapping between all the explanatory variables, i.e. seismicity features and structural parameters, and the EDP distribution of a target structure $p(\mathbf{z}|\mathbf{x})$, where the distribution represents the aleatoric uncertainties (Kyprioti and Taflanidis, 2021, Zhu et al., 2023).

The stochastic emulator problem in this setting can be formally defined as follows. A database of observations is first developed by performing simulations for N_t different input configurations $\{\mathbf{x}^i; i=1,...,N_t\}$, representing the emulator training points. The training points should cover the entire input domain, denoted as X herein, where the surrogate model is anticipated to be used for, so that any extrapolations are avoided. For each training point, the response prediction (computer simulation) is repeated a total of n^i times yielding observations $\{\mathbf{z}^{i(k)}; k=1,..,n^i\}$. The n^i replications of the output are obtained for the same input $\mathbf{x}^i$ utilizing different realizations for the stochastic random vector $\mathbf{w}$. For example, for seismic risk assessment applications utilizing stochastic ground motion models, these realizations correspond to acceleration time-histories obtained from different stochastic sequences (Kyprioti and Taflanidis, 2021). Herein, superscripts will be used to distinguish the training points, and superscripts in parenthesis will be used to distinguish the replications. Following Kyprioti and Taflanidis (2021) and Yi and Taflanidis (2024), let us consider a special configuration of partially replicated training set, where first N_r training points have n_r replications ($n^i = n_r$ for $i \le N_r$) and remaining N_n=N_t -N_r training points are non-replicated samples (n^i=1 for $N_r < i \le N_t$). The set of training points for which replications are available will be denoted as $\mathbf{X}_p$. The total number of high-fidelity simulations for the stochastic emulation training is $N_{sim} = n_r N_r + N_n$. The objective of stochastic emulation is to establish an approximation for $p(\mathbf{z}|\mathbf{x})$ using database consisting of input $\{\mathbf{x}^i; i=1,...,N_t\}$ and output $\{\mathbf{z}^{i(k)}; k=1,..,n^i,\ i=1,...,N_t\}$.

3 REVIEW OF GP-BASED STOCHASTIC EMULATION OF THE MARGINAL DISTRIBUTION FOR EACH OUTPUT COMPONENT

The foundation of the GP-based stochastic emulation for approximating distribution $p(z_l|\mathbf{x})$ is the approximation of the chosen response as a realization of a Gaussian process. Instead of approximating directly the response output z_l some transformation can be applied, for example, by setting $y_l = \ln(z_l)$. The latter transformation is recommended for earthquake engineering applications (Kyprioti and Taflanidis, 2021) as it agrees with the lognormal assumption for $p(z_l|\mathbf{x})$ shown to be accurate for many cases (Baker and Cornell, 2008). The underlying GP has some mean trend function over $\mathbf{x}$ - typically expressed by a vector of basis functions $\mathbf{f}(\mathbf{x})$ and their regression coefficients $\boldsymbol{\beta}$ - and stationary auto-covariance model denoted as $\tilde{\sigma}^2 R(\mathbf{x},\mathbf{x}'|\boldsymbol{\theta})$ with kernel parameters $\boldsymbol{\theta}$ and process variance $\tilde{\sigma}^2$ (Gramacy, 2020, Rasmussen and Williams, 2005). Leveraging the so-called nugget (Gramacy and Lee, 2012, Yin et al., 2011) to establish a regression over the training data and address the aleatoric randomness, the stochastic emulation model yields the following distribution approximation (Kyprioti and Taflanidis, 2021)

$$\tilde{p}(y_l|\mathbf{x}) = \mathcal{N}(\tilde{y}_l(\mathbf{x}), \sigma_l^2(\mathbf{x}) + \tau_l^2(\mathbf{x})) \tag{1}$$

where $\mathcal{N}(a,b)$ stands for a Normal distribution with mean a and variance b, $\tilde{y}_l(\mathbf{x})$ and $\sigma_l^2(\mathbf{x})$ represent the predictive mean and variance for the GP, and $\tau_l^2(\mathbf{x})$ represents the stochasticity variance (i.e. nugget variance). It is important to stress that the last function, $\tau_l^2(\mathbf{x})$, is the component that describes the stochasticity in the model output. When this stochasticity is assumed to be constant, i.e., when $\tau_l^2(\mathbf{x}) = \tau_l^2$, the problem is reduced to the simpler homoscedastic case, and the GP calibration can be performed straightforwardly using directly the training points. For the case of interest, which is the heteroscedastic formulation, additional care is needed to obtain observations for $\tau_l^2(\mathbf{x})$ to guide the stochastic emulation calibration. Such observations can be obtained based on the sample variance established through replication samples (Ankenman et al., 2008, Kyprioti and Taflanidis, 2021) or the sample deviation

established through some primitive mean approximation (Marrel et al., 2012, Yi and Taflanidis, 2024). These two variant implementations, which will be revisited for the covariance elements in Section 4, will be distinguished by acronyms *RV* (replication statistics) and *SD* (sample deviation statistics) herein.

In the *RV* formulation, unbiased estimates for the sample variance are obtained using the training points with replications ($\mathbf{X}_p$), as:

$$(\bar{\tau}_l^2)^i = \frac{1}{n_r - 1}\sum_{k=1}^{n_r}(y_l^{i(k)} - \bar{y}_l^i)^2, \qquad \text{for } i = 1,...,N_r$$
$$\text{where } \bar{y}_l^i = \frac{1}{n_r}\sum_{k=1}^{n_r} y_l^{i(k)} \tag{2}$$

The estimates of Eq. (2) can serve as noisy observations to train a secondary GP model (Kyprioti and Taflanidis, 2021) to support the heteroskedastic variance approximation. This approximation is then utilized within the primary GP calibration, which provides the final stochastic variance estimate, to establish the distribution approximation for Eq. (1). One limitation of the *RV* stochastic emulation strategy is that the observation of Eq. (2) for the heteroscedastic variance approximation rely only on the training points with replications. Another limitation is that replicated samples are always needed. Details for the GP-based stochastic emulator for this implementation are provided in (Kyprioti and Taflanidis, 2021).

In the *SD* formulation, the *squared sample deviation* is introduced to replace the *sample variance* of Eq. (2), so that information from both replicated and non-replicated samples can be utilized. The sample deviation is defined as the distance of the response observation from some primitive estimate of the response mean, denoted $\hat{m}_l(\mathbf{x})$, and its square is expressed as

$$(s_l^2)^{i(k)} = (y_l^{i(k)} - \hat{m}_l(\mathbf{x}^i))^2, \qquad i = 1,....,N_t \quad \text{and} \quad k = 1,....,n^i \tag{3}$$

This requires to first establish the prediction of $\hat{m}_l(\mathbf{x})$ and different smoothing techniques (Cleveland and Loader, 1996, Li et al., 2022, Hastie et al., 2009) can be used for this purpose. The one adopted in Yi and Taflanidis (2004) is to introduce a tertiary GP, denoted GP_m, with homoskedesticity assumption (Marrel et al., 2012, Zhang and Ni, 2020). This tertiary GP provides an approximation $\hat{m}_l(\mathbf{x})$ which is then utilized to establish noisy observations of the variance according to Eq. (3) to train a modified secondary GP model, to offer an alternative heteroskedastic variance approximation. The primary GP is then established identically as in the *RV* formulation, providing estimates for the stochastic variance estimate. Compared to *RV*, *SD* can be used without any replicated samples, which is something shown to offer higher accuracy and convenience in previous studies (Yi and Taflanidis, 2024). These two implementation choices to approximate marginal variances are respectively denoted herein RV_M and SD_M, with the subscript *M* to distinguish their extension to the covariance estimation introduced in the next section. Details for the GP-based stochastic emulator for this implementation are provided in (Yi and Taflanidis, 2024).

4 APPROXIMATION OF CORRELATION BETWEEN OUTPUTS AND OF THE JOINT EDP DISTRIBUTION

4.1 Approximation of the joint distribution

An approximation of the joint distribution $\tilde{p}(\mathbf{z}|\mathbf{x})$ can be established by combining the stochastic emulation approximation for the marginal distributions $\{\tilde{p}(z_l|\mathbf{x}); l = 1,,.n_z\}$ and an approximation for the correlation matrix, composed of the correlation coefficients between pairs of output components. The marginal distribution predictions can be obtained through the GP-based stochastic emulation discussed in Section 3 or through other alternative emulation approaches that do not entail a Gaussian

process approximation (Zhu and Sudret, 2021), and The approximation of the correlation matrix will be examined in Section 4.2.

4.2 Details for the GP-based approximation for the correlation matrix

For approximating the correlation matrix, a surrogate model will be utilized based on the available observations. To formalize implementation, let $\mathbf{V}(\mathbf{x}) \in \mathbb{R}^{n_z \times n_z}$ represent the symmetric covariance matrix of **y** conditional on input **x**:

$$\mathbf{V}(\mathbf{x}) = E[(\mathbf{y} - E[\mathbf{y} \mid \mathbf{x}])(\mathbf{y} - E[\mathbf{y} \mid \mathbf{x}])^T \mid \mathbf{x}] \tag{4}$$

where $E[.|\mathbf{x}]$ denotes expectation with respect to the stochastic randomness impacting the response output for given input parameters **x**. Also let $\mathbf{P}(\mathbf{x}) \in \mathbb{R}^{n_z \times n_z}$ represent the corresponding symmetric correlation matrix given by:

$$\mathbf{P}(\mathbf{x}) = \text{diag}(\mathbf{V}(\mathbf{x}))^{-1/2}\mathbf{V}(\mathbf{x})\text{diag}(\mathbf{V}(\mathbf{x}))^{-1/2} \tag{5}$$

where for a matrix **B**, diag(**B**) corresponds to a diagonal matrix maintaining only the elements of **B** along its diagonal. Note that the diagonal elements of $\mathbf{P}(\mathbf{x})$ are all equal to 1. The objective is to approximate the upper triangular elements of $\mathbf{V}(\mathbf{x})$ (including diagonal) or $\mathbf{P}(\mathbf{x})$ (excluding diagonal) to arrive at the approximation of full correlation matrix $\tilde{\mathbf{P}}(\mathbf{x})$.

Following the problem setup presented in Section 2, two different formulations can be considered for obtaining the observations to support the surrogate model approximation for $\mathbf{V}(\mathbf{x})$ or $\mathbf{P}(\mathbf{x})$: the first relying on statistics from the training points with replications and the second relying on samples for the cross-deviation from the mean. These are identical to the formulations *RV* and *SD*, respectively, considered in Section 3, and will be referenced with the same acronyms.

In the *RV* formulation, the training inputs with replications ($\mathbf{X}_p$) can be used to obtain unbiased estimates for the sample covariance between the *l*th and *j*th response outputs as:

$$(\bar{V}_{lj})^i = \frac{1}{n_r - 1}\sum_{k=1}^{n_r}(y_l^{i(k)} - \bar{y}_l^i)(y_j^{i(k)} - \bar{y}_j^i), \qquad \text{for } i = 1,...,N_r, l = 1,...,n_z, j = l,...,n_z \tag{6}$$

where sample mean vector $\bar{y}_l^i$ is defined as in Eq. (2). Equivalently, the sample correlation $\{(\bar{P}_{lj})^i; l = 1,...,n_z, j = l+1,...,n_z\}$ for the same response outputs is obtained by substituting Eq. (6) to the relationship shown in Eq. (5). A GP model can be then calibrated utilizing these noisy observations of covariance or correlation components to establish approximations covariance or correlation matrix, respectively. The noise in these observations originates from the variability in the sample-based estimator error of the covariance of Eq. (6), and can be addressed using a homoscedastic nugget in the GP formulation (Kyprioti and Taflanidis, 2021). Note that the selection of n_r controls the noise-level (larger n_r improves statistical accuracy for Eq. (6) and so reduces noise), but also the number of unique training points that may be considered for the same computational budget N_{sim} (smaller n_r accommodates a better exploration of the input domain). This selection needs to be made carefully balancing the competing objectives of noise-level in the observations and ability to explore the input domain.

The resultant covariance or correlation matrices will be symmetric by construction, but are not guaranteed to be positive definite, which is another foundational property for covariance or correlation matrices. Note that the observation data correspond to positive definite matrices, but the GP-based approximations are not guaranteed to maintain this property, as also explained in the next paragraph. A correction step is introduced to obtain the final predictions of the matrices that are positive definite. Various approaches exist for accommodating such a correction (Liu and Kiureghian, 1991), and here

the simplest one is adopted, modifying all negative eigenvalues of the resultant $\tilde{\mathbf{V}}(\mathbf{x})$ matrix (or $\tilde{\mathbf{P}}(\mathbf{x})$ matrix) to be slightly larger than 0 (eigenvectors are not modified).

The remaining important question is how to handle the multi-dimension output in the GP model calibration. One approach would be to calibrate separate metamodels for each of the of the upper triangular components of $\mathbf{V}(\mathbf{x})$ or $\mathbf{P}(\mathbf{x})$. The independent calibration of metamodels, in this case, results in approximations that will not maintain the dependence structure of the original observation data (Jia et al., 2016), and therefore will very frequently yield approximations for the covariance or correlation matrices that are not positive definite. Preliminary results obtained in the context of this study show that the correction that needs to be employed in this instance can substantially reduce the accuracy of the approximation. This challenge is alleviated by adopting a parallel GP (Gu and Berger, 2016), using a single set of hyper-parameters for the entire multi-output. This parallel GP formulation maintains the dependence structure of the observation data, yielding approximation for the covariance or correlation matrices that are almost always positive definite, requiring very infrequent corrections. Based on this setup, these two RV formulations to approximate the covariance and correlation components are respectively denoted as RV_v and RV_ρ.

Moving now to the *SD* formulation, the *squared sample cross-deviation* is introduced to replace the *sample covariance* of Eq. (6), so that information from both replicated and non-replicated samples can be utilized. The sample cross-deviation is defined as the distance of the response observation from the estimate of the response mean $\hat{m}_l(\mathbf{x})$

$$(s_{lj})^{i(k)} = (y_l^{j(k)} - \hat{m}_l(\mathbf{x}^i))(y_j^{j(k)} - \hat{m}_j(\mathbf{x}^i)), \quad i = 1,....,N_t \quad \text{and} \quad k = 1,....,n^i \tag{7}$$

where $\hat{m}_l(\mathbf{x})$ can be obtained through any appropriate approach, for example using the GP_m discussed in Section 3 or the mean of $\tilde{p}(y_l \mid \mathbf{x})$ if already available. Combining elements $\{(s_{lj})^{i(k)}; l = 1,...,n_z, j = l,...,n_z\}$ provides observation for the covariance matrix $\mathbf{V}(\mathbf{x})$ for the entire training set, including the training points with replications and the training points without replications. Similar to the *RV* formulation, a parallel GP is advocated to establish approximation of the covariance matrix. This implementation variant is denoted as SD_{vs}. Note that *SD* formulation can only be established for covariance components and not correlation components, as the sample correlation can be defined only with more than two samples.

4.3 Computational integration of GP-based approximation of marginal distributions and correlation matrix

Utilizing the approximations of marginal distributions $\{\tilde{p}(z_l \mid \mathbf{x}); l = 1,...,n_z\}$ and the correlation matrix $\tilde{\mathbf{P}}(\mathbf{x})$, the joint distribution can be approximated using the Nataf transformation (Der Kiureghian, 2022) which is a widely popular approach for modeling the joint distribution of correlated variables in risk and reliability analysis (Liu and Kiureghian, 1991, Straub and Papaioannou, 2015, Melchers and Beck, 2018). The details for employing this transformation depend on the exact type of marginal distribution. If a GP-based approximation is established for both the marginal distributions and the correlation matrix, then the joint distribution can be seamlessly approximated as a multi-variate Gaussian. Additionally, an integration of the computational implementation to obtain joint Gaussian distribution of EDPs can be promoted by combining the GP-based stochastic emulation discussed in Section 3 with the GP-based correlation matrix approximation reviewed in Section 4.2. As a result, the first two variants, denoted $RV_{J\rho}$ or RV_{Jv}, are established for *RV* formulation depending on whether variant RV_ρ or RV_v is adopted for the correlation approximation. The third variant, denoted SD_J, is established for *SD* formulation and utilizes SD_v for the correlation approximation. For RV_{Jv} and SD_J, which first approximate covariance matrix, the training of secondary GP model in the RV_M or SD_M formulations can be omitted, as the variance estimates are already included in the covariance estimates. This contributes to a reduction of n_z GP calibrations that need to be performed within the stochastic emulation workflow. In contrast, for

$RV_{J\rho}$, which directly approximates the correlation matrix, no modification to RV_M formulation is needed, and therefore no computaitonal benefits are provided.

5 ILLUSTRATIVE EXAMPLE

5.1 Structural and excitation models

The illustrative example revisits the example discussed in Kyprioti and Taflanidis (2021) but extends it to consider the approximation of the entire EDP vector. The example considers the approximation of the distribution for peak drift and absolute floor acceleration EDPs for a three-story concrete moment resisting frame (MRF), with seismic excitation described through a stochastic ground motion model. The model for the three-story concrete MRF building is described in detail in Patsialis and Taflanidis (2020). Following Kyprioti and Taflanidis (2021), the uncertain structural model parameters are provided in Table 1 along with their input domain, leading to the structural parameter vector of $\mathbf{x}_s = [f_{c1}, f_{c2}, f_{c3}, \varepsilon_{c1}, \varepsilon_{c2}, \varepsilon_{c3}, E_s, f_y, a, \zeta_s]$. The seismic excitation is described using a point-source stochastic ground motion model (Boore, 2003). The moment magnitude, M, and rupture distance, r_{rup}, are considered as explanatory input parameters for describing the seismic hazard, leading to excitation input parameter vector defined as $\mathbf{x}_g = [M\ r_{rup}]$. The input domain for M is chosen as [5 8] and for r_{rup} as [3 60] (km). The input vector for the problem description $\mathbf{x}$ is composed of $\mathbf{x}_s$ and $\mathbf{x}_g$ and consists of n_x=12 parameters.

Table 1: Structural parameter input domain for the surrogate model development and the associated probability distributions used in the risk assessment.

Structural parameter	Notation	Input domain for surrogate model formulation
Maximum compressive stress at each story for concrete	f_{c1}, f_{c2}, f_{c3}	[17,000 46,100] (kPa)
Strain at maximum stress for concrete	$\varepsilon_{c1}, \varepsilon_{c2}, \varepsilon_{c3}$	[0.0012 0.0033] (-)
The modulus of elasticity for steel	E_s	$[1.8\ \ 2.3]\cdot 10^8$ (kPa)
Yielding stress for steel	f_y	[430,000 700,000] (kPa)
Strain hardening ratio for steel	a	[0.006 0.017] (-)
Damping ratio	ζ_s	[3 8.2] (%)

5.2 Implementation details

The EDPs considered correspond to all peak inter-story drifts and all peak absolute floor accelerations (n_z=6). All three formulation variants, $RV_{J\rho}$, RV_{Jv} and SD_J, presented in Section 4.3 are implemented for approximation of the joint EDP distribution. The output considered in each case corresponds to the log-EDP. The appropriateness of using a Gaussian approximation for the marginal distributions for this specific problem, with aleatoric randomness originating strictly from a white noise sequence has been already investigated in past studies (Gidaris et al., 2015, Tsioulou et al., 2018).

We further investigate the benefit offered from replications by exploiting different mixtures of replicated and non-replicated training samples. In particular, three different values of replication size (n_r = 10 and 20) are investigated, as well as the varying numbers of the total simulations (N_{sim}=1000 and 500). Similarly, chosen cases of N_n are N_n=200, 400, 600, 800, and 1000. Among the listed N_n and N_{sim} values, the pairs that satisfy $N_n<N_{sim}$ are investigated for both the *RV* and *SD* formulations while the $N_n=N_{sim}$ cases (i.e. no replications) are only examined for the *SD* formulation. Note that, for example, when (N_{sim}=1000, N_n=200, n_r=10) is chosen, the number of replicated points is $N_r=(N_{sim}-N_n)/n_r$=80. Similarly, when (N_{sim}=1000, N_n=1000) is chosen, all the points in the training sets are non-replication points, and N_r is zero (n_r need not be defined). The training points are selected using space filling Latin Hypercube sampling in the input domains X defined in Table 1, while the numerical experiments are repeated 15 times in each case for different realizations of the training points. Linear basis functions are utilized for the influential input parameters, corresponding to the moment magnitude, while a generalized exponential correlation function was used for the correlation kernel.

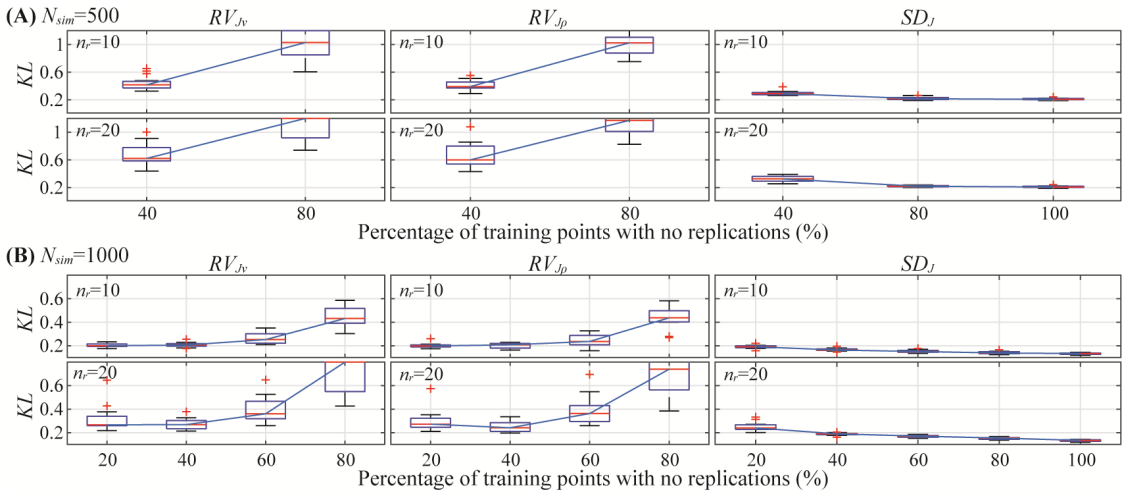

Figure 1: Averaged KL divergence for the joint EDP distribution for the RV_{Jv}, RV_{Jp}, and SD_J variants.

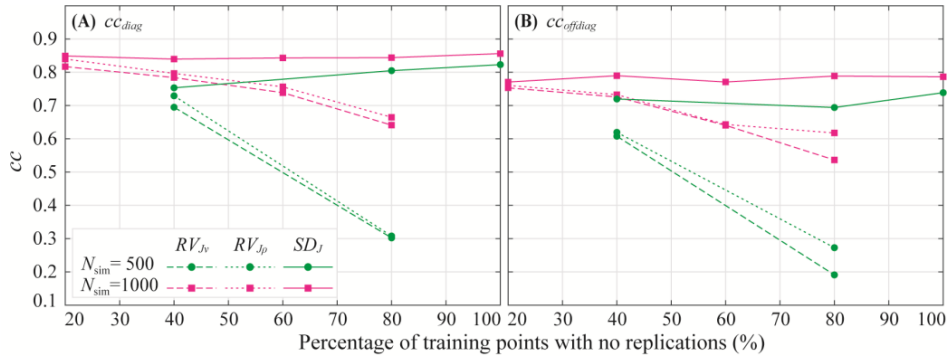

Figure 2: Average correlation coefficient metric for covariance predictions over diagonal and offdiagonal elements for n_r=10

5.3 Validation results and discussion

The validation results are presented in Figures 1-2, respectively showing KL divergence and correlation coefficients (*cc*) between the surrogate model predictions and reference EDP responses. Note the KL divergence value is normalized by dividing the value by the dimension of joint distribution, i.e. n_z=6. Both validation metrics are computed using the uniformly generated 1000 test samples across the training range. In Figure 1, the variability across the 15 different implementation trials, corresponding to different random selection of training points, is depicted in these figures in the form of boxplots. The validation results are shown for different percentages of training points without replications (N_n/N_{sim}×100), representing different computational budget allocation scenarios. Note that 100% (i.e. "no replication" implementation) is presented only for *SD* approach because the implementation without replication cannot be accommodated for the *RV* implementation. Figure 2 presents the average *cc* separately for diagonal and offdiagonal components of covariance matrix for n_r =10. For Figures 2, only the mean performance across 15 repetitions is shown.

It is evident that good overall accuracy is achieved, with KL divergence as small as 0.1 with narrow box bounds. As expected, this accuracy increases as the computational budget (N_{sim}) increases. The *SD* implementation outperforms the *RV* variants, especially for the higher percentage range of training points with no replications. This trend holds for all N_{sim} and n_r values examined and stresses the benefit of utilizing non-replicated samples in deriving the second-order statistics. As the number of training points without replications increases, the better exploration of the input domain accommodated by this

implementation (larger number of distinct training points for **x** allowed), ultimately supports greater accuracy for the SD_J variant. This agrees with the trend reported in (Yi and Taflanidis, 2024) when examining the marginal distribution approximation accuracy. The best overall performance is achieved for SD_J without any replications (i.e. n^i=1 for all training points), demonstrating the importance of the *SD* computational workflow that can accommodate this implementation. It is important to note that RV_{Jv} and $RV_{J\rho}$ show similar performance level across all examined cases. Despite the different computational approaches in deriving the correlation approximation in these variants, the achieved accuracy seems to be of a similar level. Comparing the different replication sizes, the smaller replication size of n_r=10 appears to perform slightly better overall, promoting an increased exploration of the domain by allowing a larger number of unique training points for the same computational budget (Kyprioti and Taflanidis, 2021, Yi and Taflanidis, 2024). Only when the number of training points with replications is relatively small, one can expect some small benefits from increasing the n_r for the *RV* formulations. This trend should be attributed to an improved statistical accuracy of the observations utilized for the second-order statistics approximation; when this number is small (small number of training points with replications) lower noise in these observations (larger n_r value) becomes beneficial (Kyprioti and Taflanidis, 2021) .

Figure 2 shows that across all variants, the trends for diagonal components (variance statistics) are similar to the offdiagonal components (covariance statistics) with only a small reduction of performance for the latter. This shows that the parallel GP-based approximation of the covariance (for SD_v or RV_{Jv}) or correlation (for $RV_{J\rho}$) matrices yield consistent prediction accuracy across both diagonal and offdiagonal statistics. *SD* implementation shows good accuracy with average of *cc* for diagonal and offdiagonal components reaching respectively 0.8 and 0.75 even for a small computational budget (N_{sim} =500). The performance of the *SD* implementation stays consistent, or slightly increases, as the training points without replication increases. The *RV* variants show similar accuracy to *SD* when the number of training points without replications is small, but their performance drastically deteriorates when the training points without replications increases, which is consistent with the trend observed in Figure 1.

In conclusion, for approximating the output correlation statistics in stochastic emulation settings, *SD* implementation should be preferred with no replication samples to promote greater exploration of the input domain as long as the underlying surrogate model can recognize the higher noise level infused in this instance. If *RV* implementation is preferred, then either the correlation of covariance matrix components can be approximated, but a sufficient number of training points with replications and an appropriate replication size n_r should be utilized. An iterative selection of training points can be utilized for making these choices (Binois et al., 2019). Readers interested in the validation of this implementation within seismic vulnerability and risk estimation are referred to Yi and Taflanidis (2024) and Yi and Taflanidis (2025)

6 CONCLUSIONS

This paper proposed a workflow to address multiple outputs in stochastic emulation, focusing on capturing the joint second-order statistics between outputs arising from the stochastic randomness within the simulation. Though the developments are general, they were couched within a specific application of interest: the approximation of the engineering demand parameter (EDP) joint distribution for seismic risk assessment. In this case, the stochasticity pertains to the aleatoric uncertainty in the hazard description (ground motion variability). The key challenge, newly addressed in this paper, pertains to capturing the heteroskedasticity in the correlation of the joint output variables. For approximating the output correlation matrix for given simulation inputs, a GP regression model was introduced. Two different implementations were examined, either directly approximating the correlation matrix or approximating first the covariance matrix and, through that, obtaining approximations for the correlation matrix. To ensure the positive definiteness of the correlation matrix predictions, a single calibration was promoted for the GP, sharing hyper-parameters across all correlation (or covariance) matrix components and a final correction step was introduced, adjusting any negative eigenvalues of the resultant correlation matrix. The established correlation predictions can be ultimately combined with existing stochastic

emulation approaches for approximating the marginal distribution of each output component, to characterize the joint distribution of the output vector. An extensive numerical case study was performed to validate and compare the prediction performance of the three variants. The example problem aims to accelerate seismic risk analysis by jointly emulating the EDP responses for a three-story moment frame structure, with seismic hazard described through a stochastic ground motion model. The impacts of the percentage of training points with replications, of the number of replications used and of the total computational budget afforded for the emulator calibration were examined. It was shown that the proposed GP-based framework for approximating the covariance of correlation components of the output vector can provide results with good accuracy.

Interesting future research topics include the incorporation of projection mappings from the response output vector to a latent output vector to achieve reduced between-output correlations or recused degree of heteroskedastic behavior to promote higher accuracy in the surrogate model approximation, or the promotion of an adaptive selection of simulation experiments (including selection of replications needed) to improve the accuracy of the joint distribution approximation.

ACKNOWLEDGMENTS

This research was financially supported by the National Science Foundation under Grant CMMI-2131111. This support is gratefully acknowledged. Any opinions, findings, and conclusions or recommendations expressed in this material are those of the authors and do not necessarily reflect the views of the National Science Foundation.

REFERENCES

Ankenman, B., Nelson, B. L. & Staum, J. Stochastic kriging for simulation metamodeling. 2008 Winter simulation conference, 2008. IEEE, 362-370.

Baker, E., Barbillon, P., Fadikar, A., Gramacy, R. B., Herbei, R., Higdon, D., Huang, J., Johnson, L. R., Ma, P. & Mondal, A. 2022. Analyzing stochastic computer models: A review with opportunities. *Statistical Science,* 37, 64-89.

Baker, J. W. & Cornell, C. A. 2008. Uncertainty propagation in probabilistic seismic loss estimation. *Structural Safety,* 30, 236-252.

Binois, M., Gramacy, R. B. & Ludkovski, M. 2018. Practical heteroscedastic gaussian process modeling for large simulation experiments. *Journal of Computational and Graphical Statistics,* 27, 808-821.

Binois, M., Huang, J., Gramacy, R. B. & Ludkovski, M. 2019. Replication or exploration? Sequential design for stochastic simulation experiments. *Technometrics,* 61, 7-23.

Boore, D. M. 2003. Simulation of ground motion using the stochastic method. *Pure and Applied Geophysics,* 160, 635-676.

Cabanzo, C. M., Tinoco, J., Sousa, H. S., Coelho, M. & Matos, J. C. 2023. Adaptation of traditional risk-based methodology for slopes to probabilistic-based approach integrating surrogate models. *Computers and Geotechnics,* 161, 105577.

Cleveland, W. S. & Loader, C. Smoothing by local regression: Principles and methods. Statistical Theory and Computational Aspects of Smoothing: Proceedings of the COMPSTAT'94 Satellite Meeting held in Semmering, Austria, 27–28 August 1994, 1996. Springer, 10-49.

Der Kiureghian, A. 2022. *Structural and system reliability*, Cambridge University Press.

Gentile, R. & Galasso, C. 2022. Surrogate probabilistic seismic demand modelling of inelastic single-degree-of-freedom systems for efficient earthquake risk applications. *Earthquake Engineering & Structural Dynamics,* 51, 492-511.

Gentile, R., Galasso, C. & Pampanin, S. 2021. Material property uncertainties versus joint structural detailing: relative effect on the seismic fragility of reinforced concrete frames. *Journal of Structural Engineering,* 147, 04021007.

Gidaris, I., Taflanidis, A. A. & Mavroeidis, G. P. 2015. Kriging metamodeling in seismic risk assessment based on stochastic ground motion models. *Earthquake Engineering & Structural Dynamics,* 44, 2377–2399.

Goulet, C. A., Haselton, C. B., Mitrani-Reiser, J., Beck, J. L., Deierlein, G., Porter, K. A. & Stewart, J. P. 2007. Evaluation of the seismic performance of code-conforming reinforced-concrete frame building-From seismic hazard to collapse safety and economic losses. *Earthquake Engineering and Structural Dynamics,* 36, 1973-1997.

Gramacy, R. B. 2020. *Surrogates: Gaussian process modeling, design, and optimization for the applied sciences,* Chapman and Hall/CRC.

Gramacy, R. B. & Lee, H. K. 2012. Cases for the nugget in modeling computer experiments. *Statistics and Computing,* 22, 713-722.

Gu, M. & Berger, J. O. 2016. Parallel partial Gaussian process emulation for computer models with massive output. *The Annals of Applied Statistics,* 10, 1317-1347.

Haselton, C. B., Goulet, C. A., Mitrani-Reiser , J., Beck, J. L., Deierlein, G. G., Porter, K. A., Stewart, J. P. & Taciroglu, E. 2008. An assessment to Benchmark the seismic performance of a code-conforming reinforced concrete moment-frame building. PEER 2007/12.

Hastie, T., Tibshirani, R., Friedman, J. H. & Friedman, J. H. 2009. *The elements of statistical learning: data mining, inference, and prediction,* Springer.

Jalayer, F., Beck, J. & Zareian, F. 2012. Analyzing the sufficiency of alternative scalar and vector intensity measures of ground shaking based on information theory. *Journal of Engineering Mechanics,* 138, 307-316.

Jalayer, F. & Beck, J. L. 2008. Effects of two alternative representations of ground-motion uncertainty in probabilistic seismic demand assessment of structures. *Earthquake Engineering and Structural Dynamics,* 37, 61-79.

Jia, G., Taflanidis, A. A., Nadal-Caraballo, N. C., Melby, J., Kennedy, A. & Smith, J. 2016. Surrogate modeling for peak and time dependent storm surge prediction over an extended coastal region using an existing database of synthetic storms. *Natural Hazards,* 81, 909-938.

Jung, W., Taflanidis, A. A., Nadal-Caraballo, N. C., Yawn, M. C. & Aucoin, L. A. 2023. Regional storm surge hazard quantification using Gaussian process metamodeling techniques. *Natural Hazards,* 1-29.

Kazantzi, A., Vamvatsikos, D. & Lignos, D. 2014. Seismic performance of a steel moment-resisting frame subject to strength and ductility uncertainty. *Engineering Structures,* 78, 69-77.

Kim, T., Kwon, O. S. & Song, J. 2023. Deep learning based seismic response prediction of hysteretic systems having degradation and pinching. *Earthquake Engineering & Structural Dynamics,* 52, 2384-2406.

Kyprioti, A. P. & Taflanidis, A. A. 2021. Kriging metamodeling for seismic response distribution estimation. *Earthquake Engineering & Structural Dynamics,* 50, 3550-3576.

Kyprioti, A. P. & Taflanidis, A. A. 2022. Addressing the different sources of excitation variability in seismic response distribution estimation using kriging metamodeling. *Earthquake Engineering & Structural Dynamics,* 51, 2466-2495.

Li, B. & Spence, S. M. 2023. Real-time forecast of hurricane-induced damage risk to envelope systems of engineered buildings through metamodeling. *Journal of Wind Engineering and Industrial Aerodynamics,* 232, 105273.

Li, K., Wang, S., Liu, Y. & Song, X. 2022. An integrated surrogate modeling method for fusing noisy and noise-free data. *Journal of Mechanical Design,* 144, 061701.

Liu, P.-L. & Kiureghian, A. D. 1991. Finite element reliability of geometrically nonlinear uncertain structures. *Journal of engineering mechanics,* 117, 1806-1825.

Marrel, A., Iooss, B., Da Veiga, S. & Ribatet, M. 2012. Global sensitivity analysis of stochastic computer models with joint metamodels. *Statistics and Computing,* 22, 833-847.

Mcguire, R. K. 2004. *Seismic hazard and risk analysis,* Earthquake engineering research institute.

Melchers, R. E. & Beck, A. T. 2018. *Structural reliability analysis and prediction*, John wiley & sons.

Ning, C., Xie, Y., Burton, H. & Padgett, J. E. 2024. Enabling efficient regional seismic fragility assessment of multi-component bridge portfolios through Gaussian process regression and active learning. *Earthquake Engineering & Structural Dynamics, 53*(9), 2929-2949.

Patsialis, D., & Taflanidis, A. A. 2020. Reduced order modeling of hysteretic structural response and applications to seismic risk assessment. *Engineering Structures*, 209, 110135.

Rasmussen, C. E. & Williams, C. K. I. 2005. *Gaussian Processes for Machine Learning (Adaptive Computation and Machine Learning)*, Cambridge, The MIT Press.

Straub, D. & Papaioannou, I. 2015. Bayesian updating with structural reliability methods. *Journal of Engineering Mechanics*, 141, 04014134.

Tsioulou, A., Taflanidis, A. A. & Galasso, C. 2018. Hazard-compatible modification of stochastic ground motion models. *Earthquake Engineering & Structural Dynamics*, 47, 1774-1798.

Yi, S. & Taflanidis, A. A. 2024. Stochastic emulation with enhanced partial-and no-replication strategies for seismic response distribution estimation. *Earthquake Engineering & Structural Dynamics*, 53, 2354-2381.

Yi, S. & Taflanidis, A. A. 2025. Multi-output stochastic emulation with applications to seismic response correlation estimation. *Structural Safety*, In Press.

Yin, J., Ng, S. H. & Ng, K. M. 2011. Kriging metamodel with modified nugget-effect: The heteroscedastic variance case. *Computers & Industrial Engineering*, 61, 760-777.

Zhang, Q.-H. & Ni, Y.-Q. 2020. Improved most likely heteroscedastic Gaussian process regression via Bayesian residual moment estimator. *IEEE Transactions on Signal Processing*, 68, 3450-3460.

Zhu, X., Broccardo, M. & Sudret, B. 2023. Seismic fragility analysis using stochastic polynomial chaos expansions. *Probabilistic Engineering Mechanics*, 72, 103413.

Zhu, X. & Sudret, B. 2021. Emulation of stochastic simulators using generalized lambda models. *SIAM/ASA Journal on Uncertainty Quantification*, 9, 1345-1380.

UQ state-dependent framework for seismic fragility assessment of industrial components

C. Nardin[1,2], S. Marelli[2], O. S. Bursi[1], B. Sudret[2], and M. Broccardo[*1]

[1] *Department of Civil, Environmental and Mechanical Engineering, University of Trento, Italy*
[2] *Chair of Risk, Safety and Uncertainty Quantification, ETH Zürich, Switzerland*

May 6, 2025

Abstract

This study introduces a state-dependent probabilistic framework for seismic fragility assessment of industrial components, addressing a key limitation of traditional approaches—namely, their tendency to overlook the role of initial damage conditions and complex structural-components interactions. The proposed method enhances classical fragility analysis by incorporating both the effect of seismic sequences on the multi-component structural response and its inherend uncertainties. The framework leverages advanced tools for uncertainty quantification and reliability analysis, including: (i) polynomial chaos expansions (PCE) to propagate input uncertainties and build efficient surrogate models; (ii) bootstrap resampling techniques to generate statistically robust confidence intervals for the fragility estimates; (iii) application to an real industrial process component, demonstrating the practical relevance and adaptability of the approach. By explicitly accounting for the evolving physical state of the system, this methodology provides a more detailed and accurate representation of seismic vulnerability, particularly suited for complex, safety-critical facilities.

1 Introduction

1.1 Background and motivation

Assessing the vulnerability of structural and non-structural components to earthquakes is a cornerstone of modern probabilistic seismic risk assessment. The PEER performance-based earthquake engineering (PBEE) framework has become a standard in this field, thanks to its effective application of the total probability theorem to link seismic hazard, fragility, damage, and loss analyses.

At the heart of this framework lies fragility analysis, which estimates the conditional probability of reaching or exceeding a specific damage state (DS) given an intensity measure (IM) of ground

[*]marco.broccardo@unitn.it

motion. Originally developed for nuclear safety, fragility curves are now widely used—from collapse risk assessment to community resilience studies Nguyen and Lallemant (2021); Burton et al. (2016); Du et al. (2021); Rincon and Padgett (2024).

Recent advancements include multivariate fragility functions Du and Padgett (2020), hybrid real/artificial ground motion use Gentile and Galasso (2020a), surrogate modelling Abbiati et al. (2021), and both state- and time-dependent fragility formulations Iervolino et al. (2015); Di Maio et al. (2020); Ghosh and Padgett (2010). However, most prior work focuses on damage transitions from pristine states under single events, with limited research into state-dependent fragility, which captures (i) damage accumulation over seismic sequences and (ii) varying initial damage states Jia and Gardoni (2018); Gentile and Galasso (2020b); Sarno and Wu (2021).

This gap is especially relevant in light of sequences like Wenchuan (2008), Tohoku (2011), and Central Italy (2016), which exposed the compounded risks of repeated earthquakes. As a result, there is increasing attention on modelling cumulative damage and the dynamic performance of both structures and NSCs Pang et al. (2023); Kassem et al. (2019). On the input side, careful ground motion selection—using real mainshock–aftershock pairs or synthetic data via ground motion models—is critical to preserving within-sequence correlations Zhang et al. (2018).

Simulating such complex scenarios is computationally intensive, particularly due to the nonlinear behaviour and interaction between structural systems and NSCs Quinci et al. (2023); Filiatrault et al. (2001); Nardin et al. (2022).

To address this, surrogate models are increasingly employed to replace expensive finite element simulations in uncertainty quantification (UQ) tasks. Techniques like polynomial chaos expansions (PCE), Kriging, and neural networks have gained traction, offering not just approximation but also insights like response moments and prediction confidence.

1.2 Scope and novel contributions

This paper builds on these developments, proposing a novel UQ-based framework to derive state-dependent fragility curves for industrial NSCs using limited sequential NLTHAs and advanced metamodelling. Key contributions include:

- a new methodology for state-dependent fragility under seismic sequences;
- integration of PCE and bootstrapping to enhance statistical robustness with sparse data;
- application to real industrial systems;
- computational efficiency that supports integration with experimental data.

The methodology is detailed in Section 2, and applied to a vertical tank NSC on a braced frame from the EU project SPIF in Section 3. Findings and future directions are summarized in Section 4.

2 Methodology

Risk-informed seismic assessments often rely on simplified models for practical reasons. However, as stressed in the NIST GCR 17-917-44 report NIST (2017), such simplifications can lead to suboptimal or uneconomical designs, particularly in industrial contexts. In response, this section introduces a novel framework to derive state-dependent fragility curves that integrate experimental insights and surrogate modeling.

State-dependent fragility curves extend the classical definition by conditioning not only on seismic intensity measures **IM** (often a vector), but also on the system's pre-existing damage state $\mathrm{DS_i}$ Iervolino et al. (2015). The resulting formulation estimates the probability of transitioning to a more severe state $\mathrm{DS_j}$, given an initial $\mathrm{DS_i}$ and an intensity $\boldsymbol{im}$:

$$\mathbb{P}\left[\mathrm{DS_j}|\mathrm{DS_i},,\mathbf{IM}=\boldsymbol{im}\right]=\mathbb{P}\left[\mathrm{DS}\geq\mathrm{DS_j}|\mathrm{DS_i},,\mathbf{IM}=\boldsymbol{im}\right]-\mathbb{P}\left[\mathrm{DS}\geq\mathrm{DS_{j+1}}|\mathrm{DS_i},,\mathbf{IM}=\boldsymbol{im}\right], \quad (1)$$

for $j > i$, where i and j span discrete damage limit states. Figures 1(a–b) illustrate this transition framework, assuming no recovery and an absorbing failure state $\mathrm{DS_2}$ (e.g., collapse).

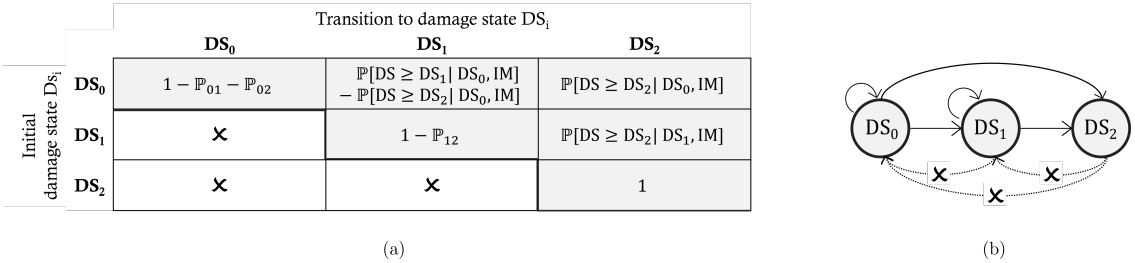

Figure 1: Transition state (a) matrix and (b) diagram.

Obtaining state-dependent fragilities requires populating the transition matrix with responses from many NLTHAs under sequential ground motions. These sequences are applied to simulate systems with varying initial damage states, enabling robust statistical sampling across transitions. Performances are then clustered by initial state and damage metric, and fragilities are derived either empirically or parametrically, conditioned on $\mathrm{DS_i}$ and **IM**.

Figure 2(a) outlines the workflow: starting from FE and seismic models (steps $\mathcal{A}$–$\mathcal{B}$), NLTHAs are executed to extract fragilities (step $\mathcal{C}$). However, this brute-force approach becomes computationally infeasible for realistic models and large ground motion sets.

To overcome this, we embed the uncertainty quantification (UQ) strategy developed in bib (2007); Sudret (2008). The process consists of: (i) defining the computational model $\mathcal{M}(\cdot)$, (ii) characterizing the uncertain inputs, and (iii) propagating uncertainty to estimate the quantities of interest (QoIs). Specifically, we model the system response to a stochastic ground motion sequence $A(t,\mathcal{X})$ as:

$$\mathcal{Y}=\mathcal{M}_{FE}\left(A(t,\mathcal{X})\right), \quad (2)$$

where $\mathcal{X}$ encodes both aleatory and epistemic uncertainties for the M-event sequence, and $\mathcal{Y}$ collects the resulting QoIs per event.

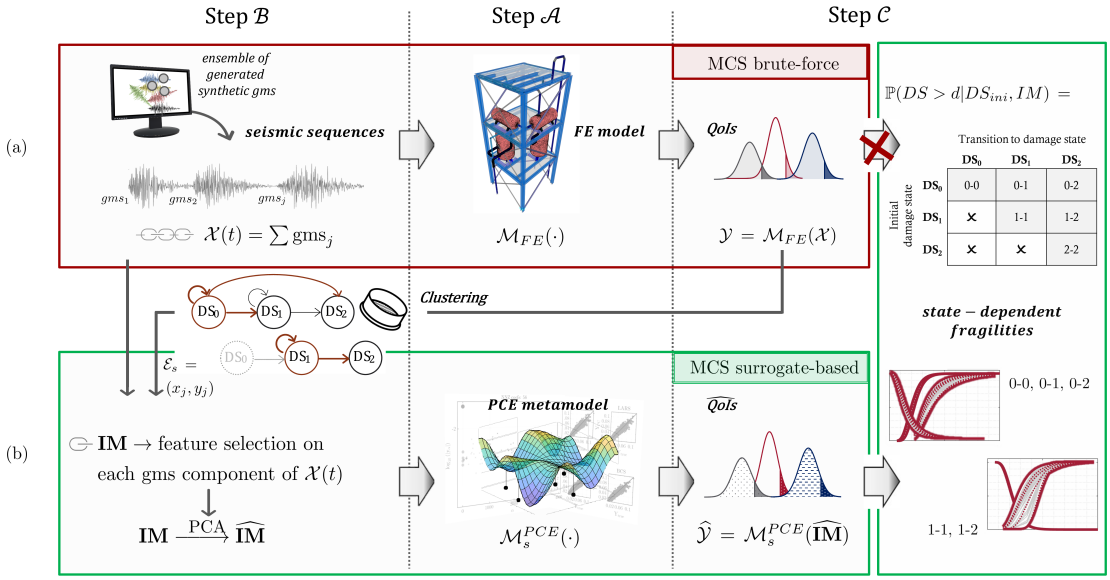

Figure 2: Steps $\mathcal{A}$–$\mathcal{C}$ for (a) brute-force and (b) surrogate-based approaches. Reproduced from Nardin et al. (2025).

To reduce computational demand, we replace $\mathcal{M}FE(\cdot)$ with surrogate models tailored to each initial damage state. Outputs are clustered by DS_i, producing datasets $\mathcal{D}s = (\mathbf{x}_j, y_j)$ for each state $s \in \text{DS}_0, \text{DS}_1$. Each $\mathbf{x}_j$ represents a ground motion from the sequence, reduced to a vector of IMs.

A significant number of IMs are initially considered. To reduce dimensionality, principal component analysis (PCA) is applied, yielding a set of uncorrelated pseudo-IMs, $\widehat{\mathbf{IM}}_j$.

Surrogate models based on polynomial chaos expansions (PCE) are then trained using $(\widehat{\mathbf{IM}}_j, y_j)$ pairs:

$$\widehat{\mathcal{Y}} = \mathcal{M}_s^{PCE}\left(\widehat{\mathbf{IM}}\right), \tag{3}$$

where s again identifies the initial damage state. These surrogates enable efficient Monte Carlo simulations for fragility estimation per Eq. 1, with minimal dependence on the original FE model.

Finally, this non-intrusive framework decouples FE modeling from UQ, allowing specialists in each area to collaborate independently. In the next Section, it is applied to a vertical tank structure from the SPIF project Nardin et al. (2022) to showcase its capabilities.

3 Industrial case study: vertical tank on 3D Braced-Frame structure

This section presents the application of the state-dependent fragility framework to a full-scale industrial case study involving the SPIF #2 experimental campaign Quinci et al. (2023); Nardin

(2022). The focus is on assessing the seismic fragility of a vertical tank mounted on a steel braced-frame (BF) substructure, a key non-structural component (NSC) with high vulnerability under seismic actions.

3.1 Step $\mathcal{A}$ — Computational Model Description

The finite element (FE) model was developed in SAP2000® SAP2000-v22 (2022), using linear elastic Euler–Bernoulli beam elements for the steel frame and flexible diaphragms for the floors. The NSCs, including vertical tanks and cabinets, were represented using dedicated stick models. Joint flexibility was modeled using calibrated rotational springs, while non-linear behavior was introduced for the bracing system via tension-only elements. The Young's modulus was set to 220GPa, based on prior calibration studies. A detailed view of the BF structure, the vertical tank, and both the global and local FE models is shown in Figure 3. The vertical tank, situated

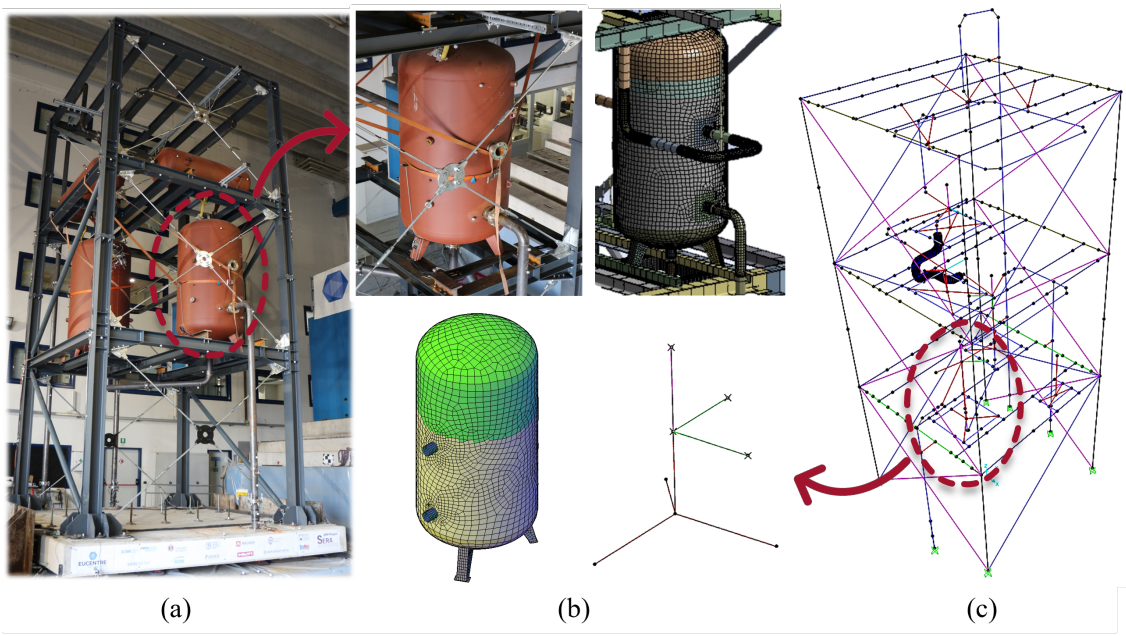

Figure 3: The SPIF #2 mock-up: (a) photo of the braced frame (BF) configuration on the shake table of EUCENTRE Facilities and details of the vertical tank installed at the first level; (b) SAP2000®high-fidelity local FE model and *ad-hoc* implemented stick-model for the vertical tank; (c) global SAP2000®FE model of SPIF #2. Reproduced from Nardin et al. (2025).

at the first floor level, demonstrated pronounced dynamic interaction with the host structure, with strong displacement responses noted during the shake table tests. Given the criticality of these components to operational safety, they were selected for fragility analysis using the bootstrap PCE methodology introduced earlier.

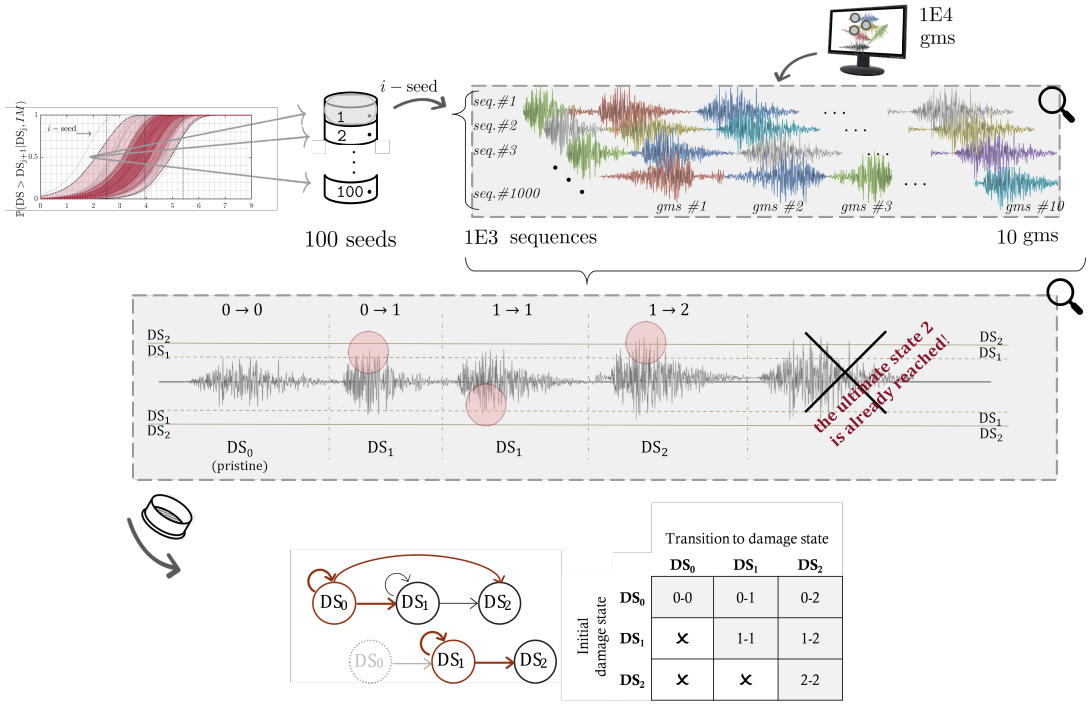

Figure 4: Individual realization of (seed) fragility curves.

3.2 Step $\mathcal{B}$ — Input Definition

To define the input space (Step $\mathcal{B}$), a sequence of 100 ground motion records, each comprising five seismic events, was applied to simulate various initial damage conditions and transition states. Performance thresholds were established for two damage states: DS_1 (DBE limit state) and DS_2 (SSE limit state), defined by base acceleration thresholds of $10 m/s^2$ and $16 m/s^2$, respectively Quinci et al. (2023).

The QoIs from NLTHAs were clustered into datasets $\mathcal{D}_0$ (undamaged), $\mathcal{D}_1$ (DBE-exceeded), and $\mathcal{D}_2$ (SSE-exceeded), as shown in Figure 4. A principal component analysis (PCA) was conducted on the complete list of intensity measures, reducing the dimensionality to 10 principal components that captured 99% of data variability.

3.3 Step $\mathcal{C}$ - QoI response

To efficiently predict the QoI—the peak acceleration at the base of the vertical tank—state-conditioned PCE surrogates were constructed for both $\mathcal{D}_0$ and $\mathcal{D}1$. These models employed the subspace pursuit (SP) solver and polynomial adaptivity, with convergence achieved at polynomial orders of 3 and 5, respectively. The surrogate performance is illustrated through histogram comparisons and control plots in Figures 5 and 6, with εLOO errors of 4.17×10^{-2} and 4.73×10^{-2}, respectively.

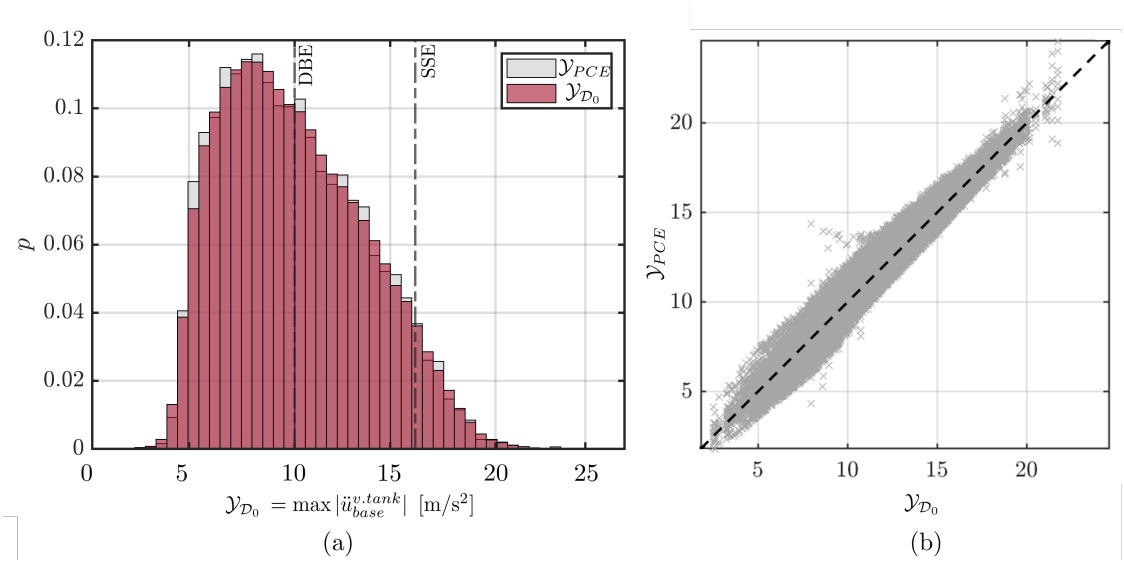

Figure 5: (a) Histogram distribution of the PCE surrogate $\mathcal{Y}_{PCE}$ (light grey) predictor *vs* the $\mathcal{Y}_{\mathcal{D}_0}$ original data of the initial undamaged condition dataset; (b) control plot of the performance of the $\mathcal{Y}_{PCE}$ surrogate model *vs* the $\mathcal{Y}_{\mathcal{D}_0}$ reference experimental design samples. Reproduced from Nardin et al. (2025).

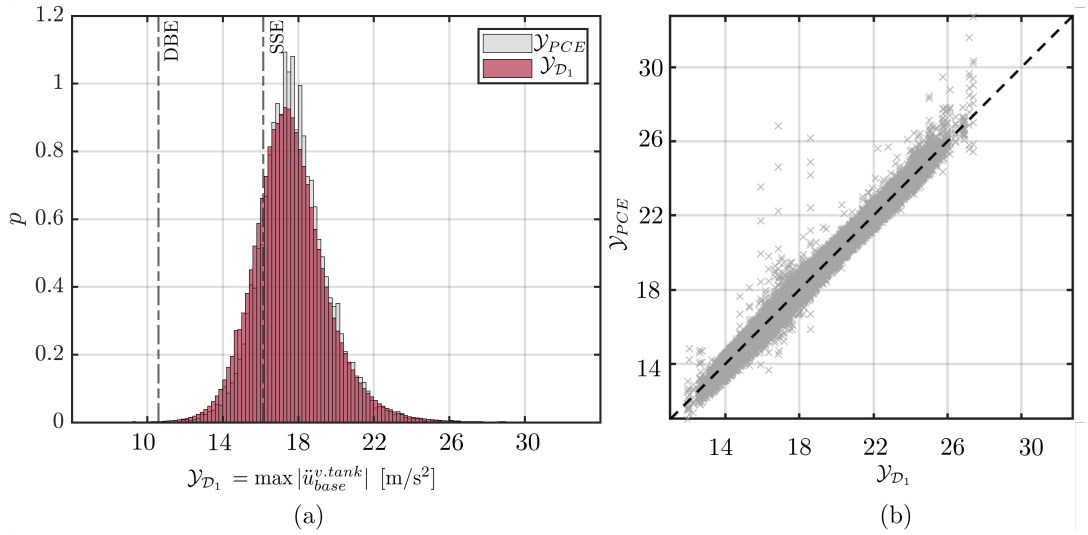

Figure 6: (a) Histogram distribution of the PCE surrogate $\mathcal{Y}_{PCE}$ (light grey) predictor *vs* the $\mathcal{Y}_{\mathcal{D}_1}$ original data of the initial undamaged condition dataset; (b) control plot of the performance of the $\mathcal{Y}_{PCE}$ surrogate model *vs* the $\mathcal{Y}_{\mathcal{D}_1}$ reference experimental design samples. Reproduced from Nardin et al. (2025).

Optimal IMs for fragility modeling were identified using the global $\beta_{\text{eff,glob}}$ metric, with peak ground acceleration (PGA) emerging as the most effective descriptor. State-dependent fragility functions, computed using the PCE surrogates and bootstrap resampling ($B = 500$), are presented

in Figure 7. These probabilistic curves capture epistemic uncertainties and provide critical insight into the transition probabilities across damage states under increasing seismic intensity.

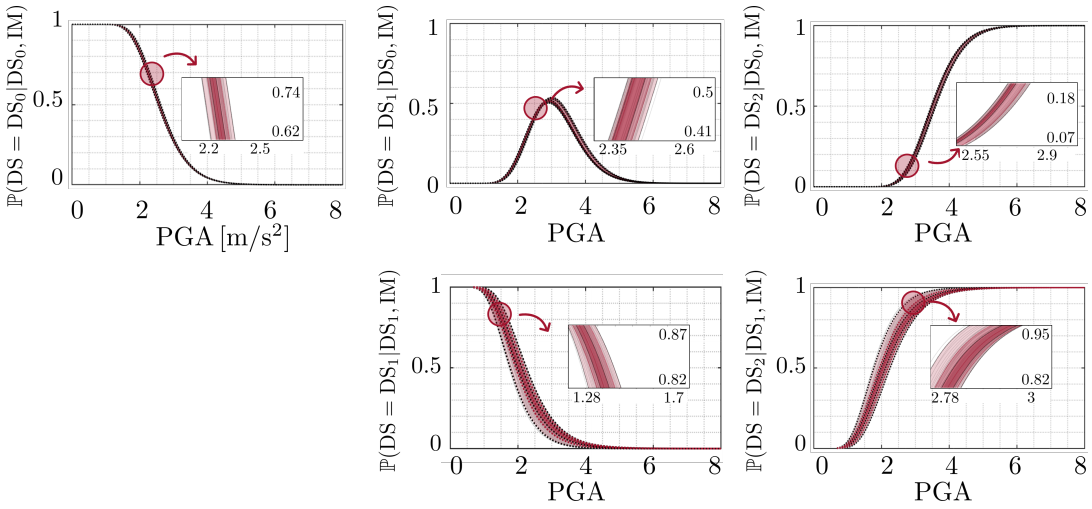

Figure 7: Bootstrap-PCE state-dependent fragility curves of the SPIF #2 vertical tank: black-dotted thick lines stand for the 1%, 50%, and 99% percentiles. Red-dotted lines for the 10% and 90% percentiles, along with their area with darker to lighter red-shaded colours. Adapted from Nardin et al. (2025).

4 Conclusions

This work presents a novel, non-intrusive UQ framework for computing state-dependent seismic fragility functions, addressing the computational challenges associated with traditional approaches. The method integrates (i) stochastic modeling of seismic sequences; (ii) finite element models; PCA for dimensionality reduction of input ground motions, and (iv) PCE for surrogate modeling of system responses.

By reducing the number of required NLTHAs and replacing them with surrogate-based Monte Carlo simulations, the framework enables efficient fragility assessment even for complex, computationally expensive models.

The methodology was applied to a critical vertical tank in a full-scale 3D industrial mock-up (SPIF #2). The results demonstrate the feasibility and robustness of the proposed fragility assessment framework when applied to real-world, full-scale industrial systems, offering a scalable and computationally efficient pathway for risk-informed decision-making in complex infrastructures.

References

(2007). *Uncertainty propagation and sensitivity analysis in mechanical models - Contributions to structural reliability and stochastic spectral methods*. Hab. a diriger des recherches, Universite Blaise Pascal, Clermont-Ferrand, France.

Abbiati, G., M. Broccardo, I. Abdallah, S. Marelli, and F. Paolacci (2021). Seismic fragility analysis based on artificial ground motions and surrogate modeling of validated structural simulators. *Earthquake Engineering & Structural Dynamics 50*(9), 2314–2333.

Burton, H. V., G. Deierlein, D. Lallemant, and T. Lin (2016). Framework for incorporating probabilistic building performance in the assessment of community seismic resilience. *Journal of Structural Engineering 142*(8), C4015007.

Di Maio, F., F. Matteo, G. Carlo, F. Perotti, and E. Zio (2020, 08). Time-dependent reliability analysis of the reactor building of a nuclear power plant for accounting of its aging and degradation. *Reliability Engineering & System Safety 205*, 107173.

Du, A., J. Cai, and S. Li (2021). Metamodel-based state-dependent fragility modeling for markovian sequential seismic damage assessment. *Engineering Structures 243*, 112644.

Du, A. and J. E. Padgett (2020). Investigation of multivariate seismic surrogate demand modeling for multi-response structural systems. *Engineering Structures 207*, 110210.

Filiatrault, A., C. Christopoulos, and C. Stearns (2001). Guidelines, specifications and seismic performance characterization of nonstructural building components and equipment. *PEER Report 2002/05, University of California, Berkeley, CA*.

Gentile, R. and C. Galasso (2020a, 07). Gaussian process regression for seismic fragility assessment of building portfolios. *Structural Safety 87*.

Gentile, R. and C. Galasso (2020b, 11). Hysteretic energy-based state-dependent fragility for ground-motion sequences. *Earthquake Engineering & Structural Dynamics 50*.

Ghosh, J. and J. E. Padgett (2010). Aging considerations in the development of time-dependent seismic fragility curves. *Journal of Structural Engineering 136*(12), 1497–1511.

Iervolino, I., M. Giorgio, and E. Chioccarelli (2015, 11). Markovian modeling of seismic damage accumulation. *Earthquake Engineering & Structural Dynamics 45*, 441–461.

Jia, G. and P. Gardoni (2018). State-dependent stochastic models: A general stochastic framework for modeling deteriorating engineering systems considering multiple deterioration processes and their interactions. *Structural Safety 72*, 99–110.

Kassem, M. M., F. M. Nazri, L. J. Wei, C. G. Tan, S. Shahidan, and S. S. M. Zuki (2019). Seismic fragility assessment for moment-resisting concrete frame with setback under repeated earthquakes. *Asian Journal of Civil Engineering 20*, 465–477.

Nardin, C. (2022). *Seismic experimental analyses and surrogate models of multi-component systems in special-risk industrial facilities*. Ph.d. thesis, Università degli Studi di Trento, Italy.

Nardin, C., O. S. Bursi, F. Paolacci, A. Pavese, and G. Quinci (2022). Experimental performance of a multi-storey braced frame structure with non-structural industrial components subjected to synthetic ground motions. *Earthquake Engineering & Structural Dynamics 51*(9), 2113–2136.

Nardin, C., S. Marelli, O. S. Bursi, B. Sudret, and M. Broccardo (2025). Uq state-dependent framework for seismic fragility assessment of industrial components. *Reliability Engineering & System Safety 261*, 111067.

Nguyen, M. and D. Lallemant (2021, 08). Order matters: The benefits of ordinal fragility curves for damage and loss estimation. *Risk Analysis 42*.

NIST (2017). Gcr 17-917-44. Technical report, Seismic Analysis, Design, and Installation of Nonstructural Components and Systems – Background and Recommendations for Future Work.

Pang, R., D. Zai, B. Xu, J. Liu, C. Zhao, Q. Fan, and Y. Chen (2023). Stochastic dynamic and reliability analysis of ap1000 nuclear power plants via dpim subjected to mainshock-aftershock sequences. *Reliability Engineering & System Safety 235*, 109217.

Quinci, G., C. Nardin, F. Paolacci, and O. Bursi (2023, 02). Modelling issues in seismic risk analysis of non-structural components located on industrial plant subsystems. *Bulletin Earthquake Engineering*.

Rincon, R. and J. E. Padgett (2024, 01). Fragility modeling practices and their implications on risk and resilience analysis: From the structure to the network scale. *Earthquake Spectra 40*.

SAP2000-v22 (2022). *Structural Analysis and Design. CSI Computer and Structures, Inc.*.

Sarno, L. D. and J.-R. Wu (2021). Fragility assessment of existing low-rise steel moment-resisting frames with masonry infills under mainshock-aftershock earthquake sequences. *Bulletin of Earthquake Engineering*.

Sudret, B. (2008). Global sensitivity analysis using polynomial chaos expansions. *Reliability Engineering & System Safety 93*(7), 964–979.

Zhang, Y., H. V. Burton, H. Sun, and M. Shokrabadi (2018). A machine learning framework for assessing post-earthquake structural safety. *Structural Safety 72*, 1–16.

Adaptive state space Kriging model for emulating complex dynamical systems under stochastic excitation

Kai Cheng[a*], Iason Papaioannou[a], MengZe Lyu[b] and Daniel Straub[a]

[a]*Engineering Risk Analysis Group, Technical University of Munich, Theresienstr. 90, Munich, 80333, Germany*
[b]*College of Civil Engineering, Tongji University, Siping Rd. 1239, Shanghai, 200092, China*

Abstract

Predicting the response of complex dynamical systems is a challenging task in engineering and applied sciences. In this contribution, we present a new surrogate modelling technique for emulating the behavior of stochastic dynamical systems with time-dependent exogenous excitation. Our method is established by learning the dynamics in state space form with sparse Kriging model. Sparsity is achieved by selecting a subset of the observed time history of the state vector and its derivative with respect to time with an active learning strategy for constructing a Kriging model. We also discuss a tailored algorithm for designing the training time history of state vector and its derivative, so as to ensure the robustness of Kriging for dynamical systems. We validate the performance of the proposed method with various benchmarks, which show that the proposed method is promising for accurately and efficiently emulating complex dynamical systems.

Keywords: Stochastic dynamical system; Surrogate model; Active learning; Gaussian process; Sparse learning.

1. Introduction

Dynamical systems are widely used in modern engineering and applied science for modeling complex underlying physical phenomena [1]. With the increase of computational power, numerical simulation offers a feasible way to study and predict the behavior of complex dynamical systems. However, the response of complex dynamical systems is governed by uncertainties, due to the stochastic external excitations, uncertain boundary conditions, and

natural variability of system properties [4]. To obtain effective prediction, these uncertainties must be accounted for. To this end, uncertainty quantification (UQ) of dynamical systems has gained particular interest in the last few decades [6, 5], but it usually requires many expensive model evaluations, which is infeasible in practice. To address this issue, surrogate models have been widely used to construct computationally efficient approximations of the expensive computational model. In this contribution, we propose a novel surrogate modelling technique for emulating complex nonlinear dynamical systems under stochastic excitation in their state space form with Kriging model, termed as the state space Kriging (S2K) model.

2. Methodology

Consider a general nonlinear dynamical system under stochastic excitation in its state space form [2] as

$$\boldsymbol{Y}(t) = \boldsymbol{f}(\boldsymbol{X}(t), \boldsymbol{U}(t)), \text{ with } \boldsymbol{X}(0) = \boldsymbol{x}_0, \tag{1}$$

where $\boldsymbol{X}(t) = [X_1(t), ..., X_n(t)]^{\mathrm{T}} \in \mathbb{R}^n$ is the state vector at time t; $\boldsymbol{x}_0$ is the initial condition; $\boldsymbol{Y}(t) = \dot{\boldsymbol{X}}(t)$ is the derivative of $\boldsymbol{X}(t)$ with respect to t; $\boldsymbol{U}(t) = [U_1(t), ..., U_m(t)]^{\mathrm{T}} \in \mathbb{R}^m$ is the external stochastic excitation vector acting on the structure; $\boldsymbol{f}(\cdot)$ is the n-dimensional nonlinear vector function .

Note that $\boldsymbol{f}(\cdot) : \mathbb{R}^{m+n} \to \mathbb{R}^n$ is a deterministic function, which maps the state vector $\boldsymbol{X}(t) \in \mathbb{R}^n$ and the external excitation $\boldsymbol{U}(t) \in \mathbb{R}^m$ to $\boldsymbol{Y}(t) \in \mathbb{R}^n$ at time instant t. The input dimension of $\boldsymbol{f}(\cdot)$ depends on the dimension of the state vector n of the associated dynamical system and the cardinality of the external excitation vector m. For every realization of the time history $\boldsymbol{u}(t)$ of the excitation $\boldsymbol{U}(t)$, the time history of the corresponding state vector $\boldsymbol{x}(t)$ and its derivative $\boldsymbol{y}(t)$ over the time period of interest $[0, T]$ can be estimated numerically.

We propose to to approximate the state space representation $\boldsymbol{f}(\cdot)$ with Kriging model [3, 7] component-wisely. To construct a Kriging model for the i-th component of $\boldsymbol{f}(\cdot)$, one can collect a few training time histories of input $\boldsymbol{\omega}(t) = [\boldsymbol{x}(t), \boldsymbol{u}(t)]^{\mathrm{T}} \in \mathbb{R}^{n+m}$ and the i-th output $y_i(t)$. To improve the robustness of S2K model, we suggest collecting the time histories of a pseudo state vector resulting from pseudo external excitation with magnified variability. In practice, one can magnify the standard deviation of the stochastic excitation at every time instant by a magnification factor $\sigma \in [1.5, 2]$. By

magnifying the variability of the excitation, the state vector will exhibit stronger variability, hence, it is expected that a few pseudo time histories of state vector will sufficiently populate its parameter space under the true excitation.

Once the S2K model is trained, it can be used to predict the time history of system response $\hat{\boldsymbol{x}}(t)$ for arbitrary realization of the time history $\boldsymbol{u}(t)$ of $\boldsymbol{U}(t)$ by solving the following approximate dynamical system in state space form

$$\hat{\boldsymbol{y}}(t) = \hat{\boldsymbol{f}}(\hat{\boldsymbol{x}}(t), \boldsymbol{u}(t)), \tag{2}$$

where $\hat{\boldsymbol{f}}(\cdot)$ is the Kriging approximation of $\boldsymbol{f}(\cdot)$. In general, the Runge-Kutta method can be used to estimate the time history of the state vector $\hat{\boldsymbol{x}}(t_i)(i = 1, ..., N_t)$ at N_t discretized time steps within the time period of interest $[0, T]$.

References

[1] Peter Benner, Serkan Gugercin, and Karen Willcox. A survey of projection-based model reduction methods for parametric dynamical systems. *SIAM review*, 57(4):483–531, 2015.

[2] Steven L Brunton, Joshua L Proctor, and J Nathan Kutz. Discovering governing equations from data by sparse identification of nonlinear dynamical systems. *Proceedings of the national academy of sciences*, 113(15):3932–3937, 2016.

[3] Jack PC Kleijnen. Kriging metamodeling in simulation: A review. *European journal of operational research*, 192(3):707–716, 2009.

[4] Jie Li and Jianbing Chen. *Stochastic dynamics of structures*. John Wiley & Sons, 2009.

[5] Meng-Ze Lyu, De-Cheng Feng, Jian-Bing Chen, and Jie Li. A decoupled approach for determination of the joint probability density function of a high-dimensional nonlinear stochastic dynamical system via the probability density evolution method. *Computer Methods in Applied Mechanics and Engineering*, 418:116443, 2024.

[6] Chu V Mai, Minas D Spiridonakos, Eleni N Chatzi, and Bruno Sudret. Surrogate modeling for stochastic dynamical systems by combining nonlinear autoregressive with exogenous input models and polynomial chaos expansions. *International Journal for Uncertainty Quantification*, 6(4), 2016.

[7] Christopher Williams and Carl Rasmussen. Gaussian processes for regression. *Advances in neural information processing systems*, 8, 1995.

Risk-Adaptive Approaches to Learning, Design, and Decision Making

Johannes O. Royset
Daniel J. Epstein Department of Industrial and Systems Engineering
University of Southern California

In most areas of engineering, one aims to determine a best decision, design, estimate, or model in the presence of uncertainty about the values of key parameters and data in a problem. The uncertainty stems from our incomplete knowledge about the state of a system, the inaccuracy of approximations that might have been adopted, and the human inaptitude to predict the future. One might hope that historical observations about varying quantities can inform us and ideally eliminate the uncertainty. Despite living in the era of big data, this aspiration rarely comes to fruition. Real-world data sets tend to be noisy, biased, corrupted, or simply insufficiently large. It is therefore prudent to optimize decisions, designs, and models while accounting *conservatively* for the uncertainty. Even when our grasp of the uncertainty in an application is fairly good, human nature and our desire to avoid exceptionally "bad" outcomes motivate conservativeness in decision making and modeling broadly. Thus, engineering designs, financial decisions, operational plans, military strategies, system controls, and statistical models are often selected conservatively.

While the various fields have approached decision making under uncertainty somewhat differently, overarching themes now emerge: the need to capture risk-averseness and ambiguity about uncertainty, promote computations and analysis, and enable explanations of algorithmic outcomes. The concept of *risk measures* provides a mathematical framework for unifying and understanding the various threads and how they connect. The framework encapsulates many common problems in robust control and optimization, distributionally robust optimization, adversarial machine learning, statistical estimation, financial risk management, utility maximization, attacker-defender games, and reliability-based design optimization. Supported by convex analysis, risk measures furnish a rich area for nonlinear analysis as well as opportunities for efficient computations. The vast literature on risk measures developed over the last 25 years is a testimony to the potency of the framework, both theoretically and practically.

The canonical problem in many engineering settings involves a *quantity of interest* given by a function $f(\xi, x)$, which depends on a *parameter* ξ and a *decision (control)* x. For example, $f(\xi, x)$ might quantify the performance of an engineering system designed according to our decision x, given an environmental condition represented by ξ. In supervised learning, $f(\xi, x)$ might specify the prediction error of a neural network designed according to x, given feature and label data ξ. Without fully knowing ξ, the problem is to determine a decision x such that $f(\xi, x)$ is minimized or, alternatively, $f(\xi, x)$ does not exceed a given threshold. The problem is ill-posed because ξ is unsettled. The uncertainty about ξ could stem from our incomplete knowledge of a "true" value, such as the demand for a product tomorrow, and/or from inherent variability in the value as exemplified by the many feature-label pairs a neural network needs to handle accurately.

There are several ways to proceed. One can estimate the value of ξ and adopt that value in the subsequent optimization and decision making. However, this fails to account for the uncertainty associated with ξ. The approach is especially problematic when ξ varies inherently and our decision x

needs to perform satisfactorily under different values of ξ. Alternatively, if there is a set Ξ of possible values of ξ, then one may consider the quantity of interest in the worst case across these values, i.e., $\sup_{\xi\in\Xi} f(\xi, x)$. The problem shifts to determining a decision x that minimizes this conservative quantity or makes it sufficiently low, which we refer to as *robust optimization*; see, e.g., [2, 3]. Yet another possibility is to model the uncertainty associated with ξ using a probability distribution. This brings in the vast and sophisticated tools of probability theory and statistics. In assessing a decision x, one can leverage the expected value of $f(\,\cdot\,, x)$ computed with respect to the adopted probability distribution. Thus, the problem becomes to find a decision that is satisfactory on average. This classical approach is the central tenet of *stochastic programming*; see, e.g., [4, 25, 22].

Risk measures capture all these possibilities and many more. Through choices of probability distributions, risk measures allow us to incorporate data and other information about the possible values of ξ and their likelihoods. They reflect a wide variety of concerns and preferences a decision maker may have toward various outcomes. When restricted suitably to the class of *regular measures of risk*, they exhibit theoretically and computationally advantageous properties. In particular, convexity, linearity, and smoothness of $f(\xi, x)$ in x commonly carry over to the resulting optimization problem. Many risk measures also address the fact that any adopted probability distribution is an imperfect model of the uncertainty associated with ξ. Thus, they account for ambiguity about the model of uncertainty, which leads to *distributionally robust optimization problems*, as exemplified by [27, 21, 14, 25], and connections with *stochastic dominance*; see, e.g., [5].

Risk measures originated in financial engineering as an approach to quantify the reserves banks, insurance companies, and other financial institutions need to cover potential future losses; see for example the influential paper [1], the textbooks [13, 7], and the review article [8]. However, risk measures have spread beyond financial engineering to operations management, reliability analysis, engineering design, defense planning, statistics, and machine learning.

Among the early reviews of risk measures, [16] stands out for a concise description of the important advances taking place around the turn of the century. The tutorials [24, 11] explain key concepts and introduce connections with statistics; see also the monograph [28]. With a focus on expected utility theory and dual utility theory, [23] reviews the deep mathematical relations between risk measures and these earlier theories as well as stochastic dominance; see also the recent paper [9]. While surveying risk measures and related concepts, [19] breaks new ground by connecting concepts of risk, regret, deviation, and error and thereby relating risk management to statistics. The paper [17] emphasizes the applicability of risk measures in reliability-based engineering design. For PDE-constrained optimization and uncertainty quantification, [10] discusses the needed technical assumptions in such infinite-dimensional settings as well as algorithms. The paper [26] surveys applications for autonomous systems. Reviews of superquantile risk measures appear in [6], with a focus on applications in supply chain management, scheduling, networks, energy, and medicine, and in [12], dealing with machine learning applications. Books covering risk measures broadly include [15, 7, 25, 22].

The above paragraphs are largely taken from the introduction of the recent survey article [20], which provides a succinct introduction to the area of risk measures and related concepts. It discusses the increasing interest in risk-averse approaches to statistical applications, with an updated review

of the risk quadrangle proposed in [19] and refined in [18]. The survey paper recounts the historical development of superquantiles (a.k.a. conditional value-at-risk, average value-at-risk, tail value-at-risk, and expected shortfall) and the central role they now play in many areas of operations research, engineering, and statistics. It introduces the terminology *measure of reliability* for failure probabilities, buffered failure probabilities, buffered probabilities of exceedance, and related concepts.

References

[1] P. Artzner, F. Delbaen, J.-M. Eber, and D. Heath. Coherent measures of risk. *Mathematical Finance*, 9(3):203–228, 1999.

[2] A. Ben-Tal, L. El Ghaoui, and A. Nemirovski. *Robust Optimization*. Princeton University Press, 2009.

[3] D. Bertsimas, D. B. Brown, and C. Caramanis. Theory and applications of robust optimization. *SIAM Review*, 53(3):464–501, 2011.

[4] J. R. Birge and F. Louveaux. *Introduction to Stochastic Programming*. Springer Series in Operations Research and Financial Engineering. Springer, 2. edition, 2011.

[5] D. Dentcheva and A. Ruszczyński. Optimization with stochastic dominance constraints. *SIAM J. Optimization*, 14(2):548–566, 2003.

[6] C. Filippi, G. Guastaroba, and M. G. Speranza. Conditional value-at-risk beyond finance: a survey. *International Transactions in Operational Research*, 27(3):1277–1319, 2020.

[7] H. Föllmer and A. Schied. *Stochastic Finance: An Introduction in Discrete Time*. de Gruyter, 4. edition, 2016.

[8] H. Föllmer and S. Weber. The axiomatic approach to risk measures for capital determination. *Annual Review of Financial Economics*, 7(1):301–337, 2015.

[9] C. Fröhlich and R. C. Williamson. Risk measures and upper probabilities: Coherence and stratification. *Preprint arXiv:2206.03183*, 2022.

[10] D. P. Kouri and A. Shapiro. Optimization of PDEs with uncertain inputs. In H. Antil, D. P. Kouri, M.-D. Lacasse, and D. Ridzal, editors, *Frontiers in PDE-Constrained Optimization*, The IMA Volumes in Mathematics and its Applications, pages 41–81. Springer, Cham, 2018.

[11] P. Krokhmal, M. Zabarankin, and S. Uryasev. Modeling and optimization of risk. *Surveys in Operations Research and Management Science*, 16(2):49–66, 2011.

[12] Y. Laguel, K. Pillutla, J. Malick, and Z. Harchaoui. Superquantiles at work: Machine learning applications and efficient subgradient computation. *Set-Valued and Variational Analysis*, 29:967–996, 2021.

[13] A. J. McNeil, R. Frey, and P. Embrechts. *Quantitative Risk Management: Concepts, Techniques and Tools*. Princeton University Press, 2015.

[14] P. Mohajerin Esfahani and D. Kuhn. Data-driven distributionally robust optimization using the wasserstein metric: Performance guarantees and tractable reformulations. *Mathematical Programming*, 171(1):115–166, 2018.

[15] G. Ch. Pflug and W. Römisch. *Modeling, measuring and managing risk*. World Scientific, 2007.

[16] R. T. Rockafellar. Coherent approaches to risk in optimization under uncertainty. In *Tutorials in Operations Research: OR Tools and Applications: Glimpses of Future Technologies*, Tutorials in Operations Research, pages 38–61. INFORMS, Cantonsville, MD, 2007.

[17] R. T. Rockafellar and J. O. Royset. Engineering decisions under risk-averseness. *ASCE-ASME J. Risk and Uncertainty in Engineering Systems, Part A: Civil Engineering*, 1(2):04015003, 2015.

[18] R. T. Rockafellar and J. O. Royset. Measures of residual risk with connections to regression, risk tracking, surrogate models, and ambiguity. *SIAM J. Optimization*, 25(2):1179–1208, 2015.

[19] R. T. Rockafellar and S. Uryasev. The fundamental risk quadrangle in risk management, optimization and statistical estimation. *Surveys in Operations Research and Management Science*, 18:33–53, 2013.

[20] J. O. Royset. Risk-adaptive approaches to stochastic optimization: A survey. *SIAM Review*, to appear, 2024.

[21] J. O. Royset and R. J-B Wets. Variational theory for optimization under stochastic ambiguity. *SIAM J. Optimization*, 27(2):1118–1149, 2017.

[22] J. O. Royset and R. J-B Wets. *An Optimization Primer*. Springer, 2021.

[23] A. Ruszczyński. Advances in risk-averse optimization. In H. Topaloglu, editor, *Tutorials in Operations Research: Theory Driven by Influential Applications*, Tutorials in Operations Research, pages 168–190. INFORMS, Cantonsville, MD, 2013.

[24] S. Sarykalin, G. Serraino, and S. Uryasev. Value-at-Risk vs. Conditional Value-at-Risk in risk management and optimization. In Z.-L. Chen and S. Raghavan, editors, *Tutorials in Operations Research: State-of-the-Art Decision-Making Tools in the Information-Intensive Age*, Tutorials in Operations Research, pages 270–294. INFORMS, Cantonsville, MD, 2008.

[25] A. Shapiro, D. Dentcheva, and A. Ruszczyński. *Lectures on Stochastic Programming: Modeling and Theory*. SIAM, 3. edition, 2021.

[26] Y. Wang and M. P. Chapman. Risk-averse autonomous systems: A brief history and recent developments from the perspective of optimal control. *Artificial Intelligence*, 311:103743, 2022.

[27] W. Wiesemann, D. Kuhn, and M. Sim. Distributionally robust convex optimization. *Operations Research*, 62(6):1358–1376, 2014.

[28] M. Zabarankin and S. Uryasev. *Statistical Decision Problems. Selected Concepts and Portfolio Safeguard Case Studies*. Springer, New York, NY, 2014.

Risk-informed Strategic Power Network Planning for Renewable Energy Transitions with DC-OPF

Uichan Seok[1], Ji-Eun Byun[2], Johannes O. Royset[3], and Junho Song[1]

[1] Department of Civil and Environmental Engineering, Seoul National University, Seoul, South Korea
[2] James Watt School of Engineering, University of Glasgow, Glasgow, United Kingdom
[3] Department of Industrial and Systems Engineering, University of Southern California, Los Angeles, USA

Abstract: Transitions to renewable energy requires strategic power network planning that accounts for weather uncertainty. This study presents a risk-informed decision-making framework for power network expansion by integrating probabilistic weather modeling with an extended Direct Current Optimal Power Flow (DC-OPF) formulation to enhance system reliability. Through the analysis of historical weather data, we identify key dependencies among weather variables and represent them using a Bayesian Network, enabling a structured understanding of their influence on renewable energy generation. Additionally, the buffered failure probability constraints are incorporated to mitigate power shortage risks. A five-node case study with 100 scenarios is conducted to evaluate the impact of incorporating generation and transmission expansion decisions into the proposed model, as well as its effects on system reliability and load shedding reduction. The results provide useful insights on the role of risk-aware constraints in shaping strategic power network planning for renewable energy transitions.

Keywords: Power grid expansion, renewable energy transitions; direct current optimal power flow; buffered failure probability; conditional value at risk; climate change

1 INTRODUCTION

The global energy landscape is undergoing a fundamental transformation as countries strive to transition from conventional fossil fuel-based power generation to renewable energy sources. This shift is driven by the urgent needs to mitigate climate change, enhance energy security, and ensure long-term sustainability. However, the integration of renewable energy into power grids, illustrated in Figure 1, pose significant challenges due to the inherent variability and uncertainty of weather-dependent generation sources such as solar and wind power. To facilitate effective long-term planning for renewable energy transitions, power network expansion must account for these uncertainties in a systematic and risk-informed manner. A key challenge lies in modeling the stochastic nature of weather conditions and their evolving trends over time. Therefore,

probabilistic system analysis is required to assess the impact of uncertain generation and demand on grid reliability and operational stability.

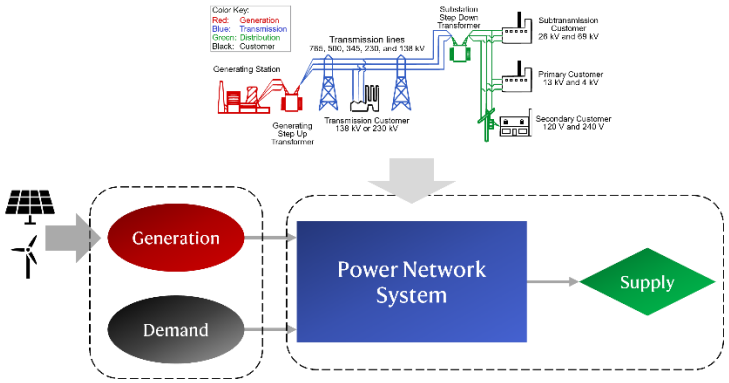

Figure 1 Power network system under renewable energy transition

To this end, we identify key dependencies among weather variables in this study to enable probabilistic modeling and formulate a strategic power network planning framework based on a direct current optimal power flow (DC-OPF) formulation. By capturing these relationships, we can generate probabilistic scenarios that reflect weather-driven uncertainties and incorporate them into the optimization process.

2 UNCERTAINTY QUANTIFICATION OF WEATHER CONDITIONS

Renewable energy generation, particularly from wind and solar power, is inherently dependent on weather conditions. On the other hand, electricity demand is significantly influenced by temperature variations, making weather modeling a crucial component of strategic power network planning. Therefore, this study considers temperature, wind speed, and solar radiation as the key weather variables and aims to construct a probabilistic framework to characterize their statistical dependencies and uncertainties.

For this purpose, we analyze historical weather data for Seoul from 1984 to 2023, using monthly resolution to capture seasonal variations. A key aspect of this analysis is to examine whether key weather variables—wind speed, solar radiation, and temperature—exhibit statistical independence in their joint probability density distributions. If the statistical independence does not hold, it indicates the presence of underlying dependencies that must be explicitly modeled, rather than assuming conditional independence on month.

The monthly scatter plots in Figure 2 show that solar radiation and temperature have strong statistical dependencies, particularly in certain months (e.g., April, July, and November) where their joint probability density distributions show clear bimodal structures. This indicates that the assumption of statistical independence between these two variables is invalid for certain seasonal conditions. To accurately capture this relationship, we introduce a latent weather node in a Bayesian Network (BN) method, which accounts for their probabilistic dependencies and enables

more realistic scenario generation for power network planning. The final structure of the BN, constructed for a power system under renewable energy transition, is presented in Figure 3.

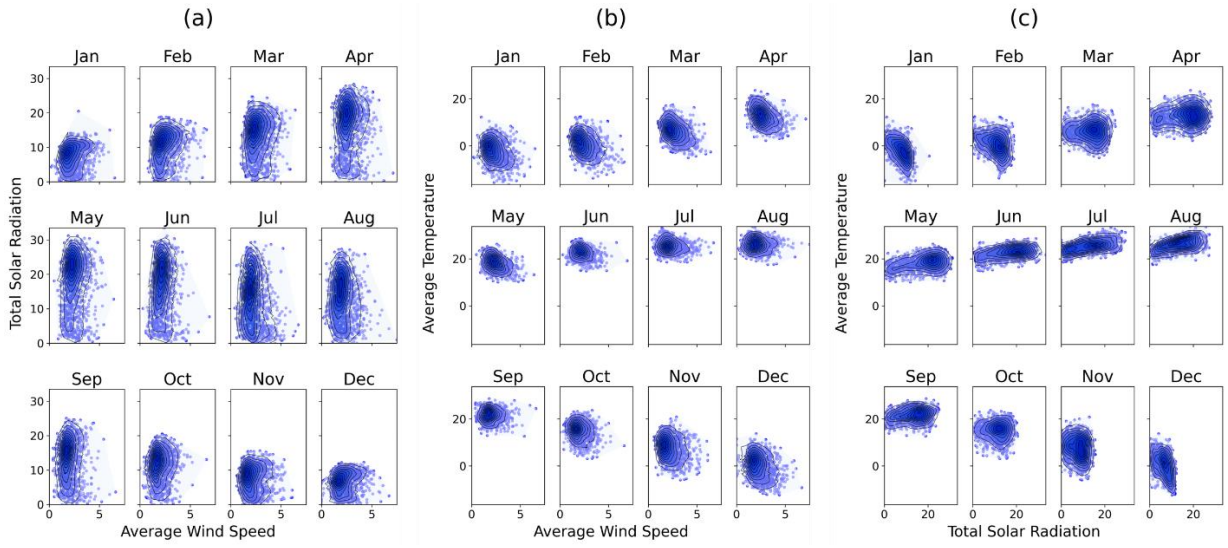

Figure 2 Monthly scatter plots between (a) average wind speed and total solar radiation, (b) average wind speed and average temperature, and (c) total solar radiation and average temperature

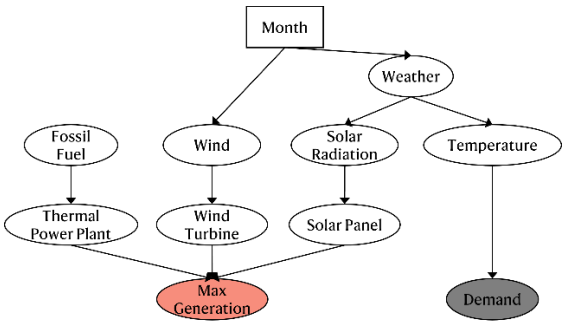

Figure 3 Final BN constructed for power system under renewable energy transition

3 LONG-TERM, UNCERTAINTY-INFORMED EXPANSION PLANNING

DC-OPF formulation is a fundamental tool for power system operation and planning. It is a mathematical optimization model that determines the most cost-effective dispatch of generation while satisfying physical and operational constraints. Unlike the full Alternating Current Optimal Power Flow (AC-OPF), which considers both active and reactive power flows, DC-OPF simplifies power flow equations by considering only active power and neglecting losses. This approximation significantly reduces computational complexity, making DC-OPF a widely adopted approach for large-scale power network studies.

In this study, the conventional DC-OPF formulation is extended to incorporate risk-informed power network expansion planning under renewable energy uncertainty. The basic model determines generation (P_g^{Gen}) and transmission (P_l) while ensuring that power flows comply with network topology and transmission limits, respecting Kirchhoff's laws and other physical constraints. Additionally, it enforces demand-supply balance across all scenarios while accounting for variability in renewable energy sources. To explicitly quantify power outage risks, a load shedding term (S) is introduced, capturing the extent of supply shortfalls in critical scenarios. Furthermore, the model includes both generator expansion (E_g) and transmission capacity expansion (E_l) as decision variables, enabling long-term strategic planning under uncertainty. To manage risk, the buffered failure probability ($\bar{p}_f$) is incorporated as a constraint, ensuring a probabilistically robust network design that mitigates the impact of uncertain generation and demand fluctuations. By integrating multiple scenarios within a unified optimization framework, this approach provides a holistic assessment of system reliability and investment strategies.

4 NUMERICAL INVESTIGATION

To assess the validation of the proposed risk-informed DC-OPF expansion model, a case study is conducted using a five-node transmission grid in Figure 4 under 100 stochastic demand scenarios. This numerical analysis evaluates how the integration of uncertainty quantification and risk constraints influences power generation, load shedding, and expansion strategies.

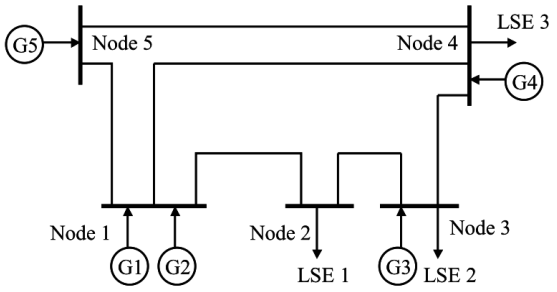

Figure 4 5-node transmission grid

The optimization results in Figure 5 highlight a significant shift in generation dispatch, with Generator 3 emerging as the primary power source. Unlike original optimization solutions in Figure 5(a), where power generation was more distributed across three generators, the proposed model identifies an optimal configuration that enhances system robustness. Notably, two generators that previously had minimal or no generation now operate at stable output levels between 100 MW and 200 MW, as shown in Figure 5(b). Additionally, all generators exhibit significantly reduced fluctuations in output, maintaining more consistent power generation levels. This adjustment ensures a more resilient generation mix, mitigating the impact of renewable energy variability on power system stability.

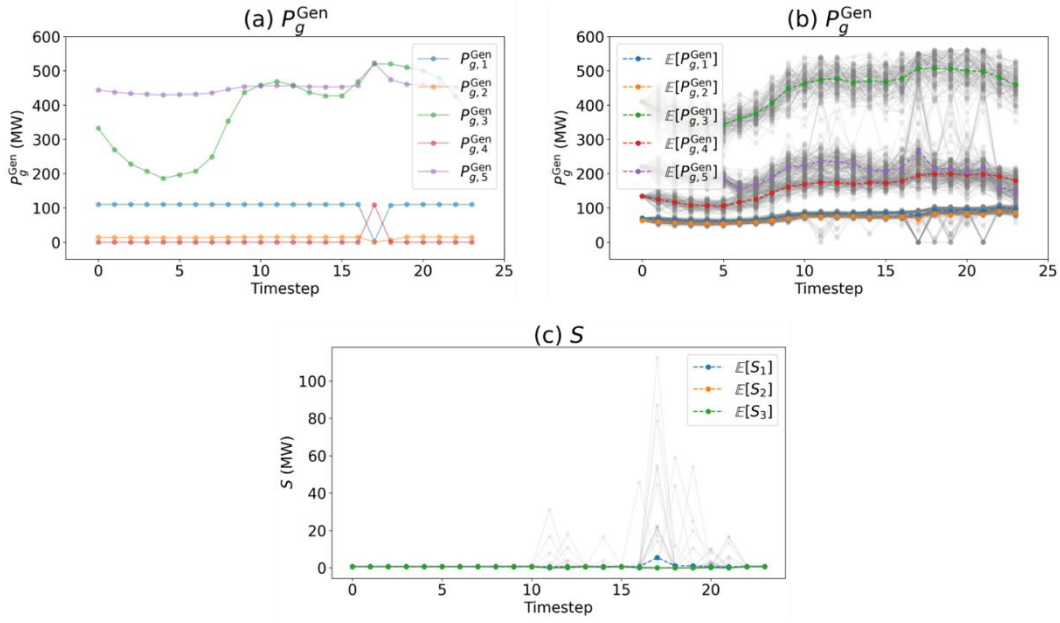

Figure 5 Optimization solution of (a) P_g^{Gen} under original demand scenario, (b) P_g^{Gen} under 100 demand scenarios, and (c) S under 100 demand scenarios

The results also demonstrate its effectiveness in managing load shedding risks under uncertainty. Figure 5(c) indicates that, while some scenarios still experience power shortages, the model enables a risk-informed approach to decision-making, ensuring that reliability is maintained without excessive overexpansion. By incorporating buffered failure probability constraints, the optimization effectively balances system security and economic efficiency, allowing for robust planning that accounts for uncertain scenarios while minimizing unnecessary interventions.

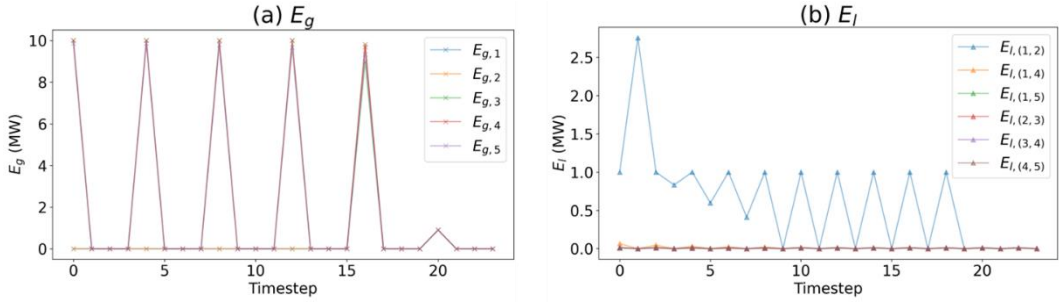

Figure 6 Optimization solution of (a) E_g, and (b) E_l under 100 demand scenarios

In terms of expansion planning, the results reveal a notable increase in generation capacity in Figure 6. The optimization strategically allocates additional generation resources to enhance overall system reliability, particularly in Figure 6(a). Conversely, transmission network expansion remains relatively limited, as depicted in Figure 6(b). The findings suggest that, due to the optimized local generation strategy, the demand is met primarily through distributed generation, thereby reducing the necessity for additional transmission capacity. This outcome underscores the

efficiency of meeting demand through localized generation, which minimizes reliance on long-distance power transmission and lowers overall infrastructure investment costs.

5 CONCLUSIONS

This study explores probabilistic weather modeling and risk-aware power network expansion planning using an extended DC-OPF formulation as complementary approaches to support strategic decision-making in renewable energy transitions. By capturing key dependencies among weather variables through a Bayesian Network and incorporating buffered failure probability constraints into the optimization model, this work provides insights into uncertainty quantification and risk-informed expansion strategies. While these two components were developed separately, their integration could further enhance the robustness of long-term power network planning. Future research will focus on applying this framework to a real-world case study in the United Kingdom, assessing its effectiveness in guiding practical renewable energy transition strategies.

ACKNOWLEDGEMENTS

This work was supported by the National Research Foundation of Korea (NRF) grant (No. RS-2024-00144434) funded by the Korea government (Ministry of Science and ICT).

REFERENCES

Byun, J. E., & Royset, J. O. (2022). Data-driven optimization of reliability using buffered failure probability. *Structural Safety*, 98, 102232.

Byun, J. E., de Oliveira, W., & Royset, J. O. (2023). S-BORM: Reliability-based optimization of general systems using buffered optimization and reliability method. *Reliability Engineering & System Safety*, 236, 109314.

Rockafellar, R. T., & Uryasev, S. (2000). Optimization of conditional value-at-risk. *Journal of Risk*, 2, 21-42.

Rockafellar, R. T., & Royset, J. O. (2010). On buffered failure probability in design and optimization of structures. *Reliability Engineering & System Safety*, 95(5), 499-510.

Royset, J. O. (2025). Risk-adaptive approaches to stochastic optimization: A survey. *SIAM Review*, 67(1), 3-70.

Salmeron, J., Wood, K., & Baldick, R. (2004). Analysis of electric grid security under terrorist threat. *IEEE Transactions on Power Systems*, 19(2), 905-912.

Seok, U., Byun, J. E., & Song, J. Comparing Conventional and Buffered Failure Probability from the Perspective of Risk-based Decision-Making. In *Proc. 14th International Conference on Application of Statistics and Probability in Civil Engineering (ICASP14)*.

Seok, U., Byun, J. E., & Song, J. (2025). Disaster risk-informed optimization using buffered failure probability for regional-scale building retrofit strategy. *Structural Safety*, 114, 102556.

Sun, J., & Tesfatsion, L. (2007). Open-source software for power industry research, teaching, and training: A DC-OPF illustration. In *2007 IEEE Power Engineering Society General Meeting* (pp. 1-6). IEEE.

Sparsity-promoting Design under Uncertainty to Maximize Stable Energy Production with Char Combustion

Yulin Guo[a,*], Dongjin Lee[b,*], Boris Kramer[a,**]

[a] *Department of Mechanical and Aerospace Engineering, University of California San Diego, CA, United States*
[b] *Department of Automotive Engineering, Hanyang University, Seoul, South Korea*

March 14, 2025

Abstract

This work presents a design under uncertainty approach for a char combustion problem with limited data, where simulations of the fluid-solid coupled system are computationally expensive. A polynomial dimensional decomposition (PDD) surrogate model is integrated into the design optimization and computational efficiency is induced in three key areas. First, the input random variables are transformed to have fixed probability measures, eliminating the need to recalculate the PDD's basis functions associated with these probability quantities. Second, the PDD coefficients are estimated using the limited data from a physics-based high-fidelity solver via sparsity-promoting diffeomorphic modulation under observable response preserving homotopy regression. Third, a single-pass surrogate model training process is proposed to avoid the need to generate new training data and update the PDD coefficients during the derivative-free optimization process. The results provide insights for optimizing process parameters to ensure consistently high energy production from char combustion.

1. Introduction

Biomass power plants convert organic materials, including wood, agricultural residues, and dedicated energy crops, into electricity and heat through combustion. The complex and multiscale biomass combustion process is subject to uncertainties in fuel variability, operating conditions, and emission measurement uncertainties [1, 20], which makes it difficult to control and predict the outcomes of biomass combustion. To achieve consistent energy production with biomass combustion, it is essential to optimize the process while taking into account these uncertainties. A design under uncertainty (DUU) framework allows one to maximize combustion efficiency and minimize fluctuations in the produced thermal energy. The straightforward approach for DUU requires evaluating the objective function, and possibly constraints, by repeatedly sampling uncertain inputs according to their joint distribution and conducting physics-based simulations. Surrogate models can be used within design optimization as cheaper-to-evaluate computational models, yet with the caveat of introducing model error. The surrogate models include, but are not limited to, polynomial chaos expansion (PCE) [17, 18] and polynomial dimensional decomposition (PDD) [9, 10, 15, 16], Kriging [21, 24, 7], copula-based surrogates [14], reduced-order modeling [22], and artificial neural networks (ANN) [3]. To reliably optimize, the surrogate model needs to be accurate, which may require a substantial amount of high-quality training data from the costly physics-based model. Moreover, within the optimization, one may have to retrain the surrogate model as the design variables change.

In this study, we formulate and solve a DUU problem for a char combustion process in a limited-data setting, since the multiscale fluid-solid combustion simulation is computationally expensive. Our contributions are as follows: (a) The optimization problem is formulated with transformed input

*These two authors contributed equally to this work.
**Corresponding author
Email address: bmkramer@ucsd.edu; +1 858-246-5327 (Boris Kramer)

random variables, whose probability measures remain fixed throughout design iterations, therefore, recalculating associated probability quantities is unnecessary. (b) A sparsity-promoting diffeomorphic modulation under observable response-preserving homotopy (sD-MORPH) regression approach is used to accurately train a PDD surrogate model from limited data. (c) We develop a single-pass surrogate model training process that estimates the objective function at current design variable values using the initially calculated PDD coefficients. This approach avoids the need for input-output data from costly physics-based models at each optimization iteration. (d) The single-pass surrogate model training process benefits from a derivative-free design method, offering advantages over gradient-based optimization solvers, which are sensitive to noisy and nonsmooth outputs [12, 13].

The paper is organized as follows. Section 2 overviews the DUU problem, relevant physics-based models, and design optimization formulation. Section 3 introduces the char combustion model and the computational domain, and defines the quantity of interest. Section 4 covers the DUU problem, including the formulation of the design optimization problem and the surrogate model that works with limited data. Section 5 presents numerical results, and Section 6 concludes with future outlook.

2. Problem description

The goal of the optimization is to find the optimal operation parameters that maximize the produced thermal energy of a char combustion process and minimize its variation under uncertainties.

We simulate the char combustion process in a lab-scale rectangular boiler (Figure 1) with the PIC method, as detailed in Section 3. The quantity of interest (QoI) is the thermal energy Q generated over a specified time interval, defined in (2) and depends on five uncertain inputs $\mathbf{X}$ (see Table 1).

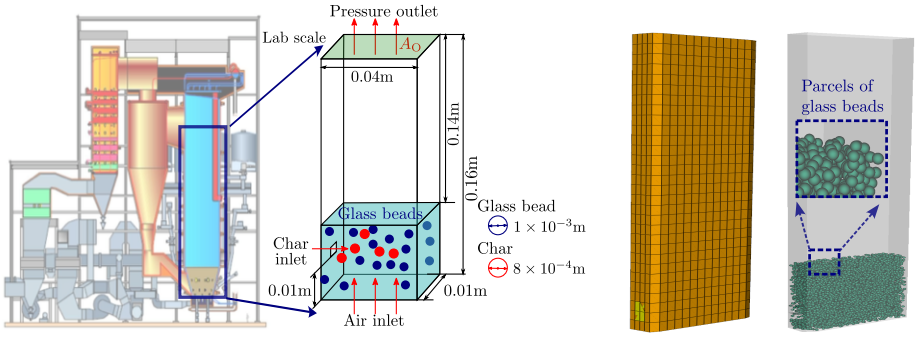

(a) Geometry model (b) Computational model

Figure 1: Fluidized bed furnace: (a) an industrial-scale model of the fluidized bed furnace (left) is scaled down to a lab-scale version (right), which details the geometry and initial conditions with the diameters of glass beads and char particles, the air inlet, and char inlet; (b) in one simulation using the PIC method, we use 2,520 cells to discretize the fluid (left) and the parcel model uses 8,344 parcels to predict solid behavior (right).

The DUU problem aims to maximize thermal energy while minimizing its variation. The objective function is a weighted sum of the first two statistical moments of Q. Specifically, we formulate the DUU problem as:

$$\min_{\mathbf{d}\in\mathcal{D}\subseteq\mathbb{R}^n} w_1 \frac{\mu_0}{\mathbb{E}_{\mathbf{d}}[Q(\mathbf{X};\mathbf{d})]} + w_2 \frac{\sqrt{\mathbb{V}\mathrm{ar}_{\mathbf{d}}[Q(\mathbf{X};\mathbf{d})]}}{\sigma_0}, \tag{1}$$

where $\mu_0 \in \mathbb{R}\setminus\{0\}$ and $\sigma_0 \in \mathbb{R}\setminus\{0\}$ are two non-zero, real-valued scaling factors; $\mathbf{d}$ is the vector of n design variables; $\mathcal{D} := \times_{k=1}^{n}[d_{k,L}, d_{k,U}]$ is the design space, where $d_{k,L}$ and $d_{k,U}$ are the lower and upper bounds of the kth design variable. The design variables are the distribution parameters, in this case the mean values, of a subset of the random inputs $\mathbf{X}$ that influence Q the most. The subset is chosen based on variance-based global sensitivity analysis in our previous work [11]. Here, $\mathbb{E}_{\mathbf{d}}[\cdot]$ and $\mathbb{V}\mathrm{ar}_{\mathbf{d}}[\cdot]$ are the expectation and variance operators, respectively, with respect to the probability measure $f_{\mathbf{X}}(\mathbf{x};\mathbf{d})\mathrm{d}\mathbf{x}$, which depends on $\mathbf{d}$. Weights $w_1 \in \mathbb{R}_0^+$ and $w_2 \in \mathbb{R}_0^+$ satisfy $w_1 + w_2 = 1$.

3. Computational model for char combustion

To predict the biomass combustion behavior, it is crucial to describe the behaviors of particles and gases in the combustor. Considering both accuracy and efficiency, we select the PIC method to efficiently describe the behavior of millions of particles and gases. The PIC model treats the gas phase as a continuous medium using the Eulerian method. The model uses the Lagrangian method for the solids phase, grouping particles into parcels based on their physical properties (e.g., density, diameter). This simplification of the particle kinetics, rather than using the full Newtonian equation, also increases computational efficiency. For more details on PIC, refer to [11].

In PIC, a collisional stress model accounts for interactions among particles and interactions between particles and walls [19]. The collision stress is expressed as $\tau = P_s \epsilon_s^{\beta} / \max(\epsilon_{cp} - \epsilon_s,\ \alpha(1-\epsilon_s))$, where $P_s = 1.0$ is the empirical pressure constant, ϵ_s is the particle volume fraction, $\beta = 2.0$ is the empirical unit-less exponent, ϵ_{cp} is the maximum possible packing fraction for particles, and $\alpha = 10^{-9} \ll 1$. The combustion process generates two gas products, CO and CO_2, from the heterogeneous (gas-solid) and homogeneous (gas-gas) reactions

$$\mathrm{C(Solid)} + 0.5\mathrm{O_2(Gas)} \rightarrow \mathrm{CO(Gas)}, \qquad \mathrm{CO(Gas)} + 0.5\mathrm{O_2(Gas)} \rightarrow \mathrm{CO_2(Gas)}.$$

The collisions among particles and between particles and the wall lead to the ash falling off the particles, following an Arrhenius kinetic rate and gas diffusion rate [23]. The homogeneous reaction can be calculated by the law of mass action via the Arrhenius formula, proposed by Dryer and Glassman [6].

Figure 1a shows the lab-scale rectangular furnace model (40 mm × 160 mm × 10 mm) with stacked glass beads at the bottom, enhancing combustion through improved mixing, heat transfer, and reaction rate due to their fluidization properties, high sphericity, and durability [8, 5] in char combustion. Char particles are introduced at a constant rate via a 2 mm × 2 mm inlet on the left wall, reacting with oxygen from the air inflow at the bottom. The model includes five random inputs: heights of glass beads, diameters of glass beads and char particles, and inflow rates of char and air, detailed in Section 5. The gas phase computational mesh consists of 2,520 cells, each with six degrees of freedom (three velocity components and three scalar variables: temperature, species concentrations, and pressure), totaling 15,120 degrees of freedom. The parcel weight is set to 3 (each parcel containing three particles). Due to randomness in the freeboard height and particle diameters, the total particle count varies per simulation. In Figure 1b, 8,344 parcels represent the glass beads in the model. We use the open-source software MFiX (version 23.1.1) [4] with an MPI-based parallel computing solver on 15 CPUs (Intel Xeon W-3175X CPU 3.10 GHz) for the combustion simulations.

Our quantity of interest (QoI) is the total thermal energy generated in 10 seconds, computed as

$$Q(\mathbf{X}) = \int_{t=0}^{t=10} \dot{Q}(\mathbf{X}, t)\mathrm{d}t = \int_{t=0}^{t=10} C_p(\mathbf{X}, t) \times \dot{m}(\mathbf{X}, t) \times T_{\mathrm{avg}}(\mathbf{X}, t)\mathrm{d}t, \tag{2}$$

where $T_{\mathrm{avg}}(\mathbf{X}, t)$ is the average temperature at the pressure outlet (at the top of the boiler model, c.f. Figure 1) at time t and inputs $\mathbf{X}$; $\dot{m}(\mathbf{X}, t)$ is the mass flow rate at the outlet and $C_p(\mathbf{X}, t)$ is the specific heat capacity of the mixture of O_2, N_2, CO, CO_2 and H_2O, i.e., $C_p(\mathbf{X}, t) = \sum_{i=1}^{5} C_{pi}(\mathbf{X}, t) \times M_i(\mathbf{X}, t)$. Here, C_{pi} is the specific heat capacity of each gas component in the mixture and M_i is the mole fraction of each gas component, such that $\sum_{i=1}^{5} M_i = 1$. The specific heat capacity C_{pi} is a function of the gas constant, the molecular weight of the gas, and the temperature and coefficients obtained from [2].

We validate the PIC-based computation model with the DEM results from [23, Fig. 2], focusing on the time evaluation of gas mass fractions for CO and CO_2. The root-mean-squared error between the DEM data and the data from our PIC-based solver for mass fractions at 5-second intervals over 40 seconds (see [11], Figure 6) is 2.73%. This indicates that the PIC model is accurate and validated compared to the computational model used in [23].

4. Design under uncertainty

4.1. Problem setup and definitions

We define random variables in a measurable space with a sample space and probability measures. Since the measurable space depends on the design vector $\mathbf{d}$, we include $\mathbf{d}$ in the notation for the variables and operators. We denote the measurable space by $(\Omega_{\mathbf{d}},\ \mathcal{F}_{\mathbf{d}})$, where $\Omega_{\mathbf{d}}$ is the sample space and $\mathcal{F}_{\mathbf{d}}$ is a σ-field on $\Omega_{\mathbf{d}}$. A family of probability measures $\{\mathbb{P}_{\mathbf{d}} :\ \mathcal{F}_{\mathbf{d}} \to [0,1]\}$ is defined over $(\Omega_{\mathbf{d}},\ \mathcal{F}_{\mathbf{d}})$. The input random vector $\mathbf{X} \coloneqq (X_1,\ X_2,\ \ldots,\ X_N)^\top$ describes uncertainties in the system, $N \in \mathbb{N}$. It is an $\mathbb{A}^N$-valued vector with $\mathcal{B}^N$ as the Borel σ-field on $\mathbb{A}^N$, $(\Omega_{\mathbf{d}},\ \mathcal{F}_{\mathbf{d}}) \to (\mathbb{A}^N,\ \mathcal{B}^N)$. The probability law of $\mathbf{X}$ is defined by a family of the joint probability density functions (PDFs) $\{f_{\mathbf{X}}(\mathbf{x};\mathbf{d}) : \mathbf{d} \in \mathbb{R}^N, \mathbf{d} \in \mathcal{D}\}$ associated with probability measures $\{\mathbb{P}_{\mathbf{d}} :\ \mathbf{d} \in \mathcal{D}\}$.

In this study, we define the random variables as the height of the freeboard (X_1), the air inflow rate (X_2), the diameter of the glass bead particle (X_3), the diameter of the char particle (X_4), and the char mass inflow rate (X_5) so $N = 5$. The n-dimensional design vector is $\mathbf{d} \coloneqq (d_1,\ d_2,\ \ldots,\ d_n)^\top \in \mathcal{D}$, where $\mathcal{D}$ is the design space. Here, each design variable represents the mean of the random variable, i.e., $d_k = \mathbb{E}[X_{i_k}]$, $k = 1,\ldots,n$ and $i_k \in \{1,\ldots,N\}$. Only the mean values of the most influential random variables are chosen as the design variables, specifically the mean values of the air inflow rate and the diameter of the glass bead particle based on variance-based global sensitivity analysis in [11], setting $n = 2$. We assume $Q(\mathbf{X};\mathbf{d})$ is a real-valued, square-integrable, measurable transformation on $(\Omega_{\mathbf{d}},\ \mathcal{F}_{\mathbf{d}})$, representing the quantity of interest.

4.2. Design under uncertainty formulation with transformed random variables

We keep the probability measure of the random variable fixed throughout the design iterations by formulating the design problem with the transformed random variable $\mathbf{Z}$, eliminating the need to recalculate probability measure-associated quantities. We define $\mathbf{Z} = (Z_1, Z_2, \ldots, Z_N)^\top$ as an N-dimensional vector of new random variables obtained by scaling $\mathbf{X}$ as $\mathbf{Z} \coloneqq \mathrm{diag}[r_1, r_2, \ldots, r_N]\mathbf{X}$, where $\mathbf{r} \coloneqq (r_1, r_2, \ldots, r_N)^\top$ is an N-dimensional vector of deterministic variables. The PDF of $\mathbf{Z}$ is

$$f_{\mathbf{Z}}(\mathbf{z};\mathbf{g}) = |\mathbf{J}| f_{\mathbf{X}}(\mathbf{x};\mathbf{d}) = \left|\frac{1}{r_1 r_2 \cdots r_N}\right| f_{\mathbf{X}}(\mathbf{x};\mathbf{d}) = \left|\frac{1}{r_1 r_2 \cdots r_N}\right| f_{\mathbf{X}}\left(\mathrm{diag}\left[\frac{1}{r_1}, \frac{1}{r_2}, \ldots, \frac{1}{r_N}\right]\mathbf{z};\mathbf{d}\right)$$

supported on $\bar{\mathbb{A}}^N \subseteq \mathbb{R}^N$. The absolute value of the determinant of the Jacobian is $|\mathbf{J}| = |\partial\mathbf{x}/\partial\mathbf{z}| = 1/(r_1 r_2 \ldots r_N)$ and $\mathbf{g} \coloneqq (g_1, g_2, \ldots, g_n)^\top \in \mathbb{R}^n$ is an n-dimensional vector of mean values. We choose g_k to be *one*. Thus, $\mathbf{g} = \mathbf{1}$ and at every iteration, $r_k = 1/d_k$.

We define $h(\mathbf{Z};\mathbf{r}) \coloneqq Q(\mathbf{X})$, so we can reformulate (1) to

$$\min_{\mathbf{d}\in\mathcal{D}\subseteq\mathbb{R}^n} w_1 \frac{\mu_0}{\mathbb{E}_{\mathbf{g}(\mathbf{d})}[h_0(\mathbf{Z};\mathbf{r})]} + w_2 \frac{\sqrt{\mathbb{V}\mathrm{ar}_{\mathbf{g}(\mathbf{d})}[h_0(\mathbf{Z};\mathbf{r})]}}{\sigma_0} \tag{3}$$

where $\mathbb{E}_{\mathbf{g}(\mathbf{d})}$ and $\mathbb{V}\mathrm{ar}_{\mathbf{g}(\mathbf{d})}$ are the expectation and variance operators, respectively, with respect to the probability measure $f_{\mathbf{Z}}(\mathbf{z};\mathbf{g})\mathrm{d}\mathbf{z}$, which depends on $\mathbf{d}$. For brevity, the subscript $\mathbf{g}(\mathbf{d})$ will be denoted by $\mathbf{g}$ in the rest of the paper. The transformed formulation in (3) is expressed in terms of the transformed input random variables $\mathbf{Z}$ and is equivalent to the original formulation in (1).

4.3. Polynomial dimensional decomposition (PDD) surrogate model

Any square-integrable function $h(\cdot)$ on $(\Omega_{\mathbf{d}}, \mathcal{F}_{\mathbf{d}}, \mathbb{P}_{\mathbf{d}})$ can be represented with an infinite Fourier-polynomial expansion known as polynomial dimensional decomposition (PDD) [15, 16]. By retaining only the degrees of interaction among input variables that are less than or equal to S, we have the S-variate, mth-order PDD approximation

$$h_{S,m}(\mathbf{Z};\mathbf{r}) = \sum_{i=1}^{L_{N,S,m}} c_i(\mathbf{r})\Psi_i(\mathbf{Z};\mathbf{g}) \approxeq h(\mathbf{Z};\mathbf{r}), \tag{4}$$

where $\Psi_i(\mathbf{Z};\mathbf{g})$ is the ith basis function and $L_{N,S,m} = 1 + \sum_{s=1}^{S} \binom{N}{s}\binom{m}{s}$.

4.4. Statistical moment analysis via the PDD surrogate

We use the S-variate, mth-order PDD surrogate $h_{S,m}(\mathbf{Z};\mathbf{r})$ to estimate the mean and variance of $h(\mathbf{Z};\mathbf{r})$. The orthonomality of the basis functions allows for the analytical formulation of the mean and the variance of $h(\mathbf{Z},\mathbf{r})$ as $\mathbb{E}_{\mathbf{g}}[h_{S,m}(\mathbf{Z};\mathbf{r})] = c_1(\mathbf{r}) = \mathbb{E}_{\mathbf{g}}[h(\mathbf{Z};\mathbf{r})]$, and $\mathbb{V}\mathrm{ar}_{\mathbf{g}}[h_{S,m}(\mathbf{Z};\mathbf{r})] = \sum_{i=2}^{L} c_i^2(\mathbf{r}) \leq \mathbb{V}\mathrm{ar}_{\mathbf{g}}[h(\mathbf{Z};\mathbf{r})]$, respectively. This necessitates accurate computation of the expansion coefficients to obtain good estimates for the mean and variance of $h(\mathbf{Z};\mathbf{r})$. To achieve this, particularly when the training data set is limited, we use a regression method called sD-MORPH regression [11], which is detailed in the following section.

4.5. Regression problem and solution from limited data

The coefficients $\mathbf{c} = (c_1, c_2, \ldots, c_L)^\intercal \in \mathbb{R}^L$ of the PDD surrogate discussed in Section 4.3 can be obtained by solving

$$\underbrace{\begin{bmatrix} \Psi_1(\mathbf{z}^{(1)};\mathbf{g}) & \cdots & \Psi_L(\mathbf{z}^{(1)};\mathbf{g}) \\ \vdots & \ddots & \vdots \\ \Psi_1(\mathbf{z}^{(M)};\mathbf{g}) & \cdots & \Psi_L(\mathbf{z}^{(M)};\mathbf{g}) \end{bmatrix}}_{=:\mathbf{A}} \underbrace{\begin{bmatrix} c_1 \\ c_2 \\ \vdots \\ c_L \end{bmatrix}}_{\mathbf{c}} = \underbrace{\begin{bmatrix} h(\mathbf{z}^{(1)};\mathbf{r}) \\ h(\mathbf{z}^{(2)};\mathbf{r}) \\ \vdots \\ h(\mathbf{z}^{(M)};\mathbf{r}) \end{bmatrix}}_{=:\mathbf{b}}. \tag{5}$$

To solve this with limited data ($M < L$), it is common to use LASSO regression, which penalizes the l^1 norm of the coefficients $\mathbf{c}$, producing sparse solutions for underdetermined systems.

However, LASSO regression introduces a bias to reduce variance and cannot infer more non-zero coefficients than the number of training samples. A sparsity-promoting D-MORPH regression leverages the sparsity from LASSO regression and iteratively improves its accuracy by combining it with the D-MORPH solution. In sD-MORPH, we define a cost function that measures the difference between a potential sD-MORPH solution $\mathbf{a}(t) \in \mathbb{R}^L$ and the LASSO estimates $\mathbf{c}_0 \in \mathbb{R}^L$ to obtain an initial sD-MORPH solution $\breve{\mathbf{c}}^{(0)} = \arg\min_{t\in\mathbb{R}} \left\{\frac{1}{2}(\mathbf{a}(t)-\mathbf{c}_0)^\intercal(\mathbf{a}(t)-\mathbf{c}_0)\right\}$. Next, we augment the cost function by including the l^2 norm between the potential sD-MORPH solution $\breve{\mathbf{c}}^{(i)}$ and the solution obtained from the previous iteration $\breve{\mathbf{c}}^{(i-1)}$. We can then iteratively solve for sD-MORPH solution by minimizing $[\frac{\lambda}{2}\left(\breve{\mathbf{c}}^{(i)}-\mathbf{c}_0\right)^\intercal \mathbf{W}\left(\breve{\mathbf{c}}^{(i)}-\mathbf{c}_0\right) + \frac{1-\lambda}{2}\left(\breve{\mathbf{c}}^{(i)}-\breve{\mathbf{c}}^{(i-1)}\right)^\intercal \mathbf{W}\left(\breve{\mathbf{c}}^{(i)}-\breve{\mathbf{c}}^{(i-1)}\right)]$, where $\lambda \in [0,1]$ and $\mathbf{W}$ is a diagonal weighting matrix based on $\breve{\mathbf{c}}^{(i-1)}$ such that large weights are assigned corresponding to smaller components of $\breve{\mathbf{c}}^{(i-1)}$.

4.6. Single-pass surrogate model training process

We use a single-pass surrogate model training process to reduce the total number of high-fidelity solutions needed. We assume that (a) an mth-order PDD approximation $h_{S,m}(\mathbf{Z};\mathbf{r})$ at the initial design is valid for all possible designs; (b) the PDD coefficients for a new design, computed by recycling PDD generated for the previous design, remain accurate.

We denote the transformation vectors associated with the previous and current designs with $\mathbf{r}$ and $\mathbf{r}'$, respectively. To satisfy the two assumptions, we use $m = 11$ and limit the design space to be represented by the PDD model computed at the initial design. We first compute the PDD coefficients $c_i(\mathbf{r})$, $i = 1, 2, \ldots, L_{S,N,m}$, collectively denoted as $\mathbf{c}(\mathbf{r})$, for the initial design using the input-output data $\{\mathbf{z}^{(l)}, h(\mathbf{z}^{(l)};\mathbf{r})\}_{l=1}^{L_{S,N,m}}$. For the next design in the optimization process, we modify the input data $\{\mathbf{z}^{(l)}\}_{l=1}^{L_{S,N,m}}$ to $\{\mathbf{z}'^{(l)}\}_{l=1}^{L_{S,N,m}}$, where $\mathbf{z}'^{(l)} = \mathrm{diag}[r_1/r_1', r_2/r_2', \ldots, r_N/r_N']\mathbf{z}^{(l)}$. We then represent the QoI at the updated design $\mathbf{r}'$ in terms of $\mathbf{z}'$ as $h(\mathbf{z}^{(l)};\mathbf{r}') := h(\mathrm{diag}[1/r_1', 1/r_2', \ldots, 1/r_N']\ \mathbf{z}^{(l)}) = h(\mathrm{diag}[1/r_1, 1/r_2, \ldots, 1/r_N]\ \mathrm{diag}[r_1/r_1', r_2/r_2', \ldots, r_N/r_N']\ \mathbf{z}^{(l)}) = h(\mathrm{diag}[1/r_1, 1/r_1, \ldots, 1/r_N]\ \mathbf{z}'^{(l)}) =: h(\mathbf{z}'^{(l)};\mathbf{r})$. This modification allows us to approximate the output function $h(\mathbf{z}^{(l)};\mathbf{r}')$ at the updated design $\mathbf{r}'$ via PDD computed at the initial design $\mathbf{r}$ as $h(\mathbf{z}^{(l)};\mathbf{r}') = h(\mathbf{z}'^{(l)};\mathbf{r}) \approx \sum_{i=1}^{L_{S,N,m}} c_i(\mathbf{r})\Psi_i(\mathbf{z}'^{(l)};\mathbf{g}) =: \tilde{h}(\mathbf{z}^{(l)};\mathbf{r}')$, which does not require updating the PDD, only evaluating the PDD at the new input $\mathbf{z}'$. As a result, at every iteration, we estimate the mean and variance with $\mathbf{c}(\mathbf{r}')$, resulting in little extra computational cost.

4.7. Complete algorithm for design under uncertainty

Figure 2 shows a flow chart for the proposed sparsity-promoting DUU method. This algorithm begins with initialization that includes setting $\mathbf{d} = \mathbf{d}_0$ and all parameters (e.g., N, S, m, etc.) used in the design process. We construct the input-output data set using $M < L_{S,N,m}$ expensive combustion simulations. We transform the input vector $\mathbf{X}$ to $\mathbf{Z}$ to avoid updating the PDD's basis functions. The next step is to train the PDD using the input-output data via the sD-MORPH regression. We then estimate the mean and variance of the output using the PDD's coefficients as discussed in Section 4.4. Subsequently, a derivative-free optimization, such as the Nelder-Mead method used in this work, finds the optimal solution by converging through a single-pass training process that uses the PDD trained at the initial design $\mathbf{d}_0$.

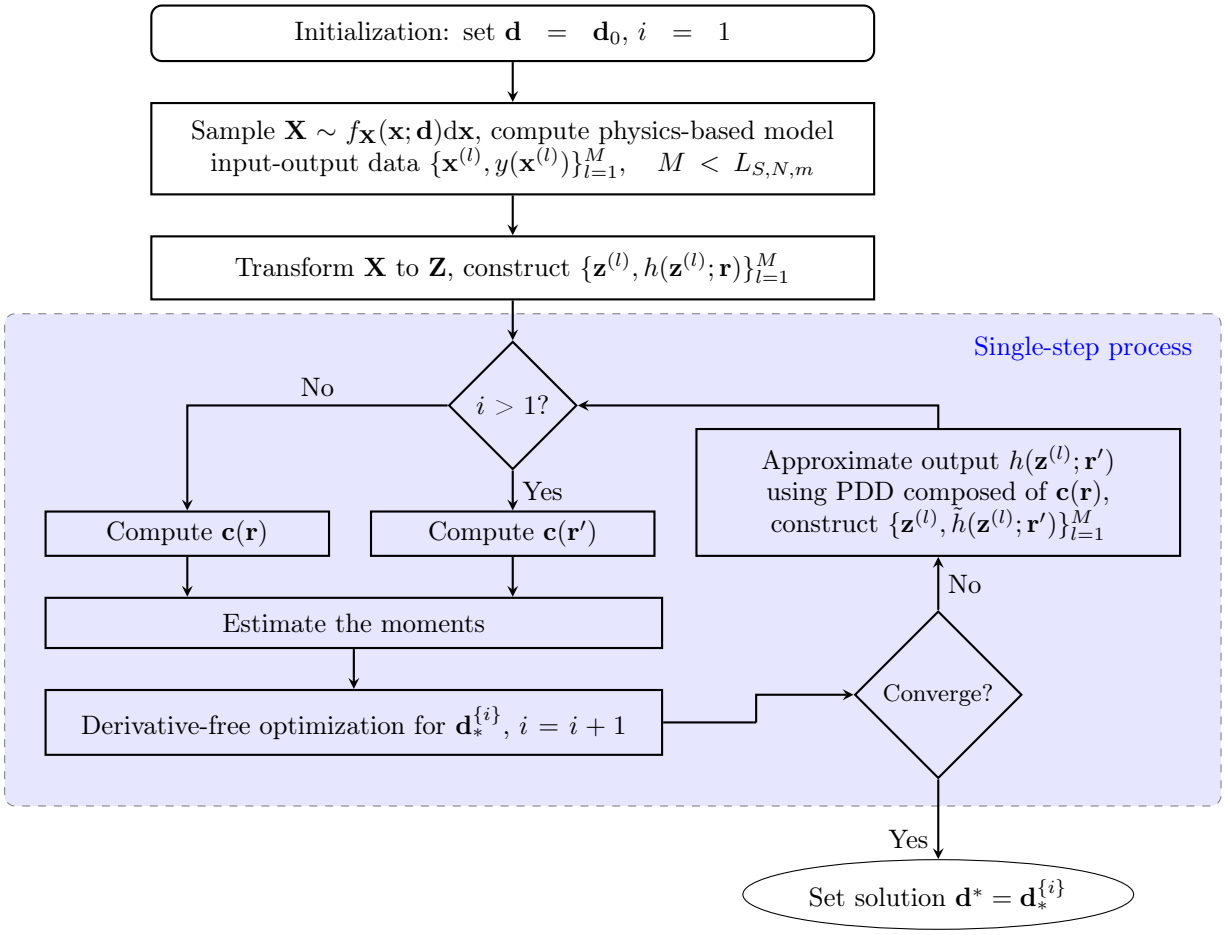

Figure 2: Flowchart for the sparsity-promoting DUU method.

5. Numerical results

5.1. Numerical setup

The PDD parameters in this work are $S = 2, N = 5$, and $m = 11$, with a computational budget of 1,600 CPU hours. Each MFiX run to obtain a sample of the input-output data takes 7.9 CPU hours, allowing for 200 samples to build the PDD surrogate model. With $L_{S,N,m} = 606$ basis functions,

$M = 200$ samples results in an underdetermined regression problem (5), as it covers only 33% of the 606 total unknown coefficients. Therefore, we use sD-MORPH to compute the PDD coefficients and compare the optimization results with coefficients calculated using LASSO regression. Table 1 shows the properties of the five random inputs. For the truncated normal random variables X_2 and X_3, the coefficients of variation are both 10%. Base on our previous work [11], we select the mean

Random Variable	Physical Quantity	Mean	Lower Boundary	Upper Boundary	Probability Distribution
X_1	Height of freeboard (m)	0.12	0.10	0.14	Uniform
X_2	Air inflow (m/s)	0.825	0.425	1.225	Truncated normal
X_3	Diameter of the glass bead particle (m)	8.0×10^{-4}	2.0×10^{-4}	1.4×10^{-3}	Uniform
X_4	Diameter of the char particle (m)	1.0×10^{-3}	5.0×10^{-4}	1.5×10^{-3}	Uniform
X_5	Char mass inflow (kg/s)	7.35×10^{-6}	1.35×10^{-6}	1.35×10^{-5}	Truncated normal

Table 1: Properties of the random inputs in a fluidized bed model for char combustion (reproduced from [11]).

values of X_2 and X_3 as design variables, i.e., $d_1 = \mathbb{E}[X_2]$ and $d_2 = \mathbb{E}[X_3]$, where $(d_1, d_2)^\intercal \in \mathcal{D} = [0.625, 1.025] \times [5 \times 10^{-4}, 1.1 \times 10^{-3}]$.

The goal of the study is to identify the two design values $(d_1, d_2)^\intercal$ that maximize the mean of the thermal energy $\mathbb{E}_{\mathbf{d}}[Q(\mathbf{X}; \mathbf{d})]$ while simultaneously minimizing its variance $\mathbb{V}\mathrm{ar}_{\mathbf{d}}[Q(\mathbf{X}; \mathbf{d})]$ under uncertainty, and given certain weights for both objectives, as shown in (1). The normorlizing constants μ_0 and σ_0 are chosen as the mean and standard deviation of the thermal energy $Q(\mathbf{X}; \mathbf{d})$ at the initial design $\mathbf{d}_0$.

We set the initial design vector $\mathbf{d}_0 = (0.825 \text{ m/s}, 8.0 \times 10^{-4} \text{ m})^\intercal$. To demonstrate the robustness of the proposed method with respect to sample number M, we tested four different sizes of training data (150, 170, 190, 200). Since the results showed a clear quantitative trend, we herein only report the cases of 150 and 200 samples used for training to ease readability in Sections 5.2.1 to 5.2.3. For comparison, we also apply the process using LASSO regression in place of sD-MORPH regression. In the sD-MORPH setting, the iteration number i of $\check{\mathbf{c}}^{(i)}$ discussed in Section 4.5 is set to at least 10 and λ is set to 0.2.

5.2. Results

5.2.1. Case (a): $w_1 = 1$ and $w_2 = 0$

This combination of weighting factors maximizes the mean of thermal energy, without considering its standard deviation. Figure 3a compares the optimization results obtained using LASSO-based and sD-MORPH-based DUU methods. We observe that the objective function value consistently decreases across all cases with different regression methods and different numbers of samples.

Using 200 training samples, at the initial design vector $\mathbf{d}_0 = (0.825 \text{ m/s}, \ 8.0 \times 10^{-4} \text{ m})^\intercal$, the mean values of the thermal energy esimated with the PDD surrogate coefficients using LASSO and sD-MORPH regressions are 1437.56J and 1436.78J, respectively. The optimal design vector is $\mathbf{d}^* = (1.025 \text{ m/s}, \ 5.0 \times 10^{-4} \text{ m})^\intercal$ for both methods, where the corresponding mean values of the thermal energy are 2017.08J (40.31% increase from initial design) and 2133.37J (48.48% increase), respectively. These results indicate that the sD-MORPH-based DUU method increases the mean of the thermal energy more. The results of DUU methods using 150 training samples are similar.

5.2.2. Case (b): $w_1 = 0$ and $w_2 = 1$

This combination of weighting factors minimizes the standard deviation of thermal energy, without considering its mean. With 200 training samples, the standard deviations of the thermal energy obtained using the LASSO-based and sD-MORPH-based DUU methods at the initial design are 185.13J and 198.67J, respectively. The optimal design vectors for the two methods are $(0.625 \text{ m/s}, \ 8.25 \times 10^{-4} \text{ m})^\intercal$ and $(0.709 \text{ m/s}, \ 7.96 \times 10^{-4} \text{ m})^\intercal$, respectively; the corresponding standard deviations of the thermal energy are 141.31J (23.67% decrease) and 168.85J (15.01% decrease), respectively. Compared to the LASSO-based method, the proposed sD-MORPH based method results in about 8% less reduction in the objective function value. This is because LASSO is limited by the number of non-zero

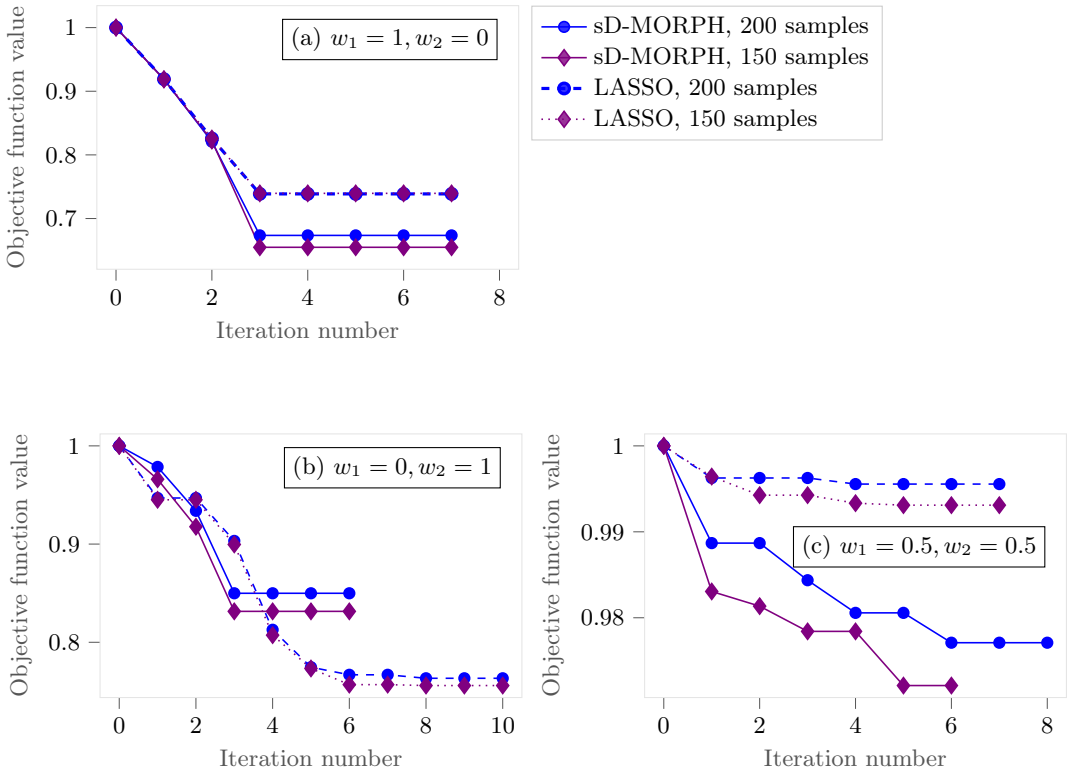

Figure 3: Change in objective function value with increasing iterations for different combinations of w_1 and w_2 in (1), comparison of LASSO-based and sD-MORPH-based design methods over different sample numbers (150 and 200).

values which is constrained by the number of training samples. As a result, the standard deviation (see Section 4.4) is often underestimated. In contrast, the sD-MORPH solution can produce small non-zero values, providing a more accurate representation of the true values.

In Figure 3b, we compare the optimization results obtained using LASSO and sD-MORPH-based DUU methods. The sD-MORPH version shows a faster drop of about 15% in the objective function within three iterations, whereas the LASSO version reduces the cost function by about 10% within the first three iterations. By the sixth iteration, the sD-MORPH version has converged, while the LASSO version is approaching convergence by the tenth iteration. The results of DUU methods with 150 training samples are similar.

5.2.3. Case (c): $w_1 = 0.5$ and $w_2 = 0.5$

This combination of weighting parameters corresponds to an optimization where the mean and standard deviation of the thermal energy are equally prioritized. Figure 3c shows the comparison of optimizations with LASSO-based and sD-MORPH-based methods. The objective function value consistently decreases across all cases with different regression methods and different numbers of samples.

For the LASSO-based method with 200 samples, the optimal design vector is $\mathbf{d}^* = (0.816\ \text{m/s}, 8.24 \times 10^{-4}\ \text{m})^\intercal$. The corresponding standard deviation is 184.32J, almost the same as 185.13J at the initial design. By comparison, for sD-MORPH-based method with 200 samples, the optimal design vector is $\mathbf{d}^* = (0.768\ \text{m/s}, 8.10 \times 10^{-4}\ \text{m})^\intercal$. The corresponding standard deviation is 173.94J (12.45% decrease). This shows that the optimization for equally weighted mean and standard deviation with sD-MORPH regression effectively reduces the standard deviation. The mean values of the thermal

energy corresponding to the LASSO-based and sD-MORPH-based DUU methods are 1437.56J and 1436.55J at the initial design, respectively; at the optimal designs, they are 1417.83J (1.37% decrease) and 1336.28J (6.98% decrease), respectively. The results when using 150 samples are similar.

6. Conclusion and future work

In this study, we proposed a design under uncertainty (DUU) problem for a char combustion process and solved it in a limited-data setting with a surrogate model. We used an sD-MORPH regression to calculate the coefficients of the PDD surrogate model in the optimization and reformulated the optimization problem using transformed input random variables combined with a single-pass training process. We conducted comparisons between DUU methods that use either a LASSO or an sD-MORPH-based surrogate model. The LASSO-based and sD-MORPH-based DUU yielded comparable improvements in thermal energy production when maximizing only the mean without accounting for the standard deviation. In another test where we only minimized the standard deviation, the sD-MORPH-based DUU converged faster than the LASSO-based approach. In a third case, we optimized both the mean and standard deviation of thermal energy, and found that the sD-MORPH-based method more effectively reduces standard deviation. An interesting future avenue is to extend this work to consider constraints, such as reliability or risk measures, in the optimization.

Acknowledgments

Y. Guo and B. Kramer were in part financially supported by the Korea Institute for Advancement of Technology (KIAT) through the International Cooperative R&D program (No. P0019804, Digital twin based intelligent unmanned facility inspection solutions). D. Lee was supported by the research fund of Hanyang University (HY-202300000003174).

References

[1] M. O. Andreae. Emission of trace gases and aerosols from biomass burning – an updated assessment. *Atmospheric Chemistry and Physics*, 19(13):8523–8546, 2019.

[2] Alexander Burcat and Branko Ruscic. Third millenium ideal gas and condensed phase thermochemical database for combustion (with update from active thermochemical tables). Technical report, Argonne National Lab.(ANL), Argonne, IL (United States), 2005.

[3] Tanmoy Chatterjee, Souvik Chakraborty, and Rajib Chowdhury. A critical review of surrogate assisted robust design optimization. *Archives of Computational Methods in Engineering*, 26:245–274, 2019.

[4] Mary Ann Clarke and Jordan M. Musser. The MFiX particle-in-cell method (MFiX-PIC) theory guide. Technical report, National Energy Technology Laboratory (NETL), Pittsburgh, PA, 2020.

[5] Heping Cui and John R Grace. Fluidization of biomass particles: A review of experimental multiphase flow aspects. *Chemical Engineering Science*, 62(1-2):45–55, 2007.

[6] Frederick L Dryer and I Glassman. High-temperature oxidation of CO and CH4. In *Symposium (International) on Combustion*, volume 14, pages 987–1003. Elsevier, 1973.

[7] Ruichen Jin, Xiaoping Du, and Wei Chen. The use of metamodeling techniques for optimization under uncertainty. *Structural and Multidisciplinary Optimization*, 25:99–116, 2003.

[8] Krittin Korkerd, Zongyan Zhou, Ruiping Zou, Pornpote Piumsomboon, and Benjapon Chalermsinsuwan. Numerical investigation of mixing and heat transfer of mixed biomass and silica sand particles in a bubbling fluidized bed combustor. *Powder Technology*, 433:119262, 2024.

[9] Dongjin Lee and Boris Kramer. Bi-fidelity conditional value-at-risk estimation by dimensionally decomposed generalized polynomial chaos expansion. *Structural and Multidisciplinary Optimization*, 66(2):33, 2023.

[10] Dongjin Lee and Boris Kramer. Multifidelity conditional value-at-risk estimation by dimensionally decomposed generalized polynomial chaos-Kriging. *Reliability Engineering & System Safety*, 235:109208, 2023.

[11] Dongjin Lee, Elle Lavichant, and Boris Kramer. Global sensitivity analysis with limited data via sparsity-promoting D-MORPH regression: Application to char combustion. *Journal of Computational Physics*, 511:113116, 2024.

[12] Dongjin Lee and Sharif Rahman. Robust design optimization under dependent random variables by a generalized polynomial chaos expansion. *Structural and Multidisciplinary Optimization*, 63(5):2425–2457, 2021.

[13] Dongjin Lee and Sharif Rahman. High-dimensional stochastic design optimization under dependent random variables by a dimensionally decomposed generalized polynomial chaos expansion. *International Journal for Uncertainty Quantification*, 13(4), 2023.

[14] Yoojeong Noh, KK Choi, and Liu Du. Reliability-based design optimization of problems with correlated input variables using a Gaussian Copula. *Structural and Multidisciplinary Optimization*, 38:1–16, 2009.

[15] Sharif Rahman. A polynomial dimensional decomposition for stochastic computing. *International Journal for Numerical Methods in Engineering*, 76(13):2091–2116, 2008.

[16] Sharif Rahman. Extended polynomial dimensional decomposition for arbitrary probability distributions. *Journal of Engineering Mechanics*, 135(12):1439–1451, 2009.

[17] Xuchun Ren and Sharif Rahman. Robust design optimization by polynomial dimensional decomposition. *Structural and Multidisciplinary Optimization*, 48:127–148, 2013.

[18] Dongying E Shen and Richard D Braatz. Polynomial chaos-based robust design of systems with probabilistic uncertainties. *AIChE Journal*, 62(9):3310–3318, 2016.

[19] Dale M Snider. An incompressible three-dimensional multiphase particle-in-cell model for dense particle flows. *Journal of Computational Physics*, 170(2):523–549, 2001.

[20] Dominik Steiner and Christof Lanzerstorfer. Particulate emissions from biomass power plants: a practical review and measurement uncertainty issues. *Clean Technologies and Environmental Policy*, 26(4):1039–1048, 2024.

[21] Jian Wang, Zhili Sun, and Runan Cao. An efficient and robust Kriging-based method for system reliability analysis. *Reliability Engineering & System Safety*, 216:107953, 2021.

[22] Gary Weickum, Mike Eldred, and Kurt Maute. Multi-point extended reduced order modeling for design optimization and uncertainty analysis. In *47th AIAA/ASME/ASCE/AHS/ASC Structures, Structural Dynamics, and Materials Conference 14th AIAA/ASME/AHS Adaptive Structures Conference 7th*, page 2145, 2006.

[23] Jun Xie, Wenqi Zhong, and Yingjuan Shao. Study on the char combustion in a fluidized bed by CFD-DEM simulations: Influences of fuel properties. *Powder Technology*, 394:20–34, 2021.

[24] Meide Yang, Dequan Zhang, Chao Jiang, Xu Han, and Qing Li. A hybrid adaptive Kriging-based single loop approach for complex reliability-based design optimization problems. *Reliability Engineering & System Safety*, 215:107736, 2021.

Hierarchical Stochastic Ground Motion Models for Uncertainty Quantification in Earthquake Engineering

Maijia Su[a,c,**], Mayssa Dabaghi[b], Marco Broccardo[a,*]

[a]*Department of Civil, Environmental and Mechanical Engineering, University of Trento, Trento, Italy*
[b]*Department of Civil and Environmental Engineering, American University of Beirut, Beirut, Lebanon*
[c]*Department of Civil and Environmental Engineering, University of California, Berkeley, United States*

Abstract

With advancements in computational power and seismic data availability, stochastic ground motion models (GMMs) are gaining popularity. This study introduces *Hierarchical Stochastic Ground Motion Models*—a generative model designed to generate new GMs that resemble a given training GM dataset. The term "*hierarchical*" reflects the two-step formulation: (1) selecting a modulated filtered white noise model (MFWNM) to replicate a target record and (2) constructing a joint probability density function (PDF) for the parameters of the selected MFWNM, capturing record-to-record variability. The hierarchical GMM is validated by comparing specific statistical metrics derived from 1,001 real strong-motion records with those obtained from corresponding synthetic datasets. The comparison demonstrates that hierarchical stochastic GMMs generate ground motions with high statistical compatibility to real datasets, effectively replicating four key intensity measures (PGA, PGV, Arias intensity, and significant duration D_{5-95}) as well as linear and nonlinear response spectra.

Keywords: Synthetic ground motion, Model validation, Uncertainty quantification

1. Introduction

In earthquake engineering, a proper definition of seismic input is essential for structural seismic design and seismic risk assessment. This seismic input is typically represented by a suite of acceleration time series. In this context, a fundamental question is determining the number and types of ground motions (GMs) used for structural seismic analysis. In practice, engineers typically select a set of original or modified GM records to match a target response

*marco.broccardo@unitn.it
**maijia.su@unitn.it (PhD Candidate), maijiasu@berkeley.edu (Visiting PhD Student)

spectrum [1, 2]. However, this method has notable limitations: (1) selected GMs are specific historical records and may not recur in future earthquake events; (2) modifications to records can lead to a loss of physical significance, introducing unnatural frequency content or amplitude variations; and (3) the response spectrum alone is an incomplete measure, as it does not capture nonstationarity or the duration of GMs. These limitations result in a potentially improper representation of GM characteristics and uncertainty.

To address these limitations, this study proposes the use of *hierarchical stochastic ground motion models* (GMMs). The term "hierarchical" refers to a two-step model formulation: (1) selecting a modulated filtered white noise model (MFWNM) to replicate a target record, and (2) constructing a joint probability density function (PDF) for the parameters of the selected MFWNM, capturing record-to-record variability to simulate synthetic GMs. Hierarchical stochastic GMMs are *generative models* that generate new GMs resembling a given training GM dataset. This approach allows for the creation of diverse and representative seismic inputs without relying on non-recurrent historical records. Additionally, hierarchical stochastic GMMs avoid the issues associated with modifying existing records, as they directly generate synthetic GMs already calibrated to reflect desired properties and statistical characteristics. Moreover, hierarchical stochastic GMMs provide a comprehensive probabilistic representation of GM characteristics, including time-varying amplitudes, nonstationary frequency content, and duration. As such, they present a promising solution to overcome the limitations of traditional GM selection methods.

This conference paper presents a concise review of the formulation, fitting, and validation of hierarchical stochastic GMMs. Interested readers can refer to our preprint for more details [3].

2. Hierarchical Ground Motion Models: Formulation, Fitting and Validation

Hierarchical stochastic GMMs are generative models that consist of a training phase and a generation phase. A conceptual illustration of hierarchical stochastic GMMs is shown in Figure 1. Hierarchical GMMs differ from deep neural network models, such as variational autoencoders or diffusion models commonly used for image and text generation. Instead, hierarchical models

are based on modeling classical stochastic processes and joint probability density functions (PDFs). Specifically, a recorded GM is regarded as a sample drawn from a simplified physics-based stochastic process. This process assumes that the earthquake source (with sudden energy released from rupture) is presented by a broadband Gaussian white noise process. Then, the white noise passes through a parametric time-varying filter that represents the earth's media and local site effects. We denote this modulated filtered white noise model as $\mathcal{M}(\cdot) : (\boldsymbol{\theta}, \boldsymbol{Z}) \rightarrow \hat{A}_g(t)$, where $\boldsymbol{\theta}$ is the model parameter, $\boldsymbol{Z}$ is the white noise, and $\hat{A}_g(t)$ is the simulated process. As a result, the hierarchical models do not have the black-box nature of deep neural networks or require complex training procedures, making them more transparent and interpretable.

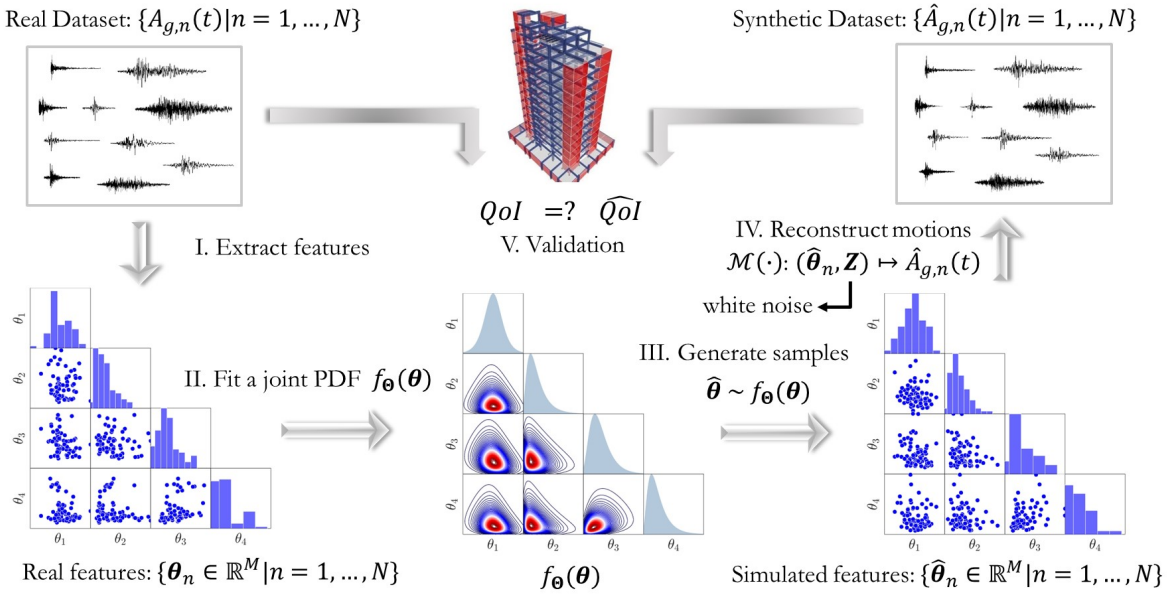

Figure 1: Illustration of hierarchical stochastic ground motion models, including (I) and (II) as fitting phrases, (III) and (IV) as generation phrases, and (IV) for validation.

The model starts with selecting a real dataset of ground motion acceleration time series, denoted as $\{A_{g,n}(t)|n = 1, ..., N\}$. This dataset is selected based on the ergodic assumption, i.e., the long-term temporal variability (at a specific site) can be represented by spatial variability (i..e, records across different sites with similar scenario parameters). This study selects a subset from the PEER NGA-West2 database [4, 5]. The subset comprises 1,001 strong motions ($N = 1,001$), selected based on the following criteria: (1) earthquake moment magnitudes (M_w) greater than 6, (2) source-to-site distances (R) is between 10 and 100 km, (3) the shear-wave velocity of superficial soil is set as $V_{S30} > 360$ m/s, and (4) pulse-like records are excluded.

In the training phase, the models extract key GM parameters (or features) $\boldsymbol{\theta} \in \mathbb{R}^M$ related to motion duration, frequency content, and total energy. These parameters form a low-dimensional feature space where a joint PDF $f_{\boldsymbol{\Theta}}(\boldsymbol{\theta})$ is built to capture the centers, dispersion, and dependencies among the parameters. The joint PDF is built by fitting marginal distributions to each parameter and modeling their Gaussian dependence using the Nataf transformation. This study selects the spectral-based stochastic GMM [6] as $\mathcal{M}(\cdot)$, which comprises 11 parameters, i.e., $M = 11$. The fitting procedures in [6] are used to extract the parameters $\boldsymbol{\theta}_n$ of n-th records. Additionally, a key parameter, termed corner frequency f_c, is estimated by the procedure outline in [7]. The definition of the 11 parameters and their fitted marginals (including distribution types, moments, and supports) are listed in Table 1. The histogram of the extract parameters, their fitted marginals, and the Gaussian dependency structure are visualized in Figure 2.

Table 1: Fitted marginal distributions of the 11 GM Parameters.

No.	**GM Parameter**	**Marginal**	**Moments**		**Distribution support**	**Unit**
			μ	σ		
1	$\log(I_a)$	Gaussian	-5.557	1.896	(-Inf, Inf)	$\log(g^2 \cdot \mathrm{s})$
2	$\omega(t_{mid})$	Lognormal	28.446	19.112	(0, Inf)	$2\pi \cdot$ Hz
3	$\omega'(t_{mid})$	Laplace	-0.227	1.003	(-Inf, Inf)	$2\pi \cdot$ Hz/s
4	$\zeta(t_{mid})$	Weibull	0.448	0.190	[0.02, 1]	1
5	D_{0-5}	Gamma	7.320	3.507	[0.1, 20]	s
6	D_{5-30}	Weibull	4.811	2.869	[0.1, 15]	s
7	D_{30-45}	Gamma	1.684	1.202	[0.1, 10]	s
8	D_{45-75}	Gamma	4.549	2.672	[0.1, 20]	s
9	D_{75-95}	Gumbel	10.271	4.664	[0.1, 40]	s
10	D_{95-100}	Lognormal	38.737	47.634	[0.1, 40]	s
11	f_c	Gamma	0.239	0.259	[0, 2]	Hz

*All GM parameters are used in [6, 7], with definitions: (1) $\log(I_a)$ is logarithmic Arias intensity (2); $\omega_g(t_{mid})$ is the predominant frequency at the middle of the strong-shaking phase; (3) $\omega_g'(t_{mid})$ is the change rate of the frequency $\omega_g(t_{mid})$; (4) $\zeta_g(t_{mid})$ is the filter bandwidth at the middle of the strong-shaking phase; (5) intervals $D_{p_i-p_{i+1}}$ refer to motion duration from p_i to p_{i+1} percentiles of the total energy; and (6) corner frequency f_c is a key parameter [7], which controls the proportion of low-frequency energy.

In the generative phrase, a set of "fake" parameters $\{\hat{\boldsymbol{\theta}}_{\boldsymbol{n}} | n = 1, ..., N\}$ is generated from the fitted joint PDF $f_{\boldsymbol{\Theta}}(\boldsymbol{\theta})$. These simulated parameters represent potential combinations of GM characteristics that are statistically consistent with the real dataset. Next, each sampled feature vector $\hat{\boldsymbol{\theta}}_{\boldsymbol{n}}$, paired with a white noise sample $\boldsymbol{z}_n$, is input into the GMM $\mathcal{M}(\cdot)$, obtaining a synthetic ground motion time series, denoted as $\mathcal{M}(\cdot) : (\hat{\boldsymbol{\theta}}_{\boldsymbol{n}}, \boldsymbol{z}_n) \rightarrow \hat{A}_{g,n}(t)$.

Finally, model validation is performed by comparing statistical metrics computed from the real dataset with those derived from the corresponding synthetic dataset. These metrics relate to quantities of interest (QoI), which include key seismic performance indicators such as ground motion intensity measures (e.g., peak ground acceleration (PGA), peak ground velocity (PGV), Arias intensity (I_a), and significant duration (D_{5-95})) as well as the response of idealized single-degree-of-freedom structures (i.e., linear and nonlinear response spectra). To account for the inherent uncertainty of white noise, 30 independent synthetic datasets are generated. Figure 3 presents a comparison of cumulative distribution functions (CDFs) for four IMs derived from the real and synthetic datasets. Additionally, Figure 4 validates three quantiles ($q_{1\%}$, $q_{50\%}$ and $q_{99\%}$) of both linear and nonlinear response spectra. In these figures, blue lines represent the real dataset, gray lines represent the 30 synthetic datasets, and red lines indicate the mean of the synthetic datasets. These figures demonstrate that hierarchical stochastic models can generate synthetic GM datasets that are statistically compatible with real strong-motion data.

3. Summary and Future Work

This study introduces hierarchical stochastic ground motion models (GMMs) for simulating nonpulse-like ground motion (GM) time series. Hierarchical GMMs take advantage of advancements in computational power and data availability. The synthetic GMs can be used for structural analysis, design, and risk assessments. Additionally, hierarchical GMMs incorporate a well-defined probabilistic model, supporting the effective application of Uncertainty Quantification in earthquake engineering. In particular, by integrating advanced structural-reliability sampling methods (such as important sampling and subset simulation), hierarchical stochastic GMMs provide clear and consistent answers on the number and types of ground motions needed for structural analysis. Moreover, hierarchical GMMs can be adapted to be site-based GM generators (similar to [8, 9, 10]) by linking the model parameters to seismological variables such as M_w, R, and V_{s30}.

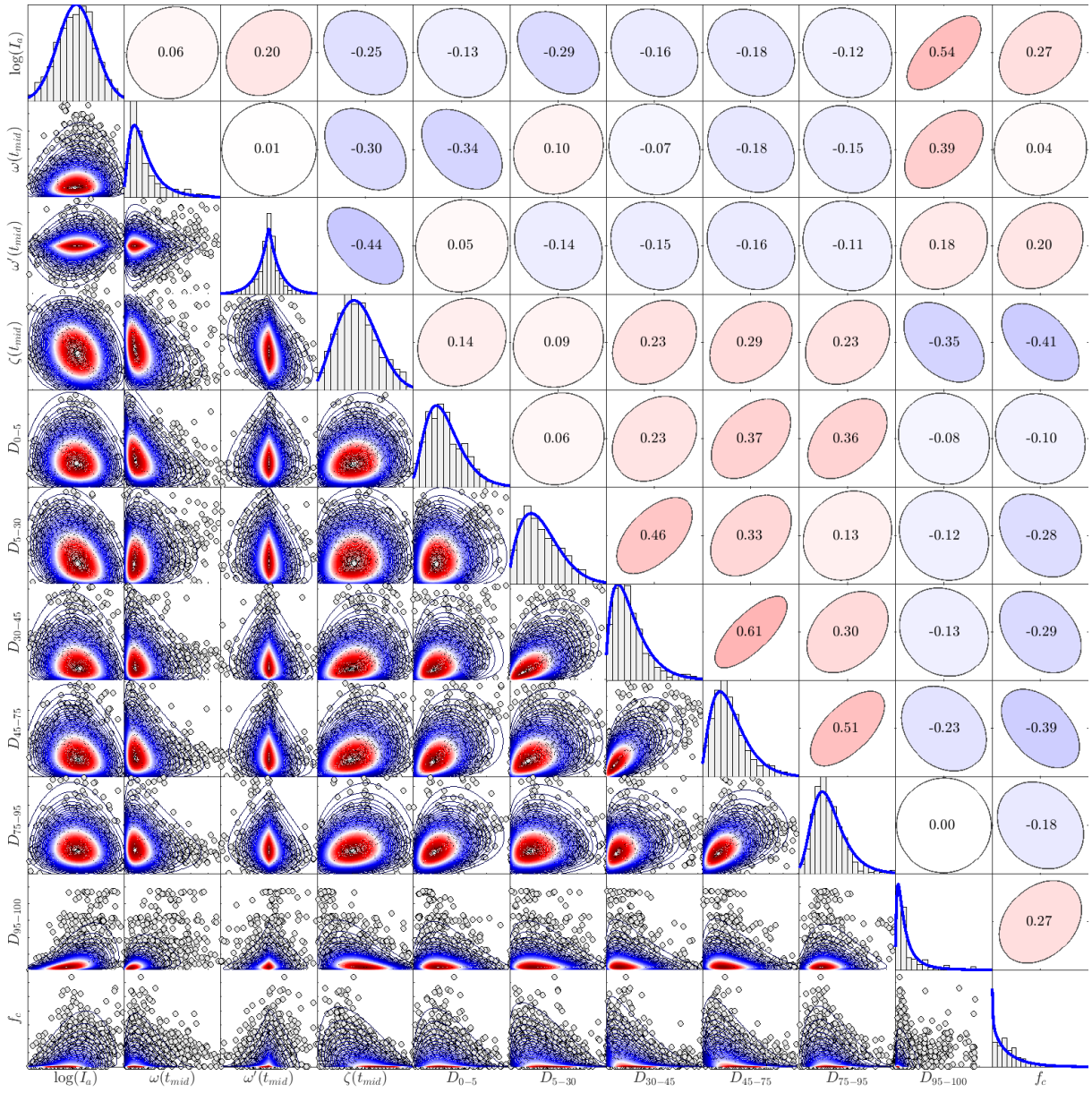

Figure 2: Visualization of the fitted joint PDF $f_{\boldsymbol{\Theta}}(\boldsymbol{\theta})$ with (i) upper triangle: Pearson's correlation coefficients of each parameter pair; (ii) diagonal positions: histograms and fitted PDF for each parameter and (iii) lower triangle: bi-variate distribution and observed data points

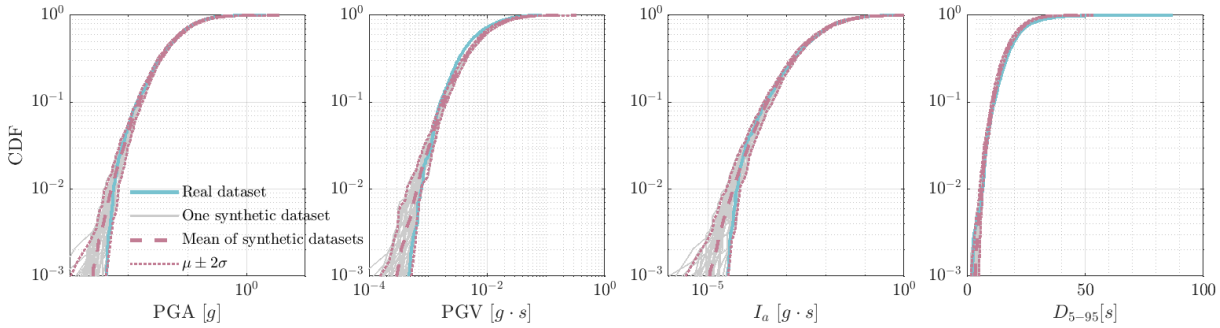

Figure 3: Validation of the hierarchical GMM w.r.t. CDFs of four intensity measures: PGA, PGV, Arias intensity I_a, and significant duration D_{5-95}.

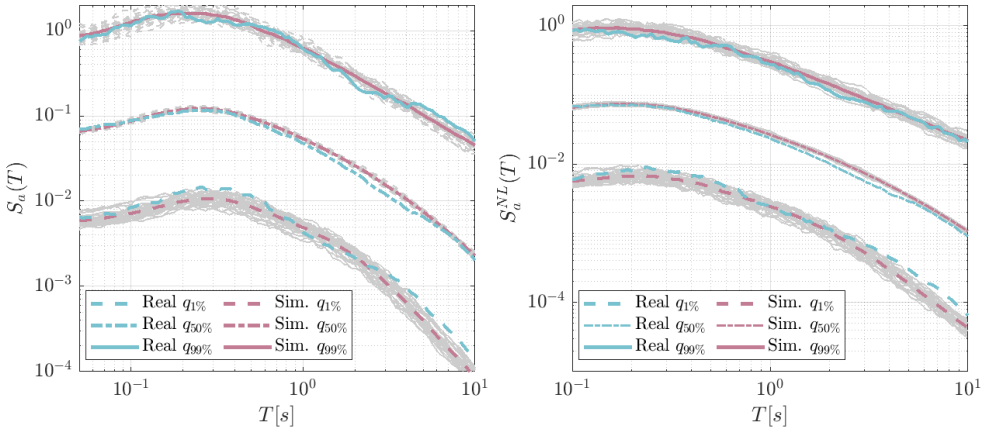

(a) Linear response spectrum

(b) Nonlinear response spectrum

Figure 4: Validation of the hierarchical GMMs using train-test split w.r.t. (a) three quantiles of 5%-damped linear-response spectra and (b) three quantiles of constant-ductility ($\mu = 2$) nonlinear-response spectra.

References

[1] F. Naeim, A. Alimoradi, S. Pezeshk, Selection and Scaling of Ground Motion Time Histories for Structural Design Using Genetic Algorithms, Earthquake Spectra 20 (2) (2004) 413–426, publisher: SAGE Publications Ltd STM. doi:10.1193/1.1719028.
URL https://doi.org/10.1193/1.1719028

[2] I. Iervolino, G. Manfredi, A Review of Ground Motion Record Selection Strategies for Dynamic Structural Analysis, in: O. S. Bursi, D. Wagg (Eds.), Modern Testing Techniques for Structural Systems: Dynamics and Control, CISM International Centre for Mechanical Sciences, Springer, Vienna, 2008, pp. 131–163. doi:10.1007/978-3-211-09445-7_3.
URL https://doi.org/10.1007/978-3-211-09445-7_3

[3] M. Su, M. Dabaghi, M. Broccardo, Review and validation of stochastic ground motion models: which one does it better?, arXiv preprint arXiv:2411.07401 (2024).

[4] Y. Bozorgnia, N. A. Abrahamson, L. A. Atik, T. D. Ancheta, G. M. Atkinson, J. W. Baker, A. Baltay, D. M. Boore, K. W. Campbell, B. S.-J. Chiou, et al., Nga-west2 research project, Earthquake Spectra 30 (3) (2014) 973–987. doi:10.1193/072113EQS209M.

[5] T. D. Ancheta, R. B. Darragh, J. P. Stewart, E. Seyhan, W. J. Silva, B. S.-J. Chiou, K. E. Wooddell, R. W. Graves, A. R. Kottke, D. M. Boore, et al., Nga-west2 database, Earthquake Spectra 30 (3) (2014) 989–1005. doi:10.1193/070913EQS197M.

[6] M. Broccardo, M. Dabaghi, A spectral-based stochastic ground motion model with a non-parametric time-modulating function, Vol. 2017, 12th International Conference on Structural Safety & Reliability, ICOSSAR, TU Wien Vienna, Austria, 2017, pp. 1–10.

[7] M. Su, M. Dabaghi, M. Broccardo, The importance of corner frequency in site-based stochastic ground motion models, Earthquake Engineering & Structural Dynamics 53 (10) (2024) 3318–3329, _eprint: https://onlinelibrary.wiley.com/doi/pdf/10.1002/eqe.4139. doi:10.1002/eqe.4139.
URL https://onlinelibrary.wiley.com/doi/abs/10.1002/eqe.4139

[8] S. Rezaeian, A. Der Kiureghian, Simulation of orthogonal horizontal ground motion components for specified earthquake and site characteristics, Earthquake Engineering & Structural Dynamics 41 (2) (2012) 335–353, _eprint: https://onlinelibrary.wiley.com/doi/pdf/10.1002/eqe.1132. doi:10.1002/eqe.1132.
URL https://onlinelibrary.wiley.com/doi/abs/10.1002/eqe.1132

[9] C. Vlachos, K. G. Papakonstantinou, G. Deodatis, Predictive model for site specific simulation of ground motions based on earthquake scenarios, Earthquake Engineering & Structural Dynamics 47 (1) (2018) 195–218, _eprint: https://onlinelibrary.wiley.com/doi/pdf/10.1002/eqe.2948. doi:10.1002/eqe.2948.
URL https://onlinelibrary.wiley.com/doi/abs/10.1002/eqe.2948

[10] M. Dabaghi, A. Der Kiureghian, Simulation of orthogonal horizontal components of near-fault ground motion for specified earthquake source and site characteristics, Earthquake Engineering & Structural Dynamics 47 (6) (2018) 1369–1393, _eprint: https://onlinelibrary.wiley.com/doi/pdf/10.1002/eqe.3021. doi:10.1002/eqe.3021.
URL https://onlinelibrary.wiley.com/doi/abs/10.1002/eqe.3021

Long-range Ising model for performance-based earthquake engineering at a regional scale

Sebin Oh[a], Sangri Yi[a], Ziqi Wang[a,*]

[a]*Department of Civil and Environmental Engineering, University of California, Berkeley, United States*

Abstract

This study introduces the long-range Ising model from statistical mechanics to the Performance-Based Earthquake Engineering (PBEE) framework for regional seismic damage analysis. The application of the PBEE framework at a regional scale involves estimating the damage states of numerous structures, typically performed using fragility function-based stochastic simulations. However, these simulations often assume independence or employ simplistic dependency models among capacities of structures, leading to significant misrepresentation of risk. The Ising model addresses this issue by converting the available information on binary damage states (safe or failure) into a joint probability mass function, leveraging the principle of maximum entropy. The Ising model offers two main benefits: (1) it requires only the first- and second-order cross-moments, enabling seamless integration with the existing PBEE framework, and (2) it provides meaningful physical interpretations of the model parameters, facilitating the uncovering of insights not apparent from data. To demonstrate the proposed method, we applied the Ising model to 156 buildings in Antakya, Turkey, using post-hazard damage evaluation data, and to 182 buildings in Pacific Heights, San Francisco, using simulated data from the Regional Resilience Determination (R2D) tool. In both instances, the Ising model accurately reproduces the provided information and generates meaningful insights into regional damages. The study also investigates the change in Ising model parameters under varying earthquake magnitudes, along with the mean-field approximation, further facilitating the applicability of the proposed approach.

1. Introduction

A large-scale simulation for regional behavior under hazards is necessary to assess and improve the resilience of infrastructure and communities. While physics-based simulations can accurately capture the complex interactions and correlations among structural responses and functionalities, their extensive computational cost often limits its usage to scenario-based analyses. On the other hand, stochastic simulations of the performance state (or damage state) given a hazard scenario are computationally feasible but require many ad hoc, sometimes subjective, assumptions about statistical models.

For regional seismic analysis, the performance state of each building is typically sampled from fragility function-based stochastic simulations. The fragility function, the probability of exceeding different damage states given a ground motion intensity measure, is typically given by

$$\mathbb{P}\left(DS \geq ds_i | IM = im\right) = \Phi\left(\frac{\ln\left(im/\theta_i\right)}{\beta_i}\right), \tag{1}$$

where ds_i represents the ith performance state, IM denotes the ground motion intensity at the location of the structure, $\Phi(\cdot)$ is the standard Gaussian cumulative distribution function, θ_i is the median of IM causing the

*Corresponding author
Email address: ziqiwang@berkeley.edu (Ziqi Wang)

performance state ds_i or greater, and β_i denotes the log standard deviation of IM that induces the damage ds_i or greater. The current practice for applying the Performance-Based Earthquake Engineering (PBEE) framework to a regional scale employs individual fragility functions under the assumption of conditional independence (conditional on site-specific intensity measures of ground motions), which can significantly underestimate system-level failure probabilities [1, 2]. To achieve more reliable regional risk analysis, it is required to construct a fragility field that summarizes the joint information, beyond the collection of marginal information, across the region [3].

This study presents an alternative method for constructing the fragility field that can be integrated with fragility-based approaches, physics-based simulations, and even post-hazard survey data. Specifically, we introduce the Ising model, a widely recognized model in statistical mechanics, as a joint probability mass function for binary performance states (safe or failure) of structures over a region. The Ising model has been used in various disciplines to study collective behavior in complex systems, owing to its nature as the maximum entropy distribution for binary variables, subject to constraints on first- and second-order cross-moments. In this study, focusing on seismic risk, the formulation and interpretations of the Ising model in the context of regional seismic analysis are provided with the brief investigation of the dependence between the Ising model parameters and the observable statistics, e.g., mean and correlation coefficients. Inferences about regional seismic behaviors that are not apparent from the data are also presented through two examples using real-world post-hazard survey data and synthetic simulation data.

2. Long-range Ising model as a joint probability mass function for performance states

2.1. Formulation

Consider a region consisting of n structures under an earthquake and assume that each structure can be in one of the binary states of safe or failure. Here, safe and failure are relative terms with respect to a target performance level. The group of structures has $N = 2^n$ configurations, where the probability of the I-th configuration is expressed as:

$$P_I = \mathbb{P}\left(X_1 = x_{1I}, X_2 = x_{2I}, \ldots, X_n = x_{nI}\right) , \tag{2}$$

where $X_i \in \{-1 \text{ (safe)}, 1 \text{ (failure)}\}$ is a random variable representing the state of the i-th structure, and x_{iI} denotes an outcome of X_i for the I-th configuration.

The entropy S for $\boldsymbol{X} = [X_1, X_2, ..., X_n]^\intercal$ is defined as:

$$S \coloneqq -\sum_{I=1}^{N} P_I \log P_I. \tag{3}$$

In the absence of information, the probability distribution that maximizes the entropy is the uniform distribution, which means that all possible configurations are equally likely. Suppose we have information up to the second-order cross-moments expressed as follows:

$$\mathcal{M}_{1,i} = \sum_{I=1}^{N} x_{iI} P_I \,, \tag{4}$$

$$\mathcal{M}_{2,ij} = \sum_{I=1}^{N} x_{iI} x_{jI} P_I \,, i, j = 1, 2, ..., n \,, \tag{5}$$

where $\mathcal{M}_{1,i}$ is the first-order cross-moment, i.e., the mean of X_i, and $\mathcal{M}_{2,ij}$ is the second-order cross-moment between the damage states of the i-th and j-th structures. Applying Lagrange multipliers with $\mathcal{M}_{1,i}$ and $\mathcal{M}_{2,ij}$ as constraints, the joint probability P_I that maximizes the entropy S is:

$$P_I = \frac{1}{Z} \exp\left(\sum_{i=1}^{n} h_i x_{iI} + \sum_{i>j} J_{ij} x_{iI} x_{jI} \right) , \tag{6}$$

where Z is the normalizing constant given as:

$$Z = \sum_{I=1}^{N} \exp\left(\sum_{i=1}^{n} h_i x_{iI} + \sum_{i>j} J_{ij} x_{iI} x_{jI}\right), \tag{7}$$

where h_i and J_{ij} are the Lagrange multipliers to meet the first- and second-order cross-moment constraints, respectively. Since our goal is to model the joint distribution that outputs the probability for any specified configuration, we drop the subscript I in Eq. (6) and replace P_I by $p(\boldsymbol{x})$:

$$\begin{aligned} p(\boldsymbol{x}) &= \frac{1}{Z} \exp\left(\sum_{i=1}^{n} h_i x_i + \sum_{i>j} J_{ij} x_i x_j\right) \\ &= \frac{1}{Z} \exp\left(\boldsymbol{h}^\intercal \boldsymbol{x} + \frac{1}{2} \boldsymbol{x}^\intercal \boldsymbol{J} \boldsymbol{x}\right), \end{aligned} \tag{8}$$

where $\boldsymbol{x} = [x_1, x_2, \ldots, x_n]^\intercal$, $\boldsymbol{h} = [h_1, h_2, \ldots, h_n]^\intercal$, and:

$$\boldsymbol{J} = \begin{bmatrix} 0 & J_{12} & \ldots & J_{1n} \\ J_{12} & 0 & \ldots & J_{2n} \\ \vdots & \vdots & \ddots & \vdots \\ J_{1n} & J_{2n} & \ldots & 0 \end{bmatrix}. \tag{9}$$

Eq. (8) is the Ising model in statistical physics for describing ferromagnetism, where h_i and J_{ij} are typically interpreted as the external magnetic field acting on each component/spin and the pairwise coupling effects between each spin pair, respectively [4, 5]. While the classic Ising model features a sparse $\boldsymbol{J}$ because it considers only the pairwise coupling effects between neighboring spins on a lattice, Eq. (8) represents a *long-range* or *fully-connected* Ising model, accounting for interactions between all pairs of structures in a region.

2.2. Interpretations of the Ising model parameters

We interpret $\boldsymbol{h}$ as a risk field acting on each structure within a region. According to Eq. (8), a structure with a positive h_i is more probable to fail, i.e., to have a spin of $x_i = +1$, with a larger h_i signifying a greater tendency towards failure. Conversely, a negative risk field h_i indicates a tendency to remain safe. Given that civil structures are engineered to be reliable and safe, they should inherently possess an inertia toward safety, a negative field $-\mathcal{I}$ where $\mathcal{I} > 0$. A hazard imposes an external positive field $h_H > 0$ on each structure, and the resulting risk field is a balance between the hazard and the inertia towards remaining safe, i.e., $h_i = h_H - \mathcal{I}$. Here, both h_H and $\mathcal{I}$ vary across structures.

On the other hand, $\boldsymbol{J}$ represents the pairwise interactions, reflecting the tendency of two structures to be in the same damage states. The term interaction encompasses all direct and indirect effects stemming from physical and statistical properties that determine how the damage state of one structure can affect the state of another. From Eq. (4), it is observed that if J_{ij} is positive, the probability of two structures being in the same states is higher than them being in different states, with a larger J_{ij} increasing this probability. Conversely, a negative J_{ij} favors the damage states being different.

2.3. Dependency between the Ising model parameters and the traditional statistics

Calculation of the observable statistics, e.g., mean and correlation coefficient, from the Ising model requires calculating Eqs. (4) and (5) over 2^n configurations, which is generally infeasible. Accordingly, Monte Carlo sampling techniques are often used as an alternative to approximate statistics of interest, and specifically, Gibbs sampling is widely adopted for this purpose owing to its applicability to high-dimensional distributions and ease of implementation. Here, to briefly introduce the dependency between the Ising model parameters and the observable statistics, simple proof-of-concept examples are investigated.

Consider two binary random variables $X = [X_1, X_2]^\intercal \in -1(\text{safe}), +1(\text{failure})^2$ representing the damage states of two buildings. The risk field and pairwise interaction are given as $h_1 = h_2 = h$ and $J_{12} = J$, respectively. With only 2 variables and thus 2^2 system configurations, the exact mean and correlation coefficient for given h and J values can be determined using Eqs. (4)- (8). The mean value $\mathbb{E}[X_i]$ is directly linked to the failure probability P_f by $P_f = (\mathbb{E}[X_i] + 1)/2$. Note that, due to parameter settings of the current demonstration, the failure probability P_f for each building is identical.

Figure 1 depicts the relationship between the Ising model parameters and the mean and correlation coefficient of the damage states. It is observed from Figure 1a that, for any J value, the mean damage state $\mathbb{E}[X_i]$ is monotonically increasing with respect to h, reflecting that a stronger risk field results in a higher failure probability. Moreover, a negative pairwise interaction provides a buffer for a building against the risk field, while positive pairwise interaction increases a building's sensitivity to the risk field, amplifying its tendency towards failure. From Figure 1b, it is shown that, for any h value, the correlation coefficient ρ monotonically increases with respect to J. Increasing the absolute value of h makes the $\rho - J$ dependency weaker. It is of particular importance to note that the mean and correlation coefficient for the damage state are influenced by both the risk field acting on the site and the pairwise interaction from the other building.

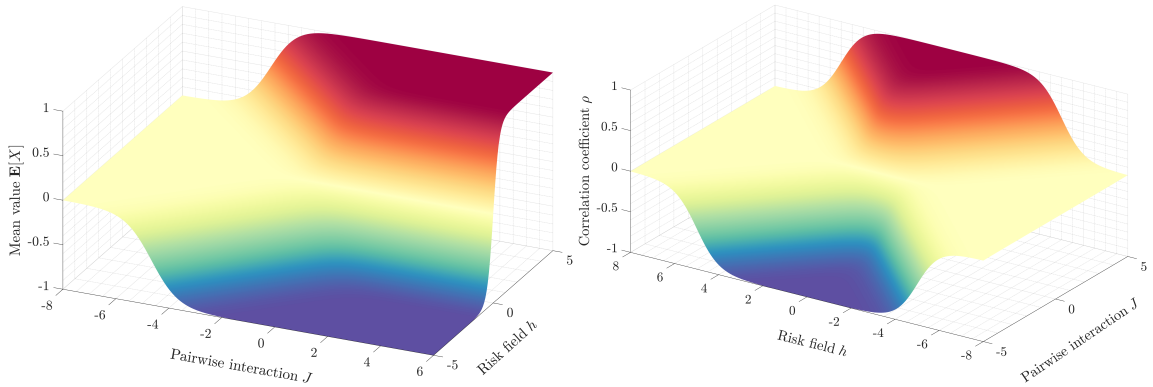

(a) (b)

Figure 1: **The relationship between the Ising model parameters and (a) the mean $\mathbb{E}[X_i]$, and (b) the correlation coefficient ρ for the demonstrative example of two buildings**

To further investigate the relationship between the correlation coefficient and pairwise interactions, we consider a scenario involving three buildings without a risk field. Figure 2 shows the J_{ij} values for each pair of buildings and the corresponding correlation coefficient values. In Figure 2a, despite having no direct interaction, i.e., $J_{AB} = 0$, buildings A and B exhibits a correlation of 0.58, which is attributed to the significant pairwise interactions between buildings A and C and between buildings C and B. Additionally, Figure 2b demonstrates that buildings A and B have a zero correlation coefficient, despite a large positive J value of 0.66. This occurs because the indirect effects of the positive interaction between buildings A and C and the negative interaction between buildings B and C outweigh the direct interaction between buildings A and B.

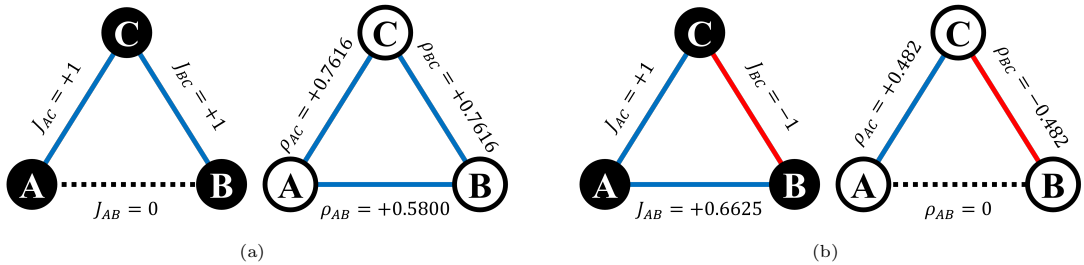

(a) (b)

Figure 2: **Demonstrative systems describing the dependency between the correlation coefficient ρ and the pairwise interaction J: (a) a 3-node system with zero pairwise interaction and (b) with zero correlation coefficient between nodes A and B**

The illustrations above briefly demonstrate the complex interplay between the Ising model parameters and both the mean and correlation coefficient. The mean damage state of a structure is primarily influenced by the risk field acting on it, although the pairwise interactions also contribute to either sharpening or diminishing this effect. Similarly, the correlation coefficient for the damage states between a pair of structures is influenced by all pairwise interactions involving those structures, with the magnitude of the risk field either amplifying or mitigating this effect. In essence, the Ising model, parameterized by h and J, provides a fundamental mechanism for generating the mean damage states and correlation coefficients.

3. Inferences on regional seismic behavior using the Ising model

Here, the engineering relevance of the Ising model in the context of regional seismic analysis is investigated. The required information to construct the Ising model is the first- and second-order cross-moments, Eqs. (4) and (5), for damage states of structures. These can be obtained from fragility curves and their correlation models [6] or be generated from regional seismic response simulators, such as the Regional Resilience Determination (R2D) tool of NHERI SimCenter [7], and the Interdependent Networked Community Resilience Modeling Environment (IN-CORE) platform of NCSA [8]. In this study, the Ising model is constructed using both post-earthquake damage evaluation data and samples generated by the R2D tool. The detailed procedures for constructing the Ising model from the data are omitted. The main findings on regional seismic behavior inferred from the Ising model for each target region are presented.

3.1. Example 1: Ising model from post-earthquake damage evaluation data

A neighborhood in Antakya, Turkey, following the 2023 Turkey-Syria earthquake is selected as the target region. The data on building damages is obtained from the Humanitarian OpenStreetMap (HOTOSM) team [9, 10]. Figure 3 illustrates the damage states for the target region, consisting of 156 buildings, 40 of which failed during the earthquake. Given that we have only a single observation under the earthquake event, we assume spatial ergodicity to obtain the correlation coefficients to construct the Ising model. Using the information about the number of failed buildings, 40 out of 156 buildings, and the correlation coefficient based on the ergodicity assumption, the Ising model is constructed.

Figure 3: **The building damage in a region of Antakya, Turkey, following the 2023 Turkey–Syria earthquake**. Out of 156 buildings, 40 failed, including 14 out of 72 failing in the inner area and 26 out of 84 failing in the outer area. The inner and outer areas are defined in the right panel; this definition will facilitate the verification of the Ising model predictions.

Once the Ising model is constructed, various inferences can be made about the regional seismic behavior. Using the Ising model, a total of 10^7 samples for the target region is generated. The failure probability for each building is then obtained, as illustrated in Figure 4a, which is not available from the given field survey. Figure 4a shows that closely spaced buildings exhibit an overall lower failure probability, consistent with the real observation in Figure 3, where about 19% (14 out of 72) of the buildings failed in the inner area while about 31% (26 out of 84) failed in the outer area. This result is consistent with the findings of Figure 1a. When the risk field is negative, strong pairwise interactions between closely spaced buildings create a buffer against failure. Conversely, this trend reverses when the risk field is positive.

Furthermore, Figure 4b illustrates a histogram of the number of failed buildings from the 10^7 samples. It is observed that the mode (most probable number of failed buildings) is around 25, although the expected number is about 39 (which is close to the input information that 40 out of 156 buildings failed). Moreover, the probability of more than 100 buildings failing is 3.85%, which is not negligible. This is because the distribution of the number of failed buildings has a long right tail. Indeed, it is well known that the Ising model exhibits bimodal for the global mean-field (number of failed buildings in this example) when pairwise interactions are large [4]. Although bimodality is only noticeable in Figure 4b, in regions with higher correlation coefficients, such as dense residential zones with similar houses, the bimodality would be more pronounced, and a collective failure would be non-negligible.

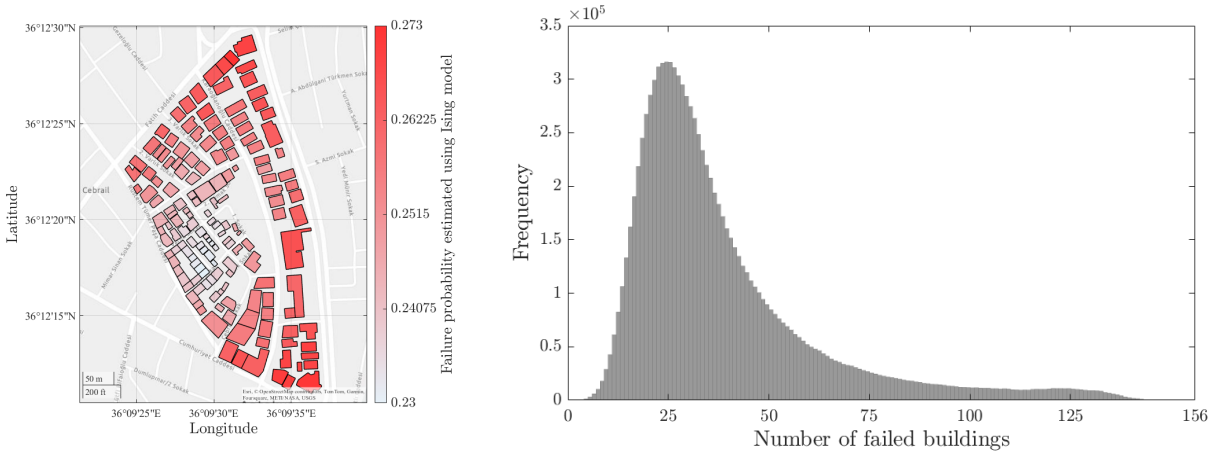

(a) (b)

Figure 4: **Inferences about the target region using the Ising model: (a) the individual failure probability of each building and (b) the histogram of the number of failed buildings**. The distribution features a long right tail with a small, yet noticeable, second model.

3.2. Example 2: Ising model based on fragility functions

In this example, the Ising model is constructed from samples generated by the R2D tool provided by the NHERI SimCenter. A neighborhood in Pacific Heights, San Francisco, is chosen as the modeled region, containing 182 buildings. An earthquake scenario of magnitude of 7.0 is assumed. The epicenter is on the San Andreas Fault, at latitude of 37.9, longitude of -122.432, with a depth of 80 kilometers. Given the earthquake scenario, the R2D computes peak ground accelerations (PGA) at each building site using the ground motion prediction equation developed in Boore et al. [11]. The models from Baker and Jayaram [6] and Markhvida et al. [12] are used to account for the inter- and intra-event spatial correlations in PGAs, respectively. Given the PGA values at each building site, the damage state for each building is evaluated using fragility curves provided by Hazus [13], leveraging structural information integrated into the R2D tool. This includes geographical location, plan area, year built, number of stories, and structural type of the buildings. Due to limitations in the current R2D tool, correlations between the capacities of buildings are not considered. Subsequently, 10,000 samples are generated, each sample being a vector representing the damage states for the 182 buildings.

Figure 5 compares the failure probabilities provided by the R2D tool with the risk field values derived from the Ising model, with the color bars indicating the rankings of buildings based on these two quantities, where 1 denotes the highest and 182 the lowest. The spatial patterns are overall similar, but differences are noticeable. These differences are highlighted in Figure 6 by comparing the risk fields to the failure probabilities, with the reference curve indicating independence between DSs. If all DSs are independent, the points should be distributed along the reference curve and the rankings from the two metrics will be identical. Additionally, if all points follow a monotonically increasing trend, the rankings are identical. In Figure 6, however, the risk field value varies significantly even for similar failure probabilities. This multiplicity is due to the interactions among structures. For instance, the building indexed as 108 stands out in Figure 6 as being distinctly close to the reference curve, implying that it is closest to independence. In fact, Figure 7 shows that building #108 deviates from the rest by having the smallest average pairwise interaction value. This suggests that the failure event of building #108 has a minimal effect on the state of the other buildings. Therefore, contrasting the risk field $\boldsymbol{h}$ with individual failure probabilities reveals the dominance of collective behavior among structures. The collective behavior directly alters the joint distribution; the effect reaches beyond second-order statistics.

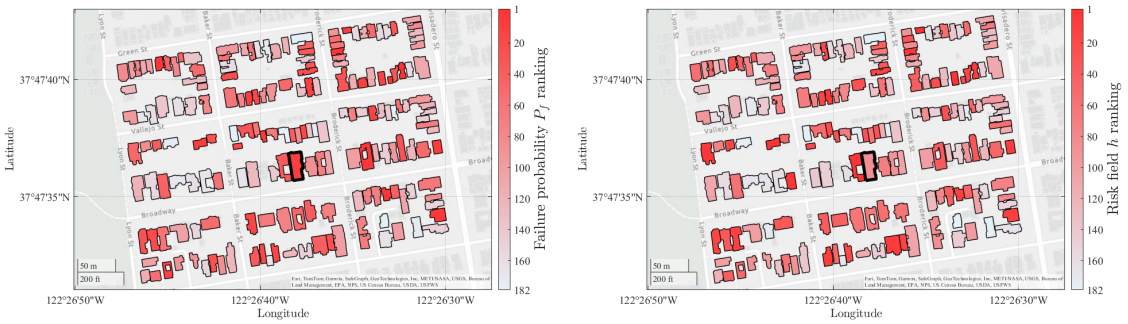

(a) (b)

Figure 5: **Illustrations of (a) the failure probabilities and (b) the risk field h values for each building in Pacific Heights, San Francisco.** Building #108, which is of particular importance, is highlighted by a bold black solid line.

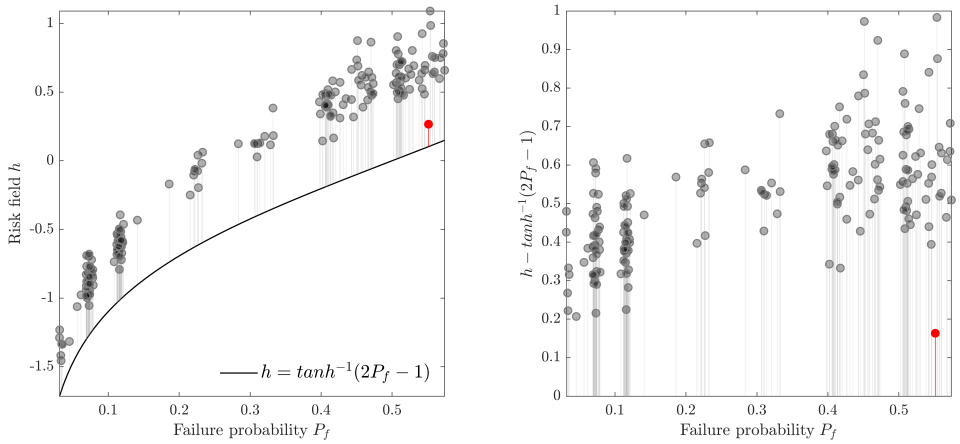

Figure 6: **Comparison between the risk fields and the failure probabilities**. The black solid curve in the left panel represents the exact relationship between h and P_f when the damage states are independent. The distance from each point to the reference curve of independence is visualized as a solid thin line, which is highlighted in the right panel. Building #108, marked in red, is identified as an outlier because, compared to other buildings with similar failure probabilities, its distance to the reference curve is distinctly small.

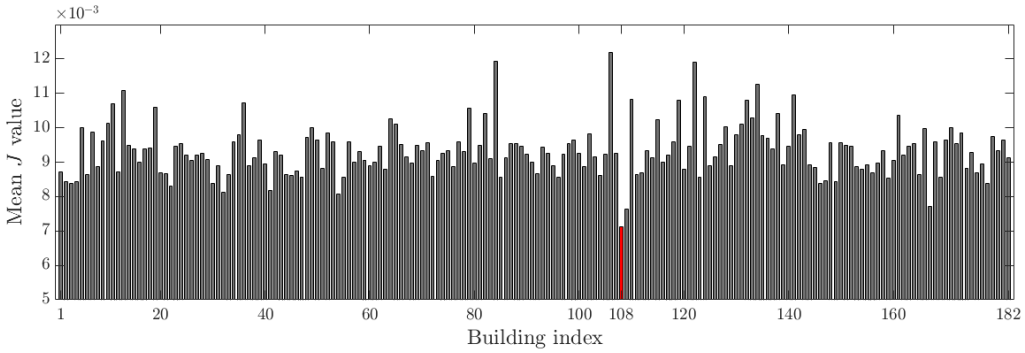

Figure 7: **The average pairwise interaction value for each building**. For the i-th building, we average its interaction with other buildings to obtain $\sum_{j \neq i} J_{ij} / (n-1)$. The average interaction for building #108 is highlighted in red.

4. Conclusions

This study introduces the long-range Ising model as a joint probability distribution of damage states of structures for regional seismic simulations. Using the principle of maximum entropy, the long-range Ising model is derived under the constraints of the first- and second-order cross-moments of the damage states. The Ising model parameters, h and J, are interpreted as a risk field acting at each structure and the pairwise interaction between structures, respectively. Through simple demonstrative examples, the complex interplay between the Ising model parameters and the mean and correlation coefficient of damage states is illustrated. It is found that the mean damage state of a structure is primarily influenced by the risk field acting on it, although the pairwise interactions also play a role in either sharpening or diminishing this effect. Similarly, the correlation coefficient for the damage states between a pair of structures is influenced by all pairwise interactions involving those structures, with the magnitude of the risk field either amplifying or mitigating this effect.

The engineering relevance of the Ising model is further illustrated by two simulation test cases. The first example considers the damage states of buildings in Antakya, Turkey, following the 2023 Turkey-Syria earthquake, and the second example studies neighborhood in Pacific Heights, San Francisco, under synthetic earthquake scenarios generated by the Regional Resilience Determination (R2D) tool of the NHERI SimCenter. In both examples, the Ising model offers insights on the collective behavior of structural failures. Specifically, it is found that the discrepancy between the rankings provided by the individual failure probabilities and the risk field values signifies the impact of collective behavior of failing/not-failing together. Although the examples presented in this study are based on seismic hazards, there is no barrier to extending the proposed framework to other typical hazards.

The Ising model serves as a fundamental component for more advanced statistical mechanics methods to analyze the multi-scale behaviors, phase transitions, and scaling laws in complex multi-body systems. This work establishes a basis for further extensions, suggesting several promising research directions, including the development of Renormalization Group method for modeling and understanding the multi-scale regional behavior under hazards, early-warning systems for system-level phase transitions and criticality, and the Ising models for functionalities of civil infrastructures.

References

[1] Pablo Heresi and Eduardo Miranda. Structure-to-structure damage correlation for scenario-based regional seismic risk assessment. *Structural Safety*, 95:102155, 2022. ISSN 0167-4730. doi: https://doi.org/10.1016/j.strusafe.2021.102155. URL https://www.sciencedirect.com/science/article/pii/S0167473021000783.

[2] Armin Tabandeh, Neetesh Sharma, and Paolo Gardoni. Seismic risk and resilience analysis of networked industrial facilities. *Bulletin of Earthquake Engineering*, pages 1–22, 2023.

[3] Pablo Heresi and Eduardo Miranda. Rpbee: Performance-based earthquake engineering on a regional scale. *Earthquake Spectra*, 39(3):1328–1351, 2023. doi: 10.1177/87552930231179491. URL https://doi.org/10.1177/87552930231179491.

[4] Leo Kadanoff. *Statistical physics: statics, dynamics, and renormalization*. World Scientific, 2000. ISBN 9789810237646.
[5] Shang-Keng Ma. *Modern theory of critical phenomena*. Routledge, 2019. ISBN 9780367095376.
[6] Jack W. Baker and Nirmal Jayaram. Correlation of spectral acceleration values from nga ground motion models. *Earthquake Spectra*, 24(1):299–317, 2008. doi: 10.1193/1.2857544. URL https://doi.org/10.1193/1.2857544.
[7] Frank McKenna, Stevan Gavrilovic, Adam Zsarnoczay, Jinyan Zhao, Kuanshi Zhong, Barbaros Cetiner, Sang-ri Yi, Wael Elhaddad, and Pedro Arduino. NHERI-SimCenter/R2DTool: Version 4.0.0, 1 2024. URL https://doi.org/10.5281/zenodo.10448043.
[8] John W van de Lindt, Jamie Kruse, Daniel T Cox, Paolo Gardoni, Jong Sung Lee, Jamie Padgett, Therese P McAllister, Andre Barbosa, Harvey Cutler, Shannon Van Zandt, Nathanael Rosenheim, Christopher M Navarro, Elaina Sutley, and Sara Hamideh. The interdependent networked community resilience modeling environment (IN-CORE). *Resilient Cities and Structures*, 2(2):57–66, 2023. ISSN 2772-7416. doi: https://doi.org/10.1016/j.rcns.2023.07.004. URL https://www.sciencedirect.com/science/article/pii/S277274162300039X.
[9] Humanitarian Data Exchange (HDX). Turkey Buildings (OpenStreetMap Export). https://data.humdata.org/dataset/hotosm_tur_buildings, . Accessed: 2024-05-13.
[10] Humanitarian Data Exchange (HDX). HOTOSM Turkey Destroyed Buildings (OpenStreetMap Export). https://data.humdata.org/dataset/hotosm_tur_destroyed_buildings, . Accessed: 2024-05-13.
[11] David M. Boore, Jonathan P. Stewart, Emel Seyhan, and Gail M. Atkinson. Nga-west2 equations for predicting pga, pgv, and 5% damped psa for shallow crustal earthquakes. *Earthquake Spectra*, 30(3):1057–1085, 2014. doi: 10.1193/070113EQS184M. URL https://doi.org/10.1193/070113EQS184M.
[12] Maryia Markhvida, Luis Ceferino, and Jack Baker. Effect of ground motion correlation on regional seismic loss estimation: application to Lima, Peru using a cross-correlated principal component analysis model. In *The 12th International Conference on Structural Safety and Reliability*, Vienna, Austria, 8 2017. ISBN 9783903024281.
[13] FEMA. Multi-hazard loss estimation methodology: earthquake model HAZUS-MH 2.1 technical manual. Technical report, Federal Emergency Management Agency, Washington, DC, 2014. URL www.msc.fema.gov.

An adaptive surrogate-based multi-fidelity stratified sampling scheme for probabilistic analysis of nonlinear systems subject to stochastic excitation

Liuyun Xu[1], and Seymour M.J. Spence[1]

[1]*Department of Civil and Environmental Engineering, University of Michigan*

ABSTRACT: Stochastic simulation frameworks generally require a substantial number of model runs when estimating small failure probabilities associated with rare events. In the context of high-fidelity modeling, this can become computationally challenging, especially when dealing with complex nonlinear systems subject to stochastic excitation. To address this, an adaptive surrogate-based multi-fidelity stratified sampling (MFSS) scheme is developed for efficiently propagating uncertainties and estimating probabilities of failure. In this approach, all high-fidelity data used in the stratified multi-fidelity estimator is also employed to train a deep learning-based surrogate model, which then serves as a cost-effective low-fidelity model that correlates well with the high-fidelity model. To derive the optimal trade-off between the approximation quality of the low-fidelity model and the computational demand associated with training, an adaptive training scheme is proposed to seek the minimum training data that ensures an adequate correlation between the high- and low-fidelity models. The efficiency of the proposed scheme for failure probability estimation has been demonstrated through the application to a high-rise steel building subject to stochastic wind excitation.

1 INTRODUCTION

To assess small failure probabilities associated with nonlinear structural systems under general stochastic excitation, the direct Monte Carlo (MC) simulation may yield computationally prohibitive problem in the case of complex high-fidelity models. In response to this limitation, variance reduction techniques, aiming at achieving estimation accuracy with a significantly reduced number of model evaluations, have been widely studied. Among these approaches, stratified sampling has been demonstrated to enable the estimation of small failure probabilities but in general still require several thousand model evaluations to ensure accuracy (Arunachalam & Spence 2023a, 2023b, Xu & Spence 2024). Alternatively, low-fidelity models, such as reduced order models and data-driven surrogate models, have been developed to obtain computational gains (Zhang et al. 2019, Simpson et al. 2021, Li & Spence 2022, Li & Spence 2024). However, low-fidelity models may yield biased or distorted estimators if used directly for complex systems associated with significant nonlinearities (Li et al. 2024). To leverage the accuracy of high-fidelity models and the efficiency of low-fidelity models, multi-fidelity schemes that effectively combine high- and low-fidelity model outputs have emerged (Patsialis & Taflanidis 2021, Li et al. 2024). In general, multi-fidelity schemes can establish an unbiased estimator with substantial variance reduction by shifting most of the work onto the cheap lower-fidelity models but correcting with a few expensive high-fidelity model outputs. Several multi-fidelity approaches employ surrogate models, that provide a rapid data-driven approximation of the high-fidelity output, as the low-fidelity model (Peherstorfer et al. 2016). In the context of estimating small probabilities, a multi-fidelity stratified sampling (MFSS) scheme is proposed in this work. Essentially, a high-fidelity sample set, generated through stratified sampling, serves as training data for not only developing a deep learning-based low-fidelity model but also defining the correction term of the multi-fidelity estimator. Additionally, to further enhance computational efficiency, an adaptive training scheme is introduced that seeks the minimum training data necessary for developing a low-fidelity model that adequately correlates with the high-fidelity model.

2 ADAPTIVE SURROGATE-BASED MULTI-FIDELITY STRATIFIED SAMPLING SCHEME

2.1 *Problem Setting*

Consider a structural system subject to the random input $\boldsymbol{\theta} \in \mathcal{R}^{n_\theta}$, where n_θ is the input dimension. The goal of this work is to develop a multi-fidelity stochastic simulation scheme for estimating the failure probabilities of the system, described by the probability of the response, $y(\boldsymbol{\theta})$, exceeding a threshold, z_i, i.e., $P(y(\boldsymbol{\theta}) > z_i)$. To achieve this, the high-fidelity model that captures the essential inelastic system behavior is assumed to be based on computationally demanding numerical simulations (e.g., finite element models). The deep learning-based surrogate model that approximates the high-fidelity model outputs will serve as the low-fidelity model. For the sake of clarity, the notions *HF* and *LF* will indicate the high- and low-fidelity models in the following. The respective computational costs will be indicated as c_{HF} and c_{LF}.

2.2 *Multi-fidelity Stratified Sampling (MFSS)*

To deal with the small failure probability problem, a generalized stratified sampling (SS) that centers on a potentially efficient intermediate variable related to the system output is considered (Arunachalam & Spence 2023a, 2023b). In this approach, the probability space of interest is partitioned into N_s mutually exclusive and collectively exhaustive subevents, E^k, termed strata. Direct MC can then be used to estimate the exceedance probability curve of the stratification variable and the subsequent unbiased strata probabilities, i.e., $P(E^k) \approx \widehat{N}_{MC}^k / \sum_{k=1}^{N_s} \widehat{N}_{MC}^k$, where $\widehat{N}_{MC}^k$ is the number of strata-wise samples. Of the $\widehat{N}_{MC}^k$ strata-wise samples, N_{HF} random *HF* samples are selected to establish a sample set for training the low-fidelity model as well as estimating the correction term within the multi-fidelity scheme. Therefore, the strata-wise failure probability can be approximated by the multi-fidelity Monte Carlo estimation combining the strata-wise *HF* training data with the *LF* outputs as follows:

$$P(y(\boldsymbol{\theta}) > z_i | E^k) \approx \widehat{H}_{i,MF}^k = \frac{1}{N_{i,HF}} \sum_{j=1}^{N_{i,HF}} h_{i,HF}^k(\boldsymbol{\theta}^j) + a_i^k \left(\frac{1}{N_{i,LF}} \sum_{j=1}^{N_{i,LF}} h_{i,LF}^k(\boldsymbol{\theta}^j) - \frac{1}{N_{i,HF}} \sum_{j=1}^{N_{i,HF}} h_{i,LF}^k(\boldsymbol{\theta}^j) \right) \tag{1}$$

where the subscript, *i*, indicates the term is associated with the i^{th} limit state of interest, z_i; $N_{i,HF}$ and $N_{i,LF}$ are the number of *HF* and *LF* model evaluations in each stratum; $h_{i,HF}^k$ and $h_{i,LF}^k$ are the consequence measures related to the *HF* and *LF* model outputs in the k^{th} stratum; and a_i^k is the control variate of the k^{th} stratum. Computational efficiency can be further improved by optimally determining the control variate as well as the sample allocation from:

$$(a_i^k)^* = \rho \cdot \sqrt{\frac{V[h_{i,HF}^k]}{V[h_{i,LF}^k]}} \tag{2}$$

$$r_i^* = \frac{N_{i,LF}}{N_{i,HF}} = \sqrt{\frac{c_{HF} \cdot \rho^2}{c_{LF} \cdot (1-\rho^2)}} \tag{3}$$

where $V[\cdot]$ is the variance operator; and ρ is approximately estimated as the correlation coefficient between outputs of interest associated with the *HF* and *LF* models. Consequently, the MFSS-based estimation can be mathematically expressed through the total probability theorem as:

$$P(y(\boldsymbol{\theta}) > z_i) \approx \widehat{H}_{i,MF} = \sum_{k=1}^{N_s} \widehat{H}_{i,MF}^k \cdot P(E^k) \tag{4}$$

To achieve the same estimation accuracy/variance, SS relying solely on HF model evaluations requires $N_{i,SS} = N_{i,HF} \times \left(1 - \left(1 - \frac{1}{r_i^*}\right) \cdot \rho^2\right)^{-1}$ samples within each stratum (Patsialis & Taflanidis 2021). Consequently, the speed-up, sp_i, which is the ratio of the computational cost between pure HF-based SS and MFSS estimated with the same variance, can be identified as follows to measure the efficiency of the MFSS scheme.

$$sp_i = \frac{c_{HF}}{c_{HF} + r_i^* \cdot c_{LF}} \left(1 - \left(1 - \frac{1}{r_i^*}\right) \cdot \rho^2\right)^{-1} \tag{5}$$

Note that sp_i is independent of the limit state under consideration in the context of optimal allocation.

2.3 *Adaptive surrogate model development*

The *LF* model is developed by a deep neural network mapping from the input and output spaces using all available *HF* model evaluations generated by SS. Recurrent neural networks (e.g., Long Term Short Memory (LSTM) and Gated Recurrent Unit (GRU)), designed to deal with sequence-to-sequence problems, are adopted to directly create the mapping from the stochastic excitation to system output. To tackle the challenges associated with high-dimensionality (i.e., n_θ in the order of hundreds if not higher in practical engineering problems), a proper orthogonal decomposition (POD)-based model order reduction technique is employed to convert the high-dimensional mapping in the physical space to a significantly lower-dimensional mapping in the reduced space (Li et al. 2021, Li & Spence 2022). Subsequently, the following weighted correlation coefficient in the reduced space is proposed to quantify the correlation between the *HF* and *LF* models for use in the MFSS scheme:

$$\rho_v = \frac{\sum_{l=1}^{n_r} \lambda_l \rho_l}{\sum_{l=1}^{n_r} \lambda_l} \tag{6}$$

where n_r is the number of reduced coordinates that satisfies $\sum_{l=1}^{n_r} \lambda_l^2 / \sum_{l=1}^{n_\theta} \lambda_l^2 \geq \eta$, $\eta \in (0,1]$; λ_l is the j^{th} largest singular value identified from the POD, and ρ_l is the correlation coefficient between outputs of interest from the *HF* and *LF* models in the l^{th} mode. Additionally, to alleviate computational effort and memory demand, it is generally convenient to perform a wavelet transformation of the reduced input and output time sequences, which significantly shortens the sequences to be learned by the deep neural network (Li et al. 2021, Li & Spence 2022).

To derive a trade-off between the approximation quality of the *LF* model and the computational demand, an adaptive training scheme is proposed to seek the minimum training data that ensures an adequate correlation of the *LF* model with minimal variance, as determined through K-fold cross-validation. In this process, all *HF* model evaluations are split into *k* equally sized subsets/folds. During each round, a different fold is set aside for testing, and the remaining *k*-1 folds become the training set. Subsequently, the unbiased model correlation coefficient, $\bar{\rho}_v$, together with its coefficient of variation (COV), δ_v, is assessed by averaging ρ_v and computing the corresponding COV across all rounds. The fundamental idea of the adaptive training strategy involves initially training the model with a small dataset (e.g., N_{init}) and then incrementally adding a fixed number of samples (e.g., N_{add}) from each stratum in each iteration, until reaching a target correlation, $\bar{\rho}_v^*$, and COV, δ_v^*.

3 FRAMEWORK CONFIGURATION

Combining the previous developments, the following workflow was created for the implementation of the adaptive surrogate-based MFSS scheme.

(1) *Initialization*: (a) define the limit states of interest z_i; (b) define the stratified sampling scheme by choosing a stratification variable (in general an intermediate model output), an upper bound of the last stratum P_f^*, and the number of strata N_s; (c) define the adaptive training scheme by choosing the number of *HF* samples in each stratum for initial training, N_{init}, the ratio of computational cost, c_{HF}/c_{LF}, and the target mean correlation, $\bar{\rho}_v^*$, and COV, δ_v^*.

(2) *Generation of intermediate variable samples:* Generation of a large number of MC samples to rapidly construct the unbiased exceedance probability curve of the intermediate variable. Define strata-wise samples by fixing the last stratum with a lower bound exceedance probability of P_f^* and estimate strata probabilities $P(E^k)$ for $k = 1, \dots, N_s$.

(3) *Adaptive surrogate model development*: Choose N_{init} random samples from each stratum to perform the initial training and keep adding N_{add} samples per stratum each iteration until the desired mean correlation, $\bar{\rho}_v^*$, and COV, δ_v^*, is satisfied. Train the surrogate model using $(N_{init} + N_{add}) \times N_s$ samples as the final *LF* model. Therefore, the *HF* dataset includes $N_{i,HF} = N_{init} + N_{add}$ total samples for each stratum.

(4) *Generate strata-wise LF outputs*: Generate $N_{i,LF}$, determined by Eq. (3), *LF* model outputs in each stratum by sampling from the $\widehat{N}_{MC}^k$ strata-wise samples.

(5) *MFSS for failure probability estimation*: Combining $N_{i,HF}$ *HF* and $N_{i,LF}$ *LF* evaluations, estimate the probability of failure and variance reduction ratio.

4 ILLUSTRATIVE EXAMPLE

4.1 *High-fidelity Structural Model and Uncertainties*

To illustrate the efficiency and applicability of the proposed framework, a case study consisting in a two-dimensional (2D) 37-story steel moment-resisting frame subject to stochastic wind excitation is considered, as illustrated in Figure 1. The total height of the structure is 150 m, with a story height of 6 m for the first floor and 4 m for all remaining floors. The structural system comprises box section columns and AISC wide-flange standard beam sections. All the sections are composed of structural steel with Young's modulus E_s= 200 GPa and yield stress σ_y=355 MPa. A fiber-discretized nonlinear model of the 2D frame is established *OpenSees*, which is deemed a *HF* model in this study. Giuffre-Menegotto-Pinto model (i.e., *Steel02* material model in *OpenSees*) is adopted for each fiber of the discretization. Damage resulting from low-cycle fatigue is modeled by warping the *Fatigue* material around each *Steel02* fiber. Large displacement effects are accounted for by utilizing a corotational transformation. To simulate wind load histories, the data-driven spectral proper orthogonal decomposition (POD) model outlined in Chuang & Spence 2019 is adopted. In this model, the record-to-record variability (stochasticity), which serves as input uncertainties, is captured to account for the path-dependency of nonlinear analysis. With a wind speed of 60 m/s and a wind direction of 270°, the stochastic wind loads have a total duration of 10 minutes with an initial ramp-up and a final ramp-down.

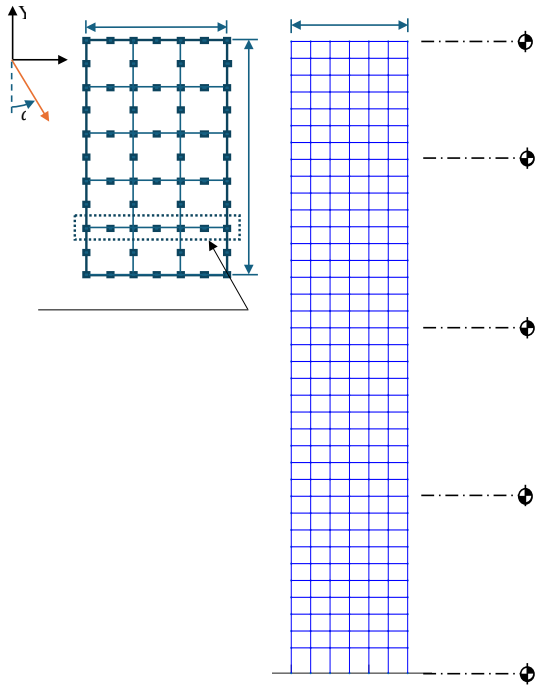

Figure 1. 2D 37-story steel structural system

4.2 *GRU-based Adaptive Surrogate Model*

To derive a trade-off between dimensionality and accuracy, the truncation criterion is set to η= 99.999%. Subsequently, each of the reduced outputs were paired with the corresponding reduced inputs. The wavelet decomposition level is set to four to cover 99% of the energy in the system response. A GRU-based deep

neural network, that maps from the wavelet coefficients of the reduced input sequence to the wavelet coefficients of all reduced outputs, is adopted to develop the *LF* model. Subsequently, the *LF* approximation quality was evaluated by estimating the unbiased correlation in terms of the peak responses in the reduced space through 5-fold cross-validation.

Elastic resultant base moment, M_R, was used as an appropriate intermediate variable for stratification as it is not only computationally negligible to evaluate but also well correlated to the system output. To account for unbiasedness, the probabilistic space of M_R is determined by $\widehat{N}_{MC}$=6,000,000 elastic samples. By fixing the last stratum with an exceedance probability of P_f^*=1×10^{-3}, the probability space was partitioned into N_s=10 strata, imposing an equal squared difference in M_R. To ensure the approximation quality of the *LF* model, the stopping criteria was set to $\bar{\rho}_v^*$=0.95 and δ_v^*=0.03. Subsequently, the adaptive training scheme was initiated from N_{init}=3 in each stratum, and if failed, N_{add}=1 random sample from each stratum was actively added into the next iteration of training until the convergence criteria was satisfied. In this case, 130 samples, as illustrated in Figure 2, are adaptively selected to develop the *LF* model resulting in $\bar{\rho}_v$=0.9640 and δ_v=0.37%. Figure 3 shows the mean and COV values of ρ_v, when increasing training samples, highlighting the significant advantage of using stratified samples over MC samples for satisfying the correlation target.

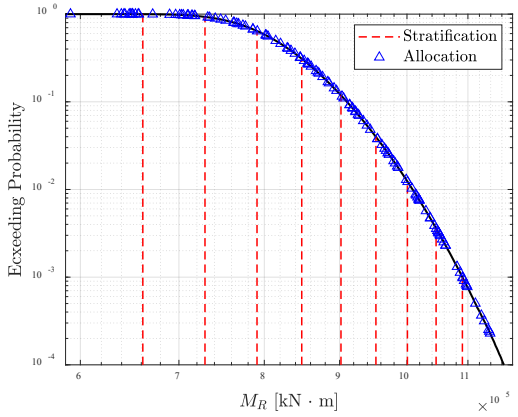

Figure 2. Sample allocation from stratified sampling on M_R

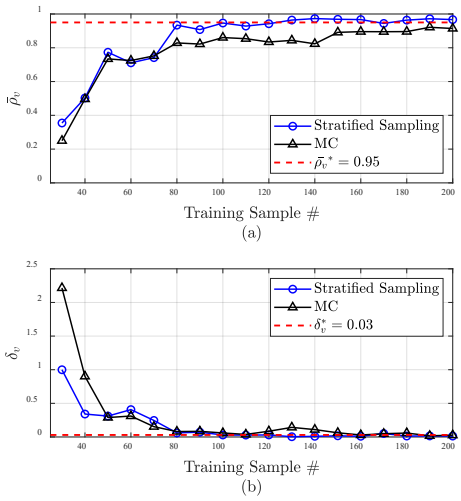

Figure 3. Comparison of (a) mean and (b) COV of ρ_v between stratified sampling and MC

4.3 *Calibration of the MFSS Scheme and Results*

To calibrate the scheme, the computational cost ratio, c_{HF}/c_{LF}, was estimated to be 10,000, showcasing the computational efficiency of neural network over the *HF* model. The MFSS implementation integrated 130 *HF* evaluations together with 47,060 *LF* evaluations, as determined through optimal allocation. To ensure a smooth estimation of the failure probability, the consequence measure $h_i[\cdot]$ is assumed as a standard normal kernel function. To demonstrate the efficiency and accuracy of the proposed scheme, 1770 *HF* simulations generated by SS were utilized as a reference. Figure 4 compares the exceedance probability curves of the peak horizontal top floor displacement, $\hat{u}_X^{(37)}$, evaluated by the different schemes, including stratified sampling using the 130 *HF* model evaluations and the 47,060 GRU-based *LF* predictions, and the proposed MFSS. Compared to pure *HF* stratified sampling, the proposed scheme not only shows remarkable accuracy in reproducing the exceedance probability curve, but also achieves a speed-up of sp_i=13.17. The advantage over the surrogate model (e.g., the GRU-based *LF* model) is also clear from how the MFSS scheme removes the bias of the GRU-based *LF* model. Moreover, Table 1 compares the failure probability

and COV given a limit state of interest between *HF*-based SS and MFSS, which quantitively demonstrates the efficiency of MFSS for small failure probability estimation.

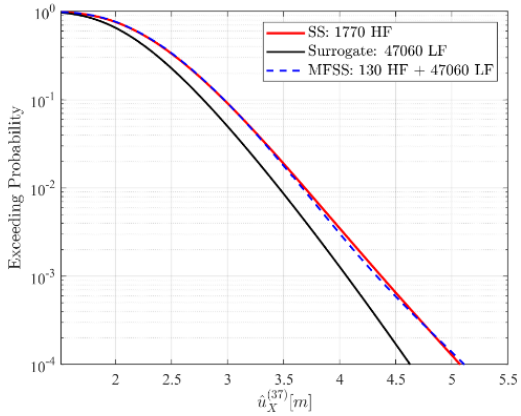

Figure 4. Comparison of the peak top floor displacement in the X-direction in terms of the exceeding probability curves

Table 1. Comparison of failure probabilities and COV between SS and MFSS

LS	SS (1770 *HF*)		MFSS (130 *HF* +47060 *LF*)	
	$\hat{H}_{i,SS}$	COV	$\hat{H}_{i,MF}$	COV
$\hat{u}_X^{(37)}$>5m	1.27×10^{-4}	0.2736	1.37×10^{-4}	0.2817

5 SUMMARY

This paper developed an adaptive surrogate based multi-fidelity stratified sampling (MFSS) scheme for efficient estimation of small failure probabilities associated with nonlinear structural systems subject to stochastic excitation. In the scheme, a deep learning-based *LF* model is developed by training on all *HF* evaluations obtained from stratified sampling on an intermediate variable. Additionally, these *HF* model evaluations also serve to estimate the correction term within the MFSS scheme. To find an optimal balance between approximation quality and computational demand during training, the minimum training data that ensures an adequate unbiased correlation between the high- and low-fidelity models with target variance, is obtained by an adaptive training strategy. The proposed scheme is shown to have remarkable efficiency in reproducing the exceedance probability curves of nonlinear structural responses with significant computational gains. The potential of the scheme in the probabilistic analysis of nonlinear structural systems is showcased.

REFERENCES

Arunachalam, S., & Spence, S. M. J. 2023a. An efficient stratified sampling scheme for the simultaneous estimation of small failure probabilities in wind engineering applications. *Structural Safety*, 101, 102310.

Arunachalam, S., & Spence, S. M. J. 2023b. Generalized stratified sampling for efficient reliability assessment of structures against natural hazards. *Journal of engineering mechanics*, 149(7), 04023042.

Chuang, W. C., & Spence, S. M. J. 2019. An efficient framework for the inelastic performance assessment of structural systems subject to stochastic wind loads. *Engineering Structures*, 179, 92-105.

Li, B., Chuang, W. C., & Spence, S. M. J. 2021. Response estimation of multi-degree-of-freedom nonlinear stochastic structural systems through metamodeling. *Journal of Engineering Mechanics*, 147(11), 04021082.

Li, B., & Spence, S. M. J. 2022. Metamodeling through deep learning of high-dimensional dynamic nonlinear systems driven by general stochastic excitation. *Journal of Structural Engineering*, 148(11), 04022186.

Li, B., & Spence, S. M. J. 2024. Deep learning enabled rapid nonlinear time history wind performance assessment. *Structures*, 66, 106810.

Li, M., Arunachalam, S., & Spence, S. M. J. 2024. A multi-fidelity stochastic simulation scheme for estimation of small failure probabilities. *Structural Safety*, 106, 102397.

Patsialis, D., & Taflanidis, A. A. 2021. Multi-fidelity Monte Carlo for seismic risk assessment applications. Structural Safety, 93, 102129.

Peherstorfer, B., Willcox, K., & Gunzburger, M. (2016). Optimal model management for multifidelity Monte Carlo estimation. *SIAM Journal on Scientific Computing*, 38(5), A3163-A3194.

Simpson, T., Dervilis, N., & Chatzi, E. (2021). Machine learning approach to model order reduction of nonlinear systems via autoencoder and LSTM networks. *Journal of Engineering Mechanics*, 147(10), 04021061.

Xu, L., & Spence, S. M. J. (2024). Collapse reliability of wind-excited reinforced concrete structures by stratified sampling and nonlinear dynamic analysis. *Reliability Engineering & System Safety*, 110244.

Zhang, R., Chen, Z., Chen, S., Zheng, J., Büyüköztürk, O., & Sun, H. (2019). Deep long short-term memory networks for nonlinear structural seismic response prediction. *Computers & Structures*, 220, 55-68.

A physics and data co-driven surrogate modeling method for high-dimensional forward and inverse uncertainty quantification

Jianhua Xian, Ziqi Wang*

Department of Civil and Environmental Engineering, University of California, Berkeley, USA

Abstract: A physics and data co-driven surrogate modeling method is presented for efficient rare event simulation and Bayesian model updating of civil and mechanical systems with high-dimensional input uncertainties. The method fuses interpretable low-fidelity physical models with data-driven error corrections. The hypothesis is that a well-designed and well-trained simplified physical model can preserve salient features of the original model, while data-fitting techniques can fill the remaining gaps between the surrogate and original model predictions. The coupled physics-data-driven surrogate model is adaptively trained using active learning, aiming to achieve a high correlation and small bias between the surrogate and original model responses in the critical parametric regions of rare events and model updates. A final importance sampling step is introduced to correct the surrogate model-based probability and normalizing constant estimations.

Keywords: surrogate modeling, active learning, importance sampling, high-dimensional, rare event simulation, Bayesian model updating

1. Introduction

Uncertainty quantification (UQ) seeks to quantify and understand the effects of pervasive uncertainties that arise in science and engineering. Forward UQ focuses on propagating the uncertainties from input parameters to predict their impact on the outputs, while inverse UQ aims to infer the uncertain input parameters based on the observed output data. The Gaussian process-based surrogate modeling methods have been proven to be effective in various UQ applications, e.g., rare event simulation [1]-[3] and Bayesian model updating [4]-[6]. However, the surrogate model training will become increasingly challenging and ultimately infeasible with a growing number of input parameters–a phenomenon known as the curse of dimensionality. The possible way out is to incorporate the domain/problem-specific prior knowledge into the surrogate modeling process, as evidenced by the emerging paradigms of scientific machine learning [7] and physics-based surrogate modeling [8]-[9]. Building on the latter, a physics-based and data-driven surrogate modeling method has been recently proposed for high-dimensional rare event simulation of civil engineering applications [10]. In this work, we further extend this method to address high-dimensional Bayesian model updating, demonstrating its potential for solving both forward and inverse UQ problems.

2. Methodology

We leverage physics-based surrogate modeling to solve high-dimensional rare event estimation and Bayesian model updating problems. A physics-based surrogate model can be adapted from the original high-fidelity model in various ad hoc ways, such as domain-specific simplifications and relaxations of numerical solvers. Physics-based surrogate models may have inherent errors due to simplifications, and thus it is promising to introduce a data-driven error correction to fill the gap between the surrogate and original model predictions. However, such an error correction is inherently noisy since the mapping from the surrogate model response to the original model response can be

one-to-many. The noisy level of error correction is inversely related to the correlation between the surrogate model response and the original model response. Therefore, a physical model optimization is desirable to maximize this correlation, such that the noise of error correction is acceptable and can be well captured by certain data-fitting techniques. We use the heteroscedastic Gaussian process to fit the noisy error correction since it can handle the input-dependent noise. Active learning is required for effective training, especially when the rare event probability is small and the measurement itself is a rare event. The goal of active learning is to identify training points over certain critical regions. For rare event simulation, this critical region should be around the boundary of the rare event; while for Bayesian model updating, the critical region should be around the measurement. Due to the presence of inherent noises, there is no guarantee that the probability/normalizing constant prediction from the surrogate model will converge to the true value. To address this issue, we apply a final step of importance sampling to improve the surrogate model solutions, by coupling surrogate model simulations with limited evaluations of the original model. Figure 1 presents a schematic of the proposed surrogate modeling method for rare event simulation and Bayesian model updating.

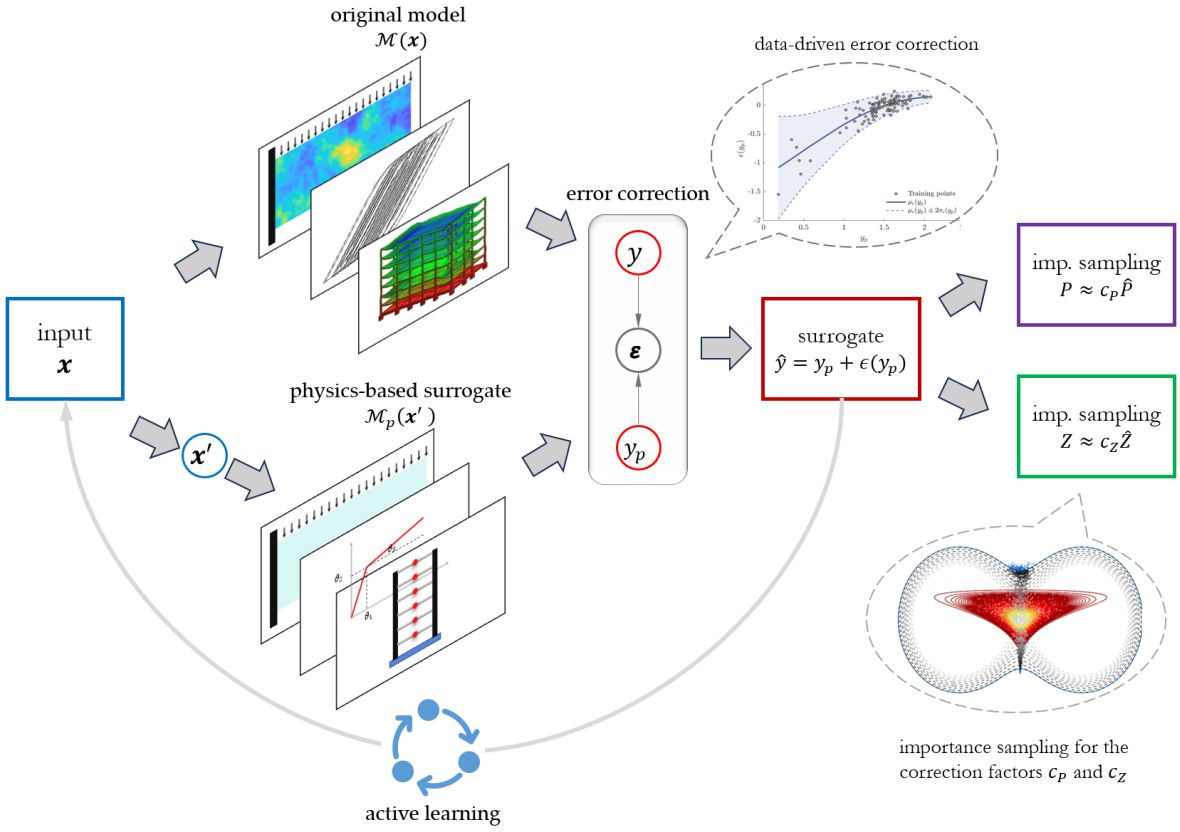

Figure 1. ***Schematic of the proposed surrogate modeling method for rare event simulation and Bayesian model updating****. The physics-based surrogate model* $y_p = \mathcal{M}_p(\boldsymbol{x}'; \boldsymbol{\theta}_p)$ *contains tunable control parameters* $\boldsymbol{\theta}_p$ *to be optimized in the training process. The error correction function* $\epsilon(y_p)$ *is modeled in the space of* y_p *by heteroscedastic Gaussian process to account for input-dependent noises. The active learning adaptively enriches the training set with a learning criterion to emphasize contributions from the critical regions of rare event and model update. The importance sampling estimates the correction factors* c_P *and* c_Z *to further improve the probability and normalizing constant estimations of the surrogate model.*

References

[1] Echard B, Gayton N, Lemaire M. AK-MCS: an active learning reliability method combining Kriging and Monte Carlo simulation. *Structural safety*, 2011, 33(2): 145-154.

[2] Echard B, Gayton N, Lemaire M, Relun N. A combined importance sampling and kriging reliability method for small failure probabilities with time-demanding numerical models. *Reliability Engineering & System Safety*, 2013, 111: 232-240.

[3] Huang X, Chen J, Zhu H. Assessing small failure probabilities by AK-SS: An active learning method combining Kriging and Subset Simulation. *Structural Safety*, 2016, 59: 86-95.

[4] Wang ZY, Shafieezadeh A. Highly efficient Bayesian updating using metamodels: An adaptive Kriging-based approach. *Structural Safety*, 2020, 84: 101915.

[5] Yoshida I, Nakamura T, Au SK. Bayesian updating of model parameters using adaptive Gaussian process regression and particle filter. *Structural Safety*, 2023, 102: 102328.

[6] Jiang X, Lu ZZ. Adaptive Kriging-based Bayesian updating of model and reliability. *Structural Safety*, 2023, 104: 102362.

[7] Raissi M, Perdikaris P, Karniadakis GE. Physics-informed neural networks: A deep learning framework for solving forward and inverse problems involving nonlinear partial differential equations. *Journal of Computational Physics*, 2019, 378: 686-707.

[8] Peherstorfer B, Willcox K, Gunzburger M. Survey of multifidelity methods in uncertainty propagation, inference, and optimization. *SIAM Review*, 2018, 60(3): 550-591.

[9] Wang ZQ. Optimized equivalent linearization for random vibration. *Structural Safety*, 2024, 106: 102402.

[10] Xian JH, Wang ZQ. A physics and data co-driven surrogate modeling method for high-dimensional rare event simulation. *Journal of Computational Physics*, 2024, 510: 113069.

Extracting a Stochastic Surrogate Model from Feature Space for Seismic Response of Bridges

Jungho Kim, Sang-ri Yi, and Ziqi Wang

Department of Civil and Environmental Engineering,
University of California Berkeley, CA, USA

Abstract: This paper introduces a stochastic surrogate modeling approach designed to enhance seismic uncertainty quantification for bridge responses. The method addresses the challenges posed by high-dimensional seismic input uncertainties by integrating input-output dimensionality reduction with feature space conditional distribution techniques. The proposed approach extracts a stochastic surrogate model from the low-dimensional representation of the input-output space, enabling efficient prediction of multivariate seismic responses while propagating both aleatory and epistemic uncertainties. Application to bridge seismic responses validates the performance of the method in significantly reducing computational cost without compromising accuracy.

Keywords: Dimensionality reduction, seismic risk, surrogate modeling, uncertainty quantification

1 INTRODUCTION

Uncertainty quantification (UQ) in seismic response analysis plays a pivotal role in performance-based earthquake engineering (PBEE). Forward UQ evaluates the impact of input uncertainties on structural responses, focusing on how these uncertainties propagate through computational models. As seismic analyses grow increasingly complex, particularly in the context of nonlinear response history analysis (NLRHA), the computational demands become prohibitive, especially when addressing high-dimensional input uncertainties (Gidaris et al., 2015; Kim et al., 2023). While traditional Monte Carlo simulation (MCS) is a benchmark method for UQ, it is hindered by slow convergence, which makes it impractical for large-scale applications.

To mitigate these challenges, surrogate modeling provides a promising solution by replacing computationally intensive models with efficient surrogates. However, methods such as Kriging and polynomial chaos expansion often struggle with the curse of dimensionality, especially in the context of seismic UQ (Williams & Rasmussen 2006; Blatman & Sudret 2011; Kim & Song 2021). This paper introduces a novel framework that extracts a stochastic surrogate model from the low-dimensional feature space of the input-output relationship. A preliminary version of this work has been presented by Kim et al. (2024b) and Kim & Wang (2024).

2 CHALLENGES IN HIGH-DIMENSIONAL SURROGATE MODELING

High-dimensional input spaces significantly complicate the construction of surrogate models, especially in seismic UQ. Dimensionality reduction techniques, such as principal component analysis (PCA), kernel-PCA, and active subspace, are commonly used to reduce the complexity of these input spaces (Abdi & Williams 2010; Kontolati et al., 2022; Kim et al., 2024a). In seismic analysis, the inherent complexity of ground motion characteristics poses an additional layer of difficulty. To address this, the proposed method integrates input-output dimensionality reduction with a feature space conditional distribution model, enabling the extraction of a stochastic surrogate model from the reduced feature space. This approach effectively manages high-dimensional uncertainties, which are critical for accurate seismic response analysis.

3 METHODOLOGY: DIMENSIONALITY REDUCTION-BASED STOCHASTIC SURROGATE MODELING

The proposed methodology begins with a high-dimensional input vector $\boldsymbol{X} \in \mathbb{R}^n$ and an output vector $\boldsymbol{Y} \in \mathbb{R}^m$, representing structural responses. Dimensionality reduction maps the input-output space into a low-dimensional feature space $\boldsymbol{\Psi_z} \in \mathbb{R}^d$, where $d \ll n + m$. The dimensionality reduction is described by the mapping $\mathcal{H}: \mathbb{R}^{n+m} \mapsto \mathbb{R}^d$, which preserves the essential features of the original relationship between $\boldsymbol{X}$ and $\boldsymbol{Y}$ while reducing the computational complexity. This study employs a physics-based dimensionality reduction method specifically tailored for seismic response (Kim & Wang, 2024).

Once the dimensionality reduction is obtained, a feature space conditional distribution model $f_{\widehat{\boldsymbol{Y}}|\boldsymbol{\Psi_z}}$ is constructed to predict $\boldsymbol{y}$ given $\boldsymbol{\psi}_z$. A kernel density estimation model is employed for this purpose (Kristan et al., 2011). In the final step, a stochastic surrogate model, denoted as $f_{\widehat{\boldsymbol{Y}}|\boldsymbol{X}}(\widehat{\boldsymbol{y}}|\boldsymbol{x})$, is extracted from the results of the dimensionality reduction and the conditional distribution model. A random variable governed by the conditional law of $\widehat{\boldsymbol{Y}}$ given $\boldsymbol{X}$ is introduced to iteratively approximate the model. This iterative process continues until convergence to a stationary model that satisfies a fixed-point equation, which is interpreted as a stationary distribution for a Markov process with a transition kernel incorporating both the conditional distribution and dimensionality reduction.

Given $\boldsymbol{X} = \boldsymbol{x}$, the transition kernel is formulated as:

$$T\left(\widehat{\boldsymbol{y}}^{(t)}, \widehat{\boldsymbol{y}}^{(t+1)}|\boldsymbol{x}\right) = f_{\widehat{\boldsymbol{Y}}|\boldsymbol{\Psi_z}}\left(\widehat{\boldsymbol{y}}^{(t+1)}\middle|\boldsymbol{\psi}_z\right) f_{\boldsymbol{\Psi_z}|\boldsymbol{XY}}\left(\boldsymbol{\psi}_z\middle|\boldsymbol{x}, \widehat{\boldsymbol{y}}^{(t)}\right), \tag{1}$$

where $f_{\boldsymbol{\Psi_z}|\boldsymbol{XY}}$ is the dimensionality reduction by the mapping $\mathcal{H}$. The iterative generation of $\widehat{\boldsymbol{y}}^{(t)}$, for $t = 1, \ldots, N_t$, forms a stochastic surrogate model that facilitates the prediction of $\boldsymbol{y}$ given $\boldsymbol{x}$. In summary, the samples generated by the transition kernel are used to estimate the mean vector $\mu_{\widehat{\boldsymbol{Y}}}(\boldsymbol{x})$ and the covariance matrix $\Sigma^2_{\widehat{\boldsymbol{Y}}\widehat{\boldsymbol{Y}}}(\boldsymbol{x})$, providing a comprehensive uncertainty quantification of the outputs.

4 NUMERICAL INVESTIGATION

The performance of the proposed method is evaluated using a finite element model of the Auburn Ravine Bridge (Konakli & Kiureghian, 2011). The bridge, a prestressed concrete structure with six spans and two piers per bent, is modeled to account for nonlinear behavior. A point-source stochastic ground motion model is used to generate synthetic ground motions applied longitudinally to the bridge. The geometric properties of the bridge are illustrated in Figure 1. The input vector $\boldsymbol{X}$ includes seismic hazard parameters (magnitude and rupture distance), structural parameters (damping ratio, material properties of reinforcing steel and concrete), and high-dimensional stochastic excitation sequences (white noise process). The total input dimensionality is $n = 2{,}061$, and the seismic responses, measured as pier drift ratios (PDRs), form the output vector $\boldsymbol{Y} \in \mathbb{R}^{10}$.

A dataset of 600 input-output pairs, generated via Latin Hypercube sampling, is used to train the surrogate model. Reference results are obtained from 20,000 NLRHAs conducted through MCS for validation purposes. Figure 2 presents the surrogate modeling results for the PDRs of the first and fourth piers, with relative mean squared errors (RMSEs) of 0.1449 and 0.1420, respectively. These results demonstrate the effectiveness of the proposed stochastic surrogate model in capturing the variability of the seismic bridge response, with the majority of observed data points falling within the predicted standard deviation intervals. Figure 3 presents box plots for a total of 10 PDRs, which further validate the surrogate model's performance in reliably predicting multivariate seismic responses.

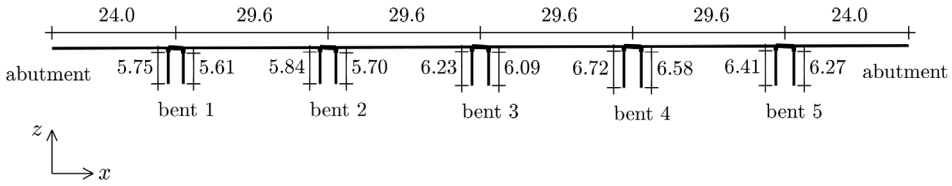

Figure 1 Elevation of the Auburn Ravine Bridge (unit: m).

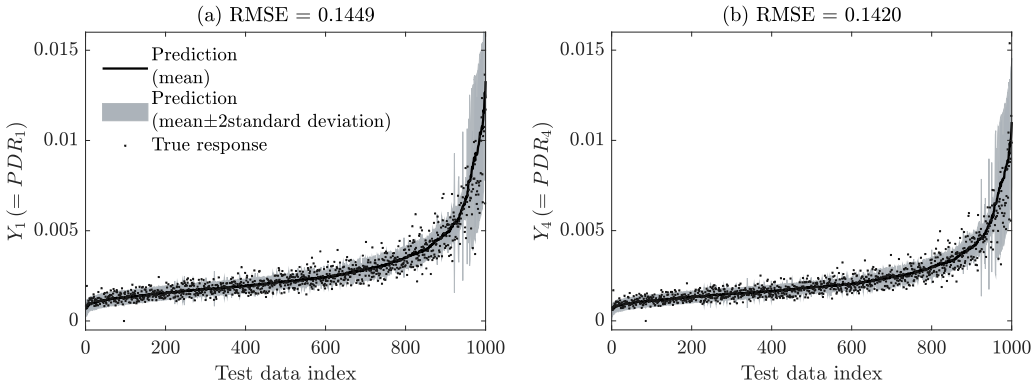

Figure 2 Stochastic surrogate modeling of bridge responses: (a) PDR_1 and (b) PDR_4.

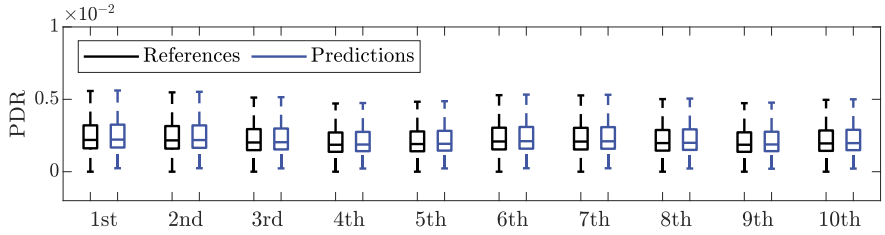

Figure 3 **Box plot of bridge PDRs.**

5 CONCLUSIONS

This study proposes a stochastic surrogate modeling approach for seismic UQ, specifically designed to efficiently handle high-dimensional input spaces. The primary contributions of this work include: (1) the development of a stochastic surrogate model extracted through dimensionality reduction, (2) probabilistic output predictions that quantify prediction variability, and (3) multi-output predictions across various structural response locations. Numerical results for a bridge structure demonstrate the method's capability to significantly reduce computational costs while maintaining high prediction accuracy. These findings confirm the effectiveness of the surrogate model for seismic UQ, offering a promising foundation for further development in tackling even more complex, high-dimensional engineering problems.

ACKNOWLEDGEMENTS

This research was supported by the Pacific Earthquake Engineering Research Center grant NCTRZW. This research was also supported by the Basic Science Research Program through the National Research Foundation of Korea (NRF) funded by the Ministry of Education (RS-2024-00407901).

REFERENCES

Abdi H., Williams L. J. (2010). Principal component analysis, Wiley Interdiscip. Rev.-Comput. Stat., 2(4):433-459. doi: 10.1002/wics.101.

Blatman G., Sudret B. (2011). Adaptive sparse polynomial chaos expansion based on least angle regression. J. Comput. Phys., 230(6), 2345-2367. doi: 10.1016/j.jcp.2010.12.021.

Gidaris I., Taflanidis A. A., Mavroeidis G. P. (2015). Kriging metamodeling in seismic risk assessment based on stochastic ground motion models, Earthq. Eng. Struct. Dyn., 44(14): 2377-2399, doi: 10.1002/eqe.2586.

Kim J., Song J. (2021). Quantile surrogates and sensitivity by adaptive Gaussian process for efficient reliability-based design optimization, Mech. Syst. Signal Proc., 161: 107962, doi: 10.1016/j.ymssp.2021.107962.

Kim J., Yi S., Song J. (2023). Estimation of first-passage probability under stochastic wind excitations by active-learning-based heteroscedastic Gaussian process, Struct. Saf., 100:102268, doi: 10.1016/j.strusafe.2022.102268.

Kim J., Wang Z., Song J. (2024a). Adaptive active subspace-based metamodeling for high-dimensional reliability analysis, Struct. Saf., 106:102404, doi: 10.1016/j.strusafe.2023.102404.

Kim J., Yi S., Wang Z. (2024b). Dimensionality reduction can be used as a surrogate model for high-dimensional forward uncertainty quantification, arXiv preprint, arXiv:2402.04582, doi: 10.48550/arXiv.2402.04582.

Kim J., Wang Z. (2024) Uncertainty quantification for seismic response using dimensionality reduction-based stochastic simulator. arXiv preprint, arXiv:2409.17159, doi: 10.48550/arXiv.2409.17159.

Kristan, M., Leonardis, A., Skočaj, D. (2011). Multivariate online kernel density estimation with Gaussian kernels. Pattern Recognit., 44(10-11): 2630-2642, doi: 10.1016/j.patcog.2011.03.019.

Konakli K., Kiureghian A. D. (2011). Extended MSRS rule for seismic analysis of bridges subjected to differential support motions, Earthq. Eng. Struct. Dyn., 40(12): 1315-1335, doi: 10.1002/eqe.1090.

Kontolati K., Loukrezis D., Giovanis D. G., Vandanapu L., Shields M. D. (2022). A survey of unsupervised learning methods for high-dimensional uncertainty quantification in black-box-type problems. J. Comput. Phys., 464: 111313. doi: 10.1016/j.jcp.2022.111313.

Williams C. K., Rasmussen C. E. (2006). Gaussian processes for machine learning. Vol. 2. No. 3. Cambridge, MA: MIT press.

Upgrading the structural performance assessment of PC box girder bridges through FE model updates

Debao Chen [1] and Chul-Woo Kim [2]

[1] Ph.D. Candidates, Department of Civil and Earth Resources Engineering, Graduate School of Engineering, Kyoto University, Kyoto 615-8540, JAPAN
Email: chen.debao.66u@st.kyoto-u.ac.jp

[2] Professor, corresponding author, Department of Civil and Earth Resources Engineering, Graduate School of Engineering, Kyoto University, Kyoto 615-8540, JAPAN
Email: kim.chulwoo.5u@kyoto-u.ac.jp

Abstract

This study is aimed at integrating existing measured data with a high-fidelity finite element (FE) model, thereby achieving a physics-based digital twin for PC box girder bridges by employing a Bayesian model updating framework. Transitional Markov Chain Monte Carlo (TMCMC) sampling served as the computational approach for estimating the posterior probability density functions (PDFs) of model parameters. The selection of a plausible model class was informed by the estimated model evidence. After the implementation of the updating framework, nonlinear static simulation results obtained through the calibrated model were found to be consistent with both the observed crack pattern and the load-deflection curve. Subsequently, a simulation method to account for tendon rupture was incorporated into the calibrated FE model. Observations demonstrated that although the model responses derived from vibration-based model updating closely matched the measured data, questions arose about the physical significance of material parameters that exhibited notable deviations from the reference values. However, the incorporation of static-dynamic data in the model updating process led to accurate estimates of material parameters. Moreover, the simulated responses from the calibrated model demonstrated good agreement with the measured data. To ensure reliability of the calibrated model, cross-verifying it with multi-source data is extremely important, especially when both static and dynamic response data are available.

Keywords: *Bayesian model updating, Physics-based digital twin, PC box girder, Structural performance evaluation, Tendon rupture.*

1. Introduction

Bayesian model updating serves as a powerful tool to minimize discrepancies between

observed and predicted structural responses, thereby improving the model's predictive accuracy. It enables more accurate parameter estimation by considering uncertainty and updating a structure's current state when new data becomes available. Bayesian methodologies, which integrate data fusion techniques for damage assessment, are gaining widespread adoption in the field of structural health monitoring (SHM). These methods excel in addressing uncertainties, synthesizing diverse data sources, improving the identifiability of inverse problems, and enhancing the reliability of structural assessments. For instance, Ierimonti et al. [1] introduced a Bayesian-based data fusion framework designed to detect and localize structural damages in historical monuments following seismic events. This method leveraged monitoring data and visual inspections while employing FE and surrogate models. Zhou et al. [2] implemented a vibration-based Bayesian model updating approach on a real-world steel truss bridge, demonstrating its effectiveness in detecting damage in truss members and showcasing its practical applicability. Integrating Bayesian model updating to develop high-fidelity models is a crucial element in the construction of physics-based digital twins. A digital twin serves as a virtual counterpart to a physical object, designed to replicate its behavior and characteristics with high accuracy. The concept of digital twins is continually advancing, integrating capabilities such as visualization, simulation, real-time prediction, and the fusion of diverse data sources [3]. While current technologies enable the creation of 3D digital replicas of physical assets, challenges persist in establishing a real-time connection between the physical and digital twins and ensuring effective data integration. Unlike traditional digital models or replicas, digital twins are uniquely characterized by their dynamic, continuous interaction with corresponding physical systems over time [4]. Bayesian model updating is a robust approach for incorporating data from the physical twin into the digital model. Within the digital twin framework, where 3D visualization plays a pivotal role, there is an increased need for complex and detailed models. In particular, the initial model used for updating is expected to accurately and comprehensively represent the geometric features of the structure. For complex structures like prestressed concrete (PC) bridges, simplified beam models are insufficient for accurately capturing their structural behaviors, particularly nonlinear mechanical responses. As a result, utilizing 3D solid models for Bayesian model updating offers a promising approach to improving the accuracy of PC bridge analyses. Additionally, it is essential to adopt a more comprehensive and long-term perspective on the PC bridge's life cycle and deterioration. Bayesian model updating should be applied to align the structural response of the digital model with the measured data in the healthy state of a PC bridge. This model can then serve as a baseline for conducting "what-if" scenario simulations, which could provide valuable insights to inform maintenance decisions. Driven by the gap between engineering needs and current research, this study aims to develop a tailored digital twin framework for PC girder bridges. The framework combines Bayesian model selection and

updating techniques, a high-fidelity three-dimensional (3D) FE model with nonlinear material laws, and a simulation approach for prestressed tendon damage, all designed to support the maintenance of PC girder bridges. This study aims to enhance the efficiency and accuracy of structural performance evaluations for PC bridges by combining monitoring data with a high-fidelity Fourier neural operator (FNO)-based surrogate model and a Transitional Markov Chain Monte Carlo (TMCMC) sampler. This integration creates a physics-based digital twin that effectively captures both the linear and nonlinear behaviors of PC girder bridges.

2. Methodology

The theoretical foundation of Bayesian model updating is Bayes' theorem, which is utilized to infer the posterior probability density function (PDF) of the parameters of interest given a set of independent observations.

In this study, Fourier neural operator (FNO), as proposed by Li et al. [5], is employed to approximate the solutions to the equation of motion and the bending differential equation.

The free-vibration equation of motion for a straight beam with uniform mass distribution and constant stiffness is given by:

$$EI\frac{\partial^4 v(x,t)}{\partial x^4} + \bar{m}\frac{\partial^2 v(x,t)}{\partial t^2} = 0 \tag{1}$$

where $\bar{m}$ denotes the mass per unit length of the beam, and $v(x,t)$ denotes the transverse displacement of the beam as a function of position x (along the beam length) and time t.

The governing partial differential equation (PDE) for the Euler-Bernoulli beam is expressed as:

$$\frac{\partial^2}{\partial x^2}\left(EI\frac{\partial^2 v}{\partial x^2}\right) = q(x) \tag{2}$$

where $v(x)$ is the transverse displacement (deflection) of the beam, EI is the bending stiffness of the beam cross-section, and $q(x)$ is the distributed load along the beam's length.

The Markov Chain Monte Carlo (MCMC) method is extensively employed to estimate the posterior distributions of model parameters. Transitional Markov Chain Monte Carlo (TMCMC) extends this approach by generating a series of intermediate PDFs that transition from the prior PDF to the posterior PDF [6]. The transitional distributions are defined as:

$$P^j \propto P(\boldsymbol{D}|\boldsymbol{\theta})^{\beta_j} \cdot P(\boldsymbol{\theta}) \tag{3}$$

where j denotes the transition step number, and β_j is the tempering parameter, satisfying $\beta_0 = 0 < \beta_1 < \beta_2 < \cdots < \beta_m = 1$. Notably, $P^0 = P(\boldsymbol{\theta})$ represents the prior distribution, while $P^m = P(\boldsymbol{\theta}|\boldsymbol{D})$ denotes the posterior distribution.

Figure 1 illustrates the proposed FNO-aided Bayesian model selection and updating framework. First, an FNO-based surrogate model is trained using data pairs generated from FE

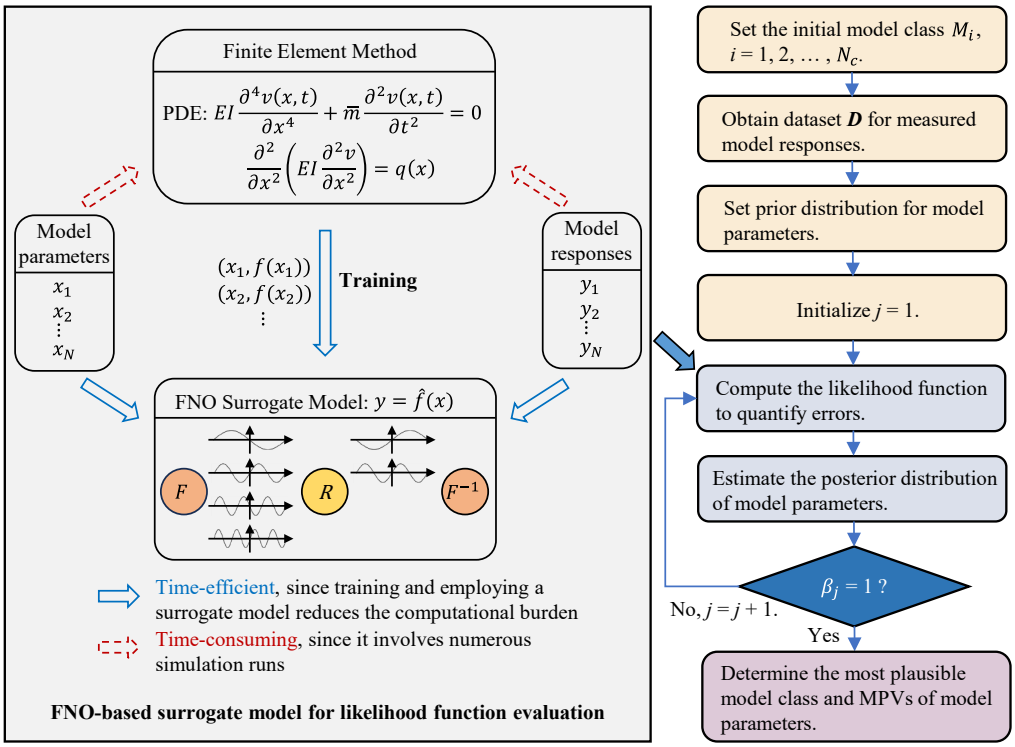

Figure 1. FNO-aided Bayesian model selection and updating framework.

simulations to approximate the relationship between predefined inputs and outputs, thereby estimating the solution to the governing PDEs [7]. The input data in FNO is transformed into the frequency domain through the Fast Fourier Transform (FFT), and the resulting coefficients are then fed into a convolutional neural network (CNN). The CNN is trained to learn the mapping between the input coefficients and the output coefficients, enabling it to efficiently approximate the solution to the PDEs at new input points. Second, the Bayesian model selection and model updating process is conducted, which involves: (1) defining candidate model classes, (2) estimating parameters for each model class, and (3) identifying the most plausible model class and calibrating its model parameters based on the most probable values (MPVs).

3. Case Study

3.1. Experiment and finite element model

A case study was conducted based on the PC box girder experiments shown in Figure 2 [8]. The test specimen prototype is a post-tensioned PC box girder bridge, designed according to Japanese Specifications for Highway Bridges. As illustrated in Figure 2, the specimen represents a 1/2 scale simply supported box girder with a span length of 7.5 m and a girder height of 1000

mm. The specimens were subjected to a four-point concentrated static load. Vibration tests were conducted to evaluate vibration characteristics simultaneously. The deflection diagram presenting measurements under a 446 kN load is shown in Figure 3(a). At this load level, the PC box girder remains within its elastic stress range. Modal properties were extracted from the frequency response function (FRF) using acceleration data, as shown in Figure 3(b), (c), and (d). The legend labels "Left side" and "Right side" denote the bending modes identified based on acceleration data from the left and right webs, respectively, while "Avg." represents the bending mode averaged and normalized across both sides.

A 3D FE model was developed using DIANA 10.6 as the initial model for updating, as shown in Figure 4. The concrete beam was modeled using 8-node hexahedral solid elements, while rebar and prestressing tendons were represented by embedded line elements within the concrete elements. In order to better simulate actual boundary conditions in the experiment, springs were incorporated at the supports to provide both rotational and translational stiffness.

The error function representing the discrepancy between measurements and model predictions in model updating is assumed to follow a zero-mean normal distribution. Furthermore, it is assumed that the errors associated with individual measurements, D_k, are identically distributed with an equal variance σ^2. Under these assumptions, the error function can be expressed as:

$$P(\boldsymbol{D}|\boldsymbol{\theta}) = \left(\frac{1}{\sigma \cdot \sqrt{2\pi}}\right)^n \cdot exp\left[-\frac{J_g(\boldsymbol{\theta})}{2\sigma^2}\right] \quad (4)$$

where $J_g(\boldsymbol{\theta})$ is defined as the goodness-of-fit function.

Based on the results of the sensitivity analysis, the uncertain parameters chosen for model updating include the elastic modulus of concrete (E_c), mass density of concrete (ρ_c), spring constant of rotational spring (K_r) and spring constant of translational spring (K_t). This study examines three model classes: M_1, which involves four parameters (E_c, ρ_c, K_r, K_t); M_2, which involves three parameters (E_c, ρ_c, K_r); and M_3, which involves two parameters (E_c, ρ_c). Different updating scenarios are discussed, considering various model classes and multi-source data for Bayesian model updating. The scenarios are denoted by the label "Scen. (k)_R(m)_T(n)", where "(k)" represents the model class (1, 2, or 3), "(m)" indicates the inclusion (0 or 1) of the rotational spring, and "(n)" indicates the inclusion (0 or 1) of the translational spring. The terms "Scen.", "R", and "T" stand for "Scenario", "Rotational Spring", and "Translational Spring", respectively. The model responses used in the updating process are grouped into three categories: "Scen. 1" integrates the frequencies and mode shapes of the first and second modes (see Figure 3(b) and (c)) into the goodness-of-fit function; "Scen. 2" incorporates the frequencies and mode shapes of the first and third modes (see Figure 3(b) and (d)); and "Scen. 3" includes the elastic deflection, along with the frequency and mode shape of the first vertical bending mode (see Figure 3(a) and (b)). The Modal Assurance Criterion

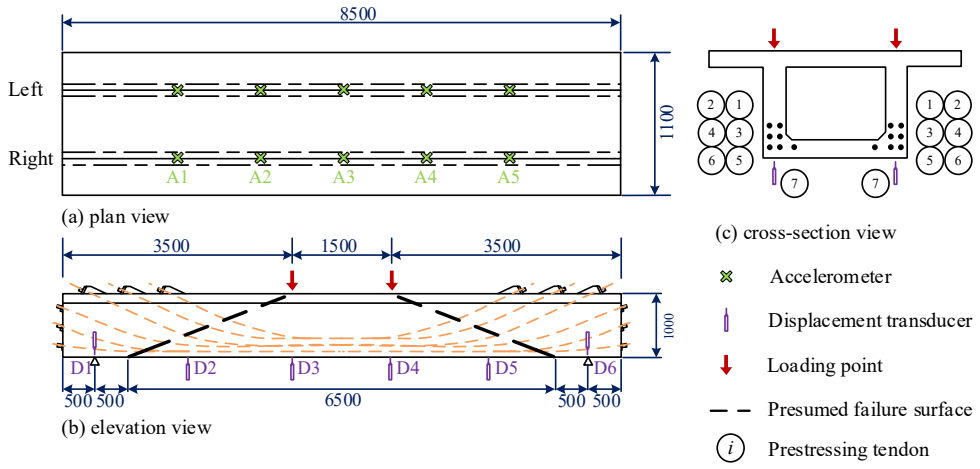

Figure 2. Specimen design and sensor locations (unit: mm).

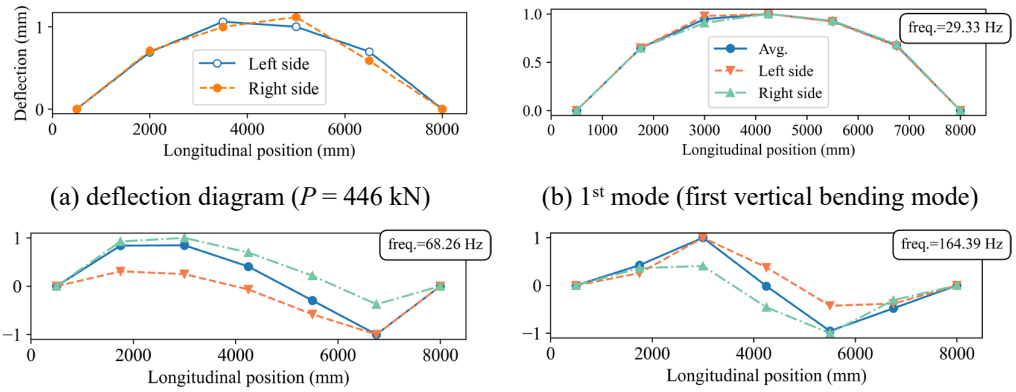

(a) deflection diagram (P = 446 kN)

(b) 1st mode (first vertical bending mode)

(c) 2nd mode (second bending-like mode)

(d) 3rd mode (second bending mode)

Figure 3. Target structural responses for linear model updating.

(MAC) is used as a normalized measure to evaluate the similarity between mode shapes. Therefore, "Scen. (k)_R1_T1", "Scen. (k)_R1_T0", and "Scen. (k)_R0_T0" correspond to the model classes "M_1", "M_2", and "M_3", respectively. For example, the label "Scen. 1_R1_T1" indicates that the updating scenario uses model class "M_1" and incorporates the frequencies and mode shapes of the first and second modes into the goodness-of-fit function.

The formulation of the goodness-of-fit function is based on observed physical quantities. In this study, data from vibration and static loading tests are utilized for model updating. As a result, the goodness-of-fit function, which includes both static and dynamic measurements, is defined as shown in Eq. (5). Since there is no explicit information regarding the weighting of errors associated with the identified modal properties and measured static deflections, equal weights are assigned to both data sources.

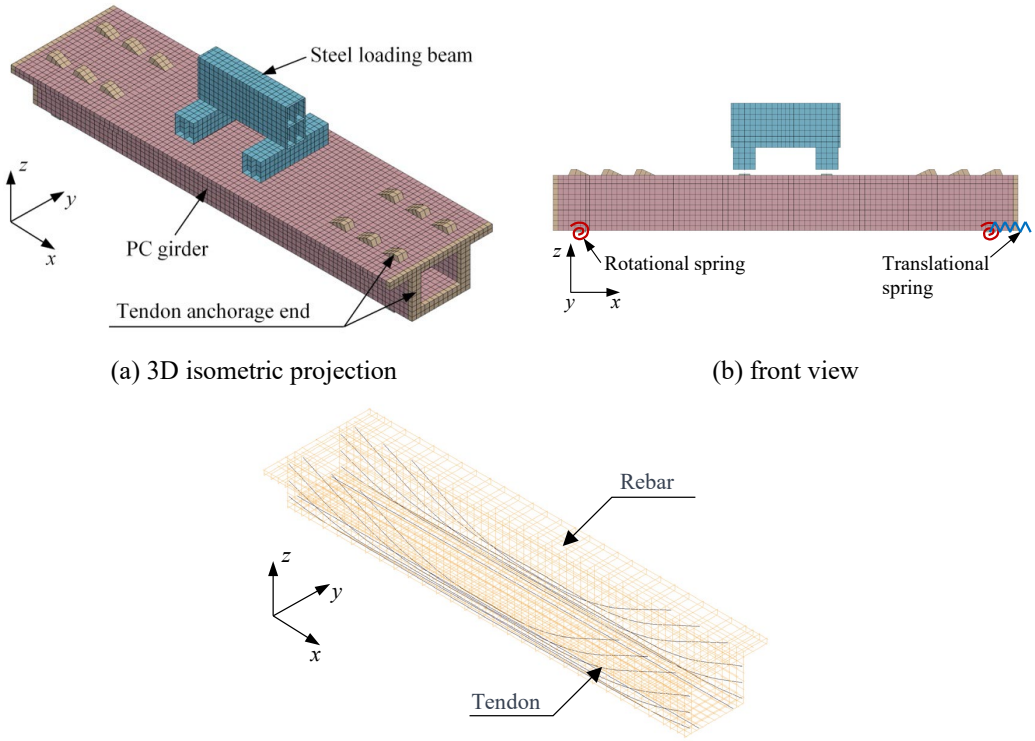

(a) 3D isometric projection (b) front view

(c) rebar arrangement inside

Figure 4. 3D FE model established in DIANA.

$$J_g(\boldsymbol{\theta}) = \sum_{i=1}^{N_m} \left(\left(1 - f_i(\boldsymbol{\theta})/\hat{f}_i\right)^2 + \left(1 - \langle \varphi_i(\boldsymbol{\theta}), \hat{\varphi}_i \rangle\right)^2 \right) + \xi \sum_{i=1}^{N_d} \left(1 - \delta_i(\boldsymbol{\theta})/\hat{\delta}_i\right)^2 \quad (5)$$

where $f_i(\boldsymbol{\theta})$ and $\varphi_i(\boldsymbol{\theta})$ respectively represent the frequencies and mode shapes derived from the eigenvalue analysis by the finite element method (FEM). Moreover, $\hat{f}_i$ and $\hat{\varphi}_i$ respectively denote the measured modal properties obtained from the experiment; $\delta_i(\boldsymbol{\theta})$ and $\hat{\delta}_i$ respectively stand for the simulated deflection by FEM and the measured deflection. ξ can take values of 0 or 1, depending on whether the static deflection is used for model updating. In addition, N_m expresses the count of identified modal properties orders, whereas N_d signifies the number of deflection sensors.

In solving inverse problems for model updating, simulation-based methods are typically employed to sample from the posterior distribution and estimate the MPVs of model parameters. These methods require repeated evaluations of the likelihood function, which in turn requires repeated evaluations of the FE model. This results in a substantial computational burden, making the process very time-consuming, especially for large-scale and complex bridge structures. One way to alleviate this computational burden is by reducing the cost of likelihood function evaluations. This can be achieved by approximating FE model solutions using surrogate models.

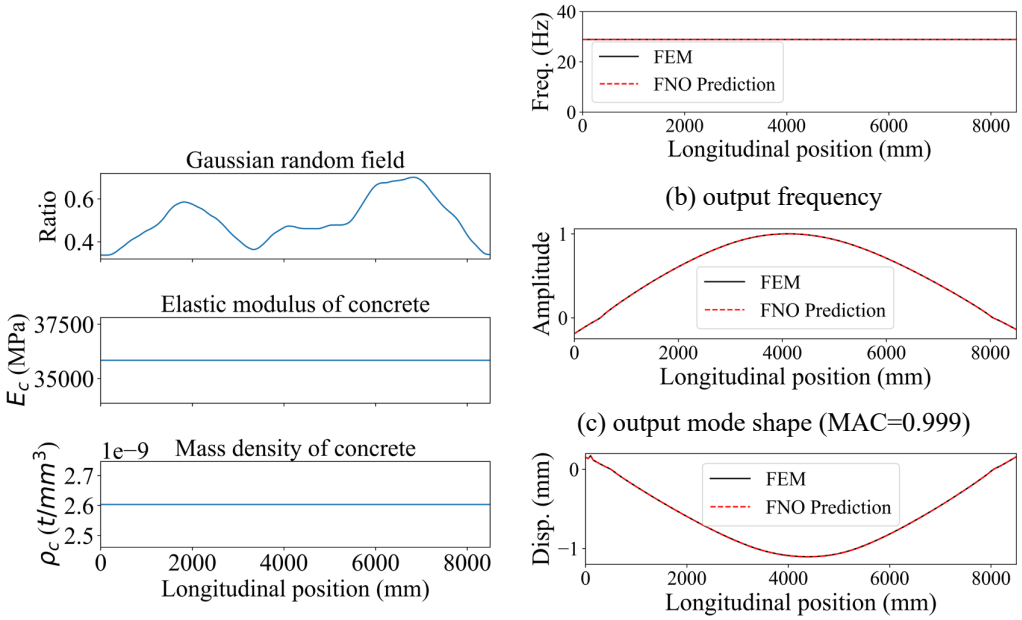

Figure 5. Prediction performance of FNO on the test dataset.

In this study, the FNO is utilized as a surrogate model to approximate solutions for both the equation of motion and the bending differential equation. For the linear model updating process, the training data for the FNO-based surrogate model include a Gaussian random field along the beam axis with a mean value of 1.0, along with random variables representing the elastic modulus and mass density of concrete. The Gaussian random field is multiplied with the elastic modulus and mass density, respectively, during the calculation of structural responses. The output from the FNO-based surrogate model consists of the first bending frequency, the vertical bending mode shape, and the elastic deflection. Figure 5 illustrates the predictions of the FNO-based model on the test dataset. After being trained on 3,000 data pairs, the model shows excellent accuracy in predicting the natural frequency and mode shape of the first bending mode, as well as the elastic deflection, exhibiting strong agreement with the FE-simulated model responses in the test dataset.

3.2. Model updating results and model class selection

As an illustrative example, Figure 6 presents histograms of the material property samples collected at the final stage of TMCMC for the “Scen. 1_R1_T1” scenario. Figures 7 shows the histograms of the final-stage samples, respectively, for the “Scen. 3_R0_T0” scenario.

As shown in Figure 6, for the “Scen. 1_R1_T1” scenario, a key observation was the alteration in the second bending mode shape when the longitudinal spring stiffness value was modified. This change was reflected in a significantly higher MAC value for the second mode after the

model updating, indicating improved alignment with the measured mode shape. Although the updated model responses more closely matched the measured data, the introduction of additional translational and rotational constraints (see Figure 4(b)) in the boundary conditions raised concerns about the physical interpretation of the material parameters, which deviated noticeably from the reference values. The results suggest that vibration-based model updating, which relies solely on modal properties in the goodness-of-fit function, is highly sensitive to the boundary conditions.

Figure 7 shows that incorporating both static and dynamic data, including the first bending mode and elastic deflections, in the model updating process for the "Scen. 3_R0_T0" scenario resulted in accurate estimates of material parameters, which closely matched the reference values. Furthermore, the simulated responses from the calibrated model demonstrated strong agreement with the measured data. Therefore, using both static and dynamic response data for cross-verification is crucial to ensure the reliability of the calibrated model.

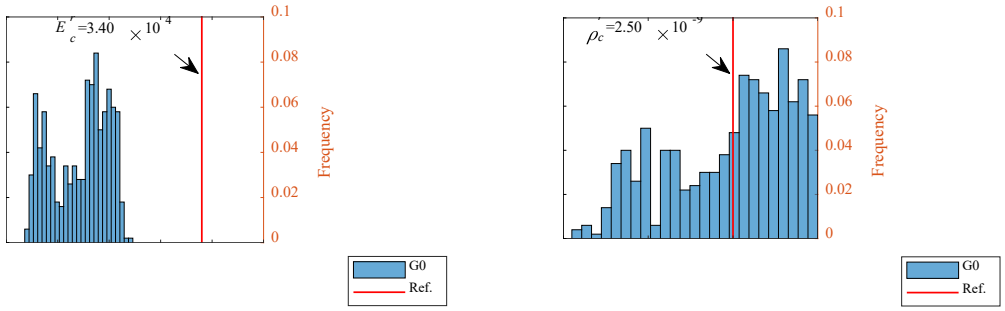

(a) elastic modulus of concrete (b) mass density of concrete

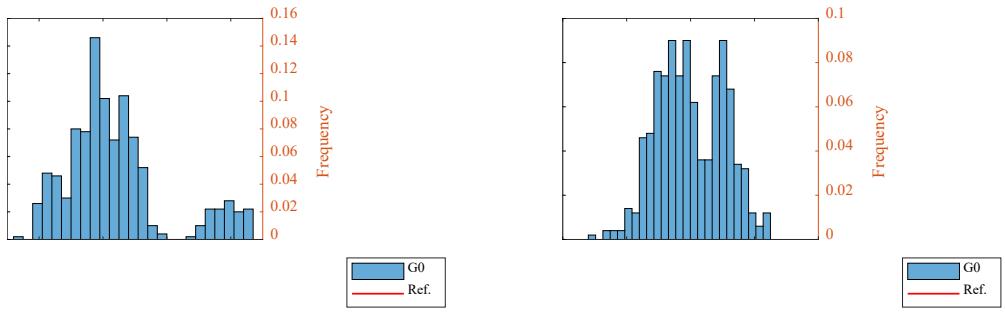

(c) spring constant of rotational spring (d) spring constant of translational spring

Figure 6. Histogram of samples for scenario "Scen. 1_R1_T1".

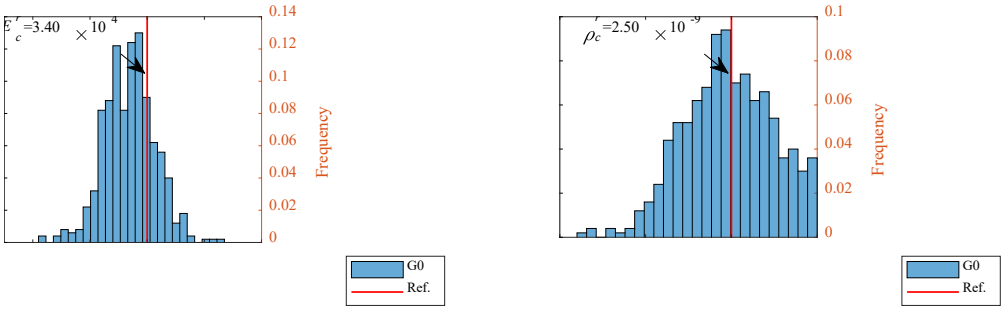

(a) elastic modulus of concrete (b) mass density of concrete

Figure 7. Histogram of samples for scenario “Scen. 3_R0_T0”.

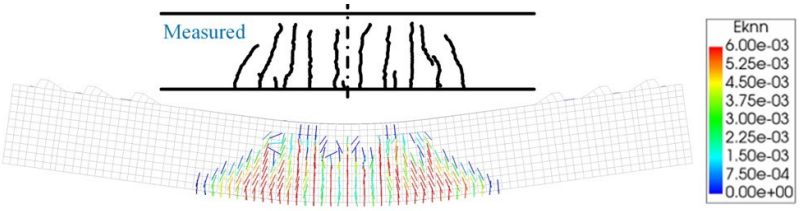

Figure 8. Measured and simulated crack patterns.

3.3. Nonlinear model predictions

Figure 8 presents a comparison between the measured and simulated crack patterns for the specimen. The crack pattern predicted by the calibrated FE model closely matched the experimental results. This suggests that the FE model, updated using elastic structural responses, can accurately predict the nonlinear structural behavior of the PC girder when nonlinear material properties derived from coupon tests are applied.

Figure 9 compares the simulated load-deflection curve with the measured curve. To evaluate the predictive capabilities of the digital twin for PC girder bridges, specifically regarding structural performance under corrosion deterioration, the calibrated model was used to assess tendon damage. The comparison revealed that the simulation underestimated the ultimate load-bearing capacity of the specimen by 9.6%. As part of the parameter sensitivity analysis, both the yield strength and ultimate strength of the prestressing tendons were adjusted by ±10% relative to the test values. The resulting load-deflection curves are shown within the shaded region in the figure. When variations in tendon strength were accounted for, the experimental ultimate load-bearing capacity more closely matched the upper bound of the simulated values. This confirms the reliability of the calibrated FE model and the proposed simulation procedures for modeling tendon ruptures.

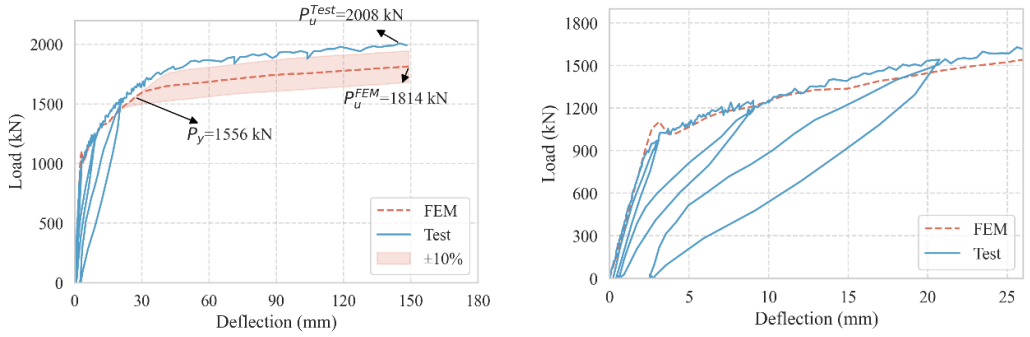

(a) load-deflection curve (b) enlarged view

Figure 9. Measured and simulated load-deflection curves.

4. Conclusions

This study introduces a digital twinning Bayesian model updating approach tailored for PC girder bridges, aiming to improve structural damage assessment in the field of structural health monitoring. The main goal is to integrate existing measured data with a high-fidelity FE model to establish a physics-based digital twin for PC bridges. The following conclusions can be drawn from the research:

(1) While the model responses obtained through vibration-based model updating closely matched the measured data, concerns arose regarding the physical interpretation of material parameters that deviated significantly from the reference values. Incorporating static and dynamic data into the model updating process resulted in more accurate estimates of material properties. Furthermore, the simulated responses from the updated model aligned well with the measured data. To ensure the calibrated model's reliability, it is crucial to cross-verify it using multi-source data, particularly when both static and dynamic response data are available.

(2) The calibrated FE model proved effective in predicting nonlinear structural behavior, especially in capturing crack patterns and bending stiffness. The simulated load-deflection curves, which incorporated the proposed method for simulating tendon rupture, showed good agreement with experimental data. Consequently, the calibrated model serves as a physics-based digital twin for structural health monitoring applications, particularly for evaluating the performance of PC girder bridges after tendon rupture.

References

[1] Ierimonti L, Cavalagli N, Venanzi I, García-Macías E, Ubertini F. A Bayesian-based inspection-monitoring data fusion approach for historical buildings and its post-earthquake application to a monumental masonry palace. Bull Earthquake Eng. 2023;21(2):1139-1172.

[2] Zhou X, Kim CW, Zhang FL, Chang KC. Vibration-based Bayesian model updating of an actual steel truss bridge subjected to incremental damage. Eng Struct. 2022;260:114226.

[3] Torzoni M, Tezzele M, Mariani S, Manzoni A, Willcox KE. A digital twin framework for civil engineering structures. Comput Methods Appl Mech Eng. 2024;418:116584.

[4] Jeon CH, Shim CS, Lee YH, Schooling J. Prescriptive maintenance of prestressed concrete bridges considering digital twin and key performance indicator. Eng Struct. 2024;302:117383.

[5] Li Z, Kovachki N, Azizzadenesheli K, Liu B, Bhattacharya K, Stuart A, et al. Fourier neural operator for parametric partial differential equations. arXiv. 2020. Available from: https://arxiv.org/abs/2010.08895.

[6] Ching J, Chen YC. Transitional Markov chain Monte Carlo method for Bayesian model updating, model class selection, and model averaging. J Eng Mech. 2007;133(7):816-832.

[7] Kaewnuratchadasorn C, Wang JJ, Kim CW. Neural operator for structural simulation and bridge health monitoring. Comput Aided Civ Infrastruct Eng. 2024;39(6):872-890.

[8] Chen DB, Kim CW, Yoshida E, Sim C. Enhancing structural damage evaluation of PC girder bridges through digital twinning Bayesian model updating. Eng Struct. 2024;321:118974.

Development of recoverability index for structural systems from a perspective of system-reliability-based disaster resilience analysis

Taeyong Kim[1] **and Sang-ri Yi**[2*]

[1] Department of Civil Systems Engineering, Ajou University, Suwon, Republic of Korea
[2] Department of Civil and Environmental Engineering, University of California Berkeley, Berkeley, USA
* Correspondence: yisangri@berkeley.edu; Tel.: +1-510-229-2904

Abstract: This paper introduces a new recoverability index within the framework of system-reliability-based disaster resilience analysis. The proposed index quantifies recoverability by linking the final damage states of the system to the probabilistic resource demands necessary for structural recovery, while considering the aleatoric uncertainties in hazard. To account for post-disaster price inflation caused by the surge in recovery demand, the index incorporates a proportional relationship between regional-scale loss and associated price inflation. A numerical case study of a steel moment frame structure in the San Francisco area subjected to earthquakes demonstrates the feasibility of the proposed recoverability assessment workflow. The example highlights the importance of incorporating recoverability into resilience assessment.

Keywords: Disaster resilience; Recoverability; Structural reliability; Rapidity; Resourcefulness; Aleatoric uncertainties

1. Introduction

The concept of resilience has emerged as a prominent paradigm in disaster risk assessment, particularly in confronting inevitable structural damages from extreme events. According to the United Nations Office for Disaster Risk Reduction (UNDRR): "A resilient city is characterized by its capacity to withstand or absorb the impact of a hazard through resistance or adaptation, enabling it to maintain essential functions and structures during a crisis, and to bounce back or recover from an event" (Johnson & Blackburn, 2012).

While various approaches exist for evaluating resilience in civil structural systems, the system-reliability-based disaster resilience analysis framework (Lim et al., 2022) conceptualizes resilience through the "3R" criteria: reliability, redundancy, and recoverability. The framework first decomposes the failure of a system by a set of initial disruption scenarios. Then, reliability (β) and redundancy (π) indices are defined based on the probabilities of both component- and system-level failures associated with the initial disruption scenarios (Lim et al., 2022; Yi & Kim, 2023). The framework facilitates the identification of vulnerable components and failure paths that play a critical role in structural resilience.

Meanwhile, recoverability, representing the capacity of the system to restore the original or required functionality level of structures by replacing or repairing damaged structural components, is another crucial component of the resilience analysis framework. However, only limited research efforts have been made to develop methods for quantitatively evaluating the recoverability performance. To address this research gap, this study proposes a new recoverability index from a system reliability perspective. The recoverability index is defined by estimating the demand for recovery-related resources after a hazard event, accounting for the increase in price induced by a surge in demand attributed to the collective failure of neighboring structures subjected to the same hazard event. To be consistent with the established system-reliability-based disaster resilience analysis (Lim et al., 2022; Yi & Kim, 2023), the recoverability index is designed to be estimated for

each initial disruption scenario, thereby inheriting the aforementioned advantages of the original framework.

This paper provides a brief review of the system-reliability-based framework (Section 2) and introduces a new definition of the recoverability index (Section 3). A numerical demonstration of the recoverability index is presented for a three-story steel building structure and earthquake loads (Section 4). Finally, the paper concludes with a summary and remarks (Section 5).

2. High-level overview of system-reliability-based disaster resilience analysis

2.1. Reliability and redundancy indices

In system-reliability-based disaster resilience analysis, *reliability* is defined as the system's capacity to withstand component failures, whereas *redundancy* represents the system's ability to maintain functionality after initial component failures (Lim et al., 2022; Yi & Kim, 2023). These properties are quantified using the reliability and redundancy indices, defined as follows (Yi & Kim, 2023):

$$\beta_i = -\Phi^{-1}\big(P(F_i|H)\big) = -\Phi^{-1}\left(\int P(F_i|im,H) f_{IM}(im|H) dim\right) \tag{1}$$

$$\pi_i = -\Phi^{-1}\left(P\big(F_{sys}\big|F_i,H\big)\right) = -\Phi^{-1}\left(\frac{1}{P(F_i|H)}\int P\big(F_{\mathrm{sys}}\big|F_i,im,H\big)P(F_i|im,H) f_{IM}(im|H) dim\right) \tag{2}$$

where $\Phi^{-1}(\cdot)$ is the inverse cumulative distribution function (CDF) of the standard normal distribution, F_i denotes the *i*-th initial disruption scenario, H stands for the hazard event, im refers to the intensity measure characterizing the hazard's intensity, $f_{IM}(im|H)$ is the probability density function (PDF) of im given the hazard event H, and F_{sys} is the system-level failure event.

To alleviate the computational burden in estimating reliability and redundancy indices for every initial disruption scenario, several methods have been developed (Kim & Yi, 2024; Kim et al., 2024).

2.2. Resilience threshold

Provided that the initial disruption scenarios are mutually exclusive and collectively exhaustive (MECE), the annual failure probability of the structural system given a hazard event H, $P\big(F_{sys}\big)$, is expressed in terms of reliability and redundancy indices as follows:

$$P\big(F_{sys}\big) = \sum_i P\big(F_{sys,i}\big) = \sum_i P\big(F_{sys}\big|F_i,H\big)P(F_i|H)\lambda_{H_j} = \sum_i \Phi(-\pi_i)\Phi(-\beta_i)\lambda_H \tag{3}$$

in which $P(F_{sys,i})$ denotes the annual probability of the system failure event originating from the *i*-th initial disruption scenario under H, and λ_H stands for the annual mean occurrence rate of H.

To set a resilience threshold, the *de minimis* risk level P_{dm}, which serves as the upper bound for the system failure probability $P\big(F_{sys}\big)$, can be introduced. The resilience threshold is defined as:

$$P\big(F_{sys}\big) = \sum_i \Phi(-\pi_i)\Phi(-\beta_i)\lambda_H < P_{dm} \tag{4}$$

By enforcing equal weights across the initial disruption scenarios and additionally introducing the recoverability index $\gamma_i \in [0,1]$ that serves as a reduction factor for the threshold (i.e. low recoverability index enforces more stringent threshold), Eq. (4) can be re-formulated as a combination of reliability-redundancy-recoverability indices for each initial disruption scenario as (Yi & Kim, 2024)

$$\frac{\Phi(-\pi_i)\Phi(-\beta_i)}{\gamma_i} < \frac{P_{dm}}{\lambda_H N_F} \tag{5}$$

where N_F is the number of MECE initial disruption scenarios, and $P_{dm}/(\lambda_H N_F)$ represents a factored per-hazard *de minimis* risk or resilience threshold.

3. Proposal of recoverability Index

3.1. Recoverability index from the perspective of system-reliability

We define *recoverability* as the estimated amount of resource, denoted as r, required to restore a system to its original state after disruption. To account for the inherent uncertainties in resource demand, the statistical representation of resource demand is defined as:

$$R_i = E[h(r)] = \int h(r) f_{r|F_i}(r|F_i)\, dr \tag{6}$$

where $E[\cdot]$ is the mathematical expectation, $h(r)$ is a measure defining the statistics of interest (e.g. $h(r) = r$ if R_i represents the mean of r), and $f_{r|F_i}(r|F_i)$ is the PDF of the resource demand r given the i-th initial disruption scenario. While various forms of resource demand (e.g. time or cost) could be used to define r, this study employs repair costs as the primary measure of resource demand.

To evaluate $f_{r|F_i}(r|F_i)$ in Eq. (6), we assume that the i-th initial disruption scenario F_i results in one of the final damage states G_j , $j = 1, \dots, N_G$, where N_G is the total number of damage states. Then, $f_{r|F_i}(r|F_i)$ is expressed as

$$f_{r|F_i}(r|F_i) = \int \sum_j f_{r|G_j}(r|G_j, im) P(G_j|F_i, im)\, f(im|F_i)\, dim \tag{7}$$

where $f_{r|G_j}(r|G_j, im)$ is the PDF of resource demand given the j-th damage state and im, and $P(G_j|F_i, im)$ denotes the probability of occurrence of the j-th damage state given the i-th initial failure scenario and im.

The recoverability index for the i-th initial disruption scenario, γ_i is, then, defined using R_i as

$$\gamma_i = f_{RA}(R_i) \tag{8}$$

where f_{RA} is a "resource-attitude" function. This function converts R_i to a value between zero and one. A possible example of the resource-attitude function is written as

$$\gamma_i = \max(k_R R_i + 1, \gamma_{\min}) \tag{9}$$

where $k_R \leq 0$ is a slope parameter that controls the resource-attitude, and $\gamma_{\min} > 0$ is a lower bound of the index.

3.2. Consideration of demand surge

The collective failure of neighboring structures can result in demand surges for recovery-related resources, such as materials and labor. These surges may manifest as price inflation and impede recovery. To account for these potential effects, we separate the resource demand into two terms - the first term representing the resource demand estimated under normal conditions (i.e., without a demand surge) and the second term representing an increase of actual required resources after the surge:

$$r = r^b(G_j) \cdot \alpha_{DS}(im) \tag{10}$$

where r^b is the baseline resource demand and α_{DS} is the adjustment factor.

The adjustment factor is estimated by assuming that the price inflation amount is proportional to the regional-scale loss amount. Furthermore, the regional-scale loss is assumed to be a function of the intensity measure im observed at the target site. Thus, the price inflation factor is expressed as a function of im:

$$\alpha_{DS}(im) = \max\left(\frac{L_{city}(im)}{L_{ref}}, 1\right) \tag{11}$$

where $L_{city}(im)$ denotes the estimated regional-scale loss for a given im, and L_{ref} is the reference regional-scale loss that begins to induce price increases. To estimate $L_{city}(im)$ in Eq. (11), the following linear function is assumed:

$$L_{city}(im) = a \ln im + b \tag{12}$$

where a and b are regression coefficients determined through regional-scale risk assessment.

4. Numerical Investigation

4.1. Target structural system and hazard description

Figure 1 presents a steel frame structure modeled using OpenSees (McKenna, 2011), employed to demonstrate the proposed recoverability index. The structure is assumed to be located in the San Francisco area, being susceptible to strong earthquakes. The beam width is 300 inches, with the height of the first story set at 150 inches and subsequent story heights at 120 inches. The Young's modulus for the steel material is specified as 29,000 ksi. For the structural elements, W27×102 sections are used for the beams, and W24×131 sections for the columns. Rotational springs are incorporated to model plastic hinges in the frame, utilizing a modified Ibarra-Krawinkler deterioration model (Ibarra & Krawinkler, 2005). The parameters for these springs are derived from the work of Lignos & Krawinkler (2012)

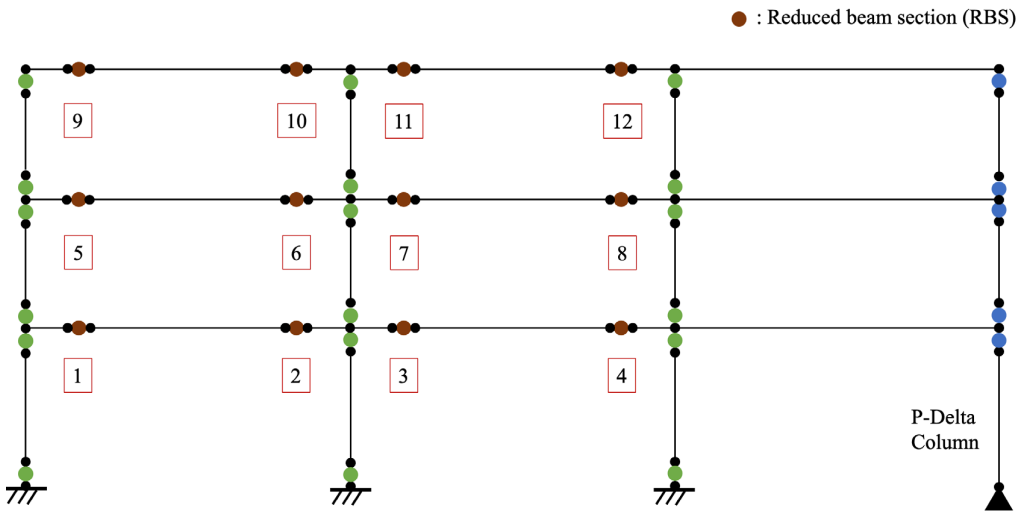

Figure 1. Steel frame structure

The initial disruption scenarios (F_i) are defined as the possible combinations of failures in the reduced beam section (RBS) connections ($C_j, j = 1,2,\dots,12$). A total of 12 RBS components are considered in this analysis. The final damage configurations **G** are assumed to be the same as **F**, considering the importance of the RBS connection in the evaluation of structural loss.

To estimate the reliability and redundancy indices, both component- and system-level failure limit states are defined. The component-level limit state is characterized by the seismic moment demand in the RBS connection exceeding a predefined threshold. The system-level limit state, on the other hand, is defined in terms of the roof-top drift ratio. The changes in structural behavior following damage to a structural component in F_i is modeled by reducing the initial stiffness of the affected components. In particular, a 60% reduction in stiffness is assumed for the components after experiencing initial damage.

Furthermore, 50 recorded ground motions are selected whose response spectra closely match the design spectrum of the target site. The design spectrum is derived using the ground motion prediction equation (GMPE) developed by Boore & Atkinson (2008). Spectral acceleration Sa is selected as the IM. Further details of the parameters used to develop the design spectrum and ground motion information can be found in Yi & Kim (2023). For a detailed procedure on obtaining reliability and redundancy indices and interpretation of the outcome, the readers are referred to Yi & Kim (2023) as the remaining section focuses solely on the recoverability index.

4.2. Estimation of the recoverability index

The first step in estimating the recoverability index is to compute $P(G_j|F_i, im)$ in Eq. (7) for each pair of F_i and G_j along with im. To achieve this, we employed multinomial logistic regression using sample pairs of Sa and their corresponding final damage indices. Figure 2 presents an example of estimated $P(G_j|F_i, im)$ for F_i =C1-4, in which several notable final damage scenarios G_j are labeled in

the plot. Note that F_i =C1-4 corresponds to the failure of RBS connections 1, 2, 3, and 4, as indicated by the red boxes in Figure 1.

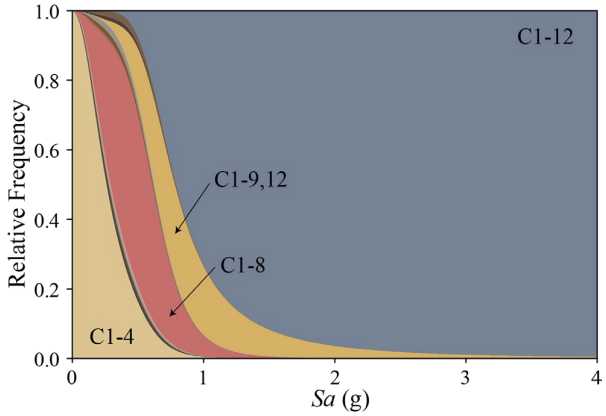

Figure 2. $P(G_j|F_i, im)$ where F_i =C1-4

The repair cost of the RBS connections is chosen as the primary metric for resource demand when estimating the recoverability index. To estimate the baseline repair cost $r^b(G_j)$, we employed the probability distribution of structural loss indicated in FEMA P-58 (FEMA, 2012b), defined in terms of the quantity of damaged building components. To account for demand surges, a regional-scale seismic performance assessment is conducted. City-scale resource demand is simulated using the Regional Resilience Determination (R2D) tool developed by SimCenter (McKenna et al., 2024). Through the tool, a total of 300 spatially correlated realizations of Sa at each building site are generated for different rupture locations and magnitudes and used as input for HAZUS damage curves to estimate the associated repair costs (FEMA, 2012a). Figure 3(a) provides a summary of the regional performance assessment for a single realization, with the target building site highlighted by a black dot. Figure 3(b) presents the 300 realizations of Sa at the target site and city-level repair costs.

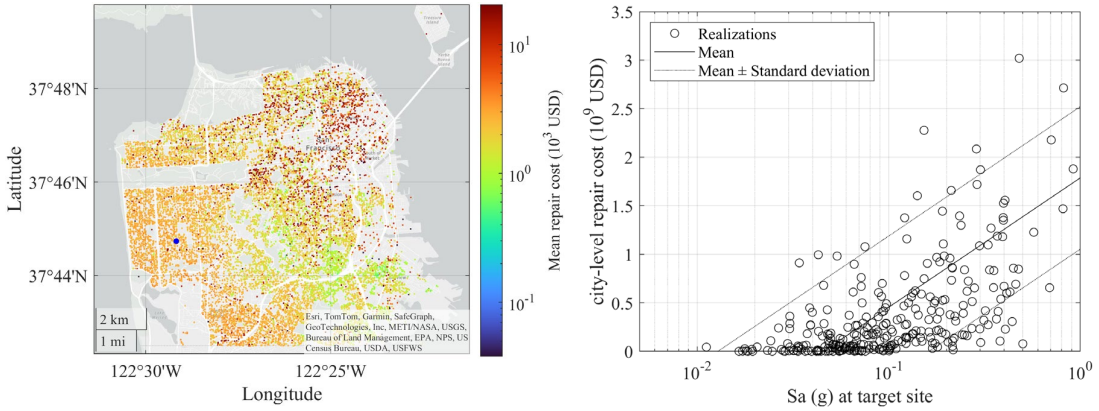

Figure 3. Regional performance assessment to estimate city-level repair demand: (a) realization of regional loss, and (b) city-scale loss versus intensity measure

A linear regression analysis is performed based on Eq. (12), and the estimated regression curve is shown in Figure 3(b). In this example, the estimated regression parameters are a = 579 (×10⁶ USD) and b = 1,788 (×10⁶ USD), with a mean squared error (standard deviation) of 737 (×10⁶ USD). The solid orange line represents the mean predicted repair cost, while the gray dotted lines represent the mean ± one standard deviation.

4.3. β–π–γ diagram

The β–π–γ diagram is presented in Figure 4. Each dot represents an initial disruption scenario, where the recoverability indices are represented by colors, and the resilience thresholds for two different recoverability values (0.718 and 0.1) are also presented under the assumption of $P_{dm}/(\lambda N_F) = 5 \times 10^{-5}$. Two scenarios, i.e., C1,4 and C1-12, are highlighted because they are situated near the resilience threshold lines. The recovery indices for these two scenarios are 0.718 and 0.1, respectively, and their corresponding resilience threshold curves are shown using the same colors. The diagram indicates that neither scenario meets the resilience criteria.

To address the identified lack of resilience, retrofit or design modification strategies could be implemented to enhance the reliability, redundancy, or recoverability of these scenarios. It is important to note that, if potential price inflation had not been accounted for, the recoverability index for scenario C1-12 would have been evaluated as $\gamma = 0.40$, and the scenario would have been assessed as satisfying the resilience criteria. Therefore, in the current case study, the impact of price inflation significantly affected the resilience assessment outcomes.

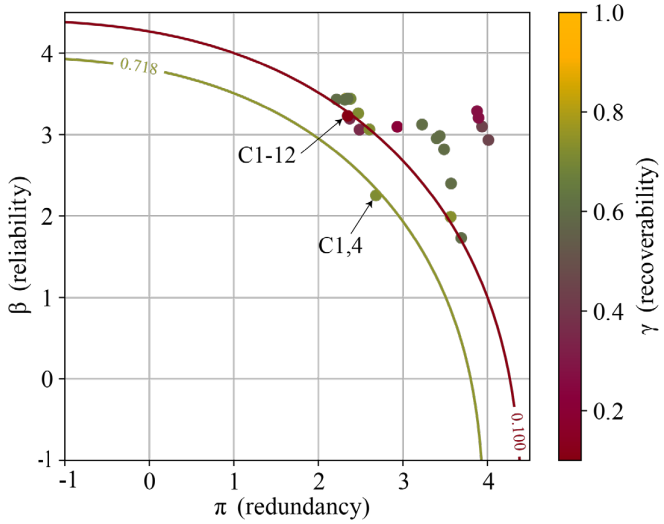

Figure 4. Resilience assessment results presented in terms of β–π–γ diagram

5. Conclusions

This paper proposed a new recoverability index from the perspective of system-reliability-based disaster resilience analysis. The recoverability index is formulated by first identifying a set of final damage states and their probabilities and associating those damage states with the recovery resource demands. The developed index can account for potential post-disaster price inflation resulting from demand surges. This is achieved by establishing an empirical relationship that relates regional-scale losses to price increases. A numerical example of a steel moment frame located in the San Francisco area was presented to illustrate the proposed methodology. In this example, initial disruption scenarios and final damage configurations were defined in terms of the failure of reduced beam section connections. The results highlighted the significance of incorporating recoverability into resilience analysis.

Building on this work, two potential research directions are proposed. First, the incorporation of more advanced socio-economic models could improve the understanding of the relationship between city-scale losses and demand surges. Second, the integration of the proposed framework with the well-known recovery curve (also known as resilience triangle model) model (Bruenau et al., 2003) could be explored. This integration would allow the system-reliability-based disaster resilience analysis framework to be used not only for resilience performance assessment but also for the determination of optimal post-hazard recovery sequences.

Acknowledgment: This research was supported by the National Research Foundation of Korea (NRF) grant funded by the Korea government (MSIT) (RS-2023-00242859).

References

Boore, D. M., & Atkinson, G. M. (2008). Ground-motion prediction equations for the average horizontal component of PGA, PGV, and 5%-damped PSA at spectral periods between 0.01 s and 10.0 s. Earthquake Spectra, 24(1), 99–138.

Bruneau, M., Chang, S. E., Eguchi, R. T., Lee, G. C., O'Rourke, T. D., Reinhorn, A. M., Shinozuka, M., Tierney, K., Wallace, W. A., & Von Winterfeldt, D. (2003). A framework to quantitatively assess and enhance the seismic resilience of communities. Earthquake Spectra, 19(4), 733–752.

Federal Emergency Management Agency (FEMA). (2012a). Multi-Hazard loss estimation methodology. Earthquake model – HAZUS MH 2.1 Technical Manual, Washington, USA.

Federal Emergency Management Agency (FEMA). (2012b). Seismic Performance Assessment of Buildings Volume 1-Methodology. Rep. No. FEMA P-58-1, Washington, USA.

Ibarra, L. F., & Krawinkler, H. (2005). Global collapse of frame structures under seismic excitations. John A. Blume Earthquake Engineering Center, Stanford Univ, CA: https://blume.stanford.edu/tech_reports

Johnson, C., & Blackburn, S. (2012). Making cities resilient report 2012. My city is getting ready! *A global snapshot of how local governments reduce disaster risk*. United Nation Office for Risk Reduction.

Kim, J., Yi, S. R., Park, J., & Kim, T. (2024). Efficient System Reliability–Based Disaster Resilience Analysis of Structures Using Importance Sampling. Journal of Engineering Mechanics, 150(11), 04024081.

Kim, T., & Yi, S. (2024). Accelerated system-reliability-based disaster resilience analysis for structural systems. Structural Safety, 109, 102479.

Lim, S., Kim, T., & Song, J. (2022). System-reliability-based disaster resilience analysis: Framework and applications to structural systems. Structural Safety, 96, 102202.

McKenna, F. (2011). OpenSees: a framework for earthquake engineering simulation. Computing in Science & Engineering, 13(4), 58–66.

McKenna F., Gavrilovic S., Zhao J. Zhong K., Zsarnoczay A., Cetiner B., Yi S., Bangalore Satish A., Naeimi S., & Arduino P. (2024). NHERI-SimCenter/R2DTool: Version 4.2.0 (v4.2.0). Zenodo. https://doi.org/10.5281/zenodo.11175489

Yi, S., & Kim, T. (2023). System-reliability-based disaster resilience analysis for structures considering aleatory uncertainties in external loads. Earthquake Engineering & Structural Dynamics, 52(15), 4939–4963.

System-reliability-based disaster resilience analysis of power grids for causality-based decision support

Youngjun Kwon[1], and Junho Song[2]

[1]Department of Civil and Environmental Engineering, Seoul National University, 08826, South Korea
[2]Department of Civil and Environmental Engineering, Seoul National University, 08826, South Korea;
e-mail: junhosong@snu.ac.kr

ABSTRACT

Civil infrastructure systems have become increasingly complex and vulnerable to a wide range of disaster risks due to rapid social development. The urgency of addressing climate change further underscores the need for system managers and policymakers to take prompt and prudent actions to mitigate the socio-economic impacts of diverse risks. The concept of disaster resilience has emerged as prominent in this context, referring to the comprehensive capacity of a system and its surrounding society to effectively confront and manage such risks. This study employs a novel disaster resilience analysis framework to assess a regional power grid from a system reliability perspective. The framework delineates plausible hazard-induced outage scenarios and calculates component-level reliability indices (β) and final system-level redundancy indices (π) through a reliability-redundancy (β-π) analysis. The calculation of β incorporates the impact of spatial correlations of earthquakes on a series of transmission towers, while that of π considers subsequent line failures in cascading models reflecting the flow-based nature of the network. The framework facilitates quantifying the causality of individual lines in the seismic resilience of the system, utilizing β-π analysis results and a causal diagram illustrating the systems affected by hazards. This quantified causality helps avoid misunderstanding caused by spurious correlations arising from common source effects on the line states. A numerical example demonstrates the pragmatic utility of the framework in evaluating the seismic resilience of power grids. The investigation emphasizes the importance of setting appropriate levels of line capacity to ensure the resilient operation of grids exhibiting complex cascading outages. Additionally, it is revealed that safeguarding specific lines may undermine the resilience of the entire grid. The examples in this study also serve as a valuable guide for decision-making strategies aimed at enhancing the seismic resilience of power grids, including anticipatory scenario management.

1. INTRODUCTION

Power systems are among the most essential civil infrastructure systems, underpinning a wide range of societal activities. As the demand for power supply increases due to population growth and urbanization, the resulting increased complexity and scale of these systems are coupled with a high vulnerability to inherent natural hazards such as earthquakes. Since potential damage caused by earthquakes can disrupt power systems and result in severe power outages, it is urgently required to assess the seismic resilience of the system and develop a comprehensive strategy to proactively strengthen its resilience by effective recovery plans.

Power systems composed of highly interdependent components carrying significant power loads during normal operation pose challenges for resilience analysis (Dobson et al., 2007). One of the challenges is found in incorporating cascading failure effects into power system vulnerability analysis, i.e., phenomena of a localized failure propagating through the system topology. Extensive studies have proposed risk mitigation strategies for power systems based on vulnerability analysis. For example, the cascading failure propagation can be controlled by optimizing the grid topology (Fang et al., 2015), adjusting the topology by adding edges (Lonapalawong et al., 2022), or distributing generators (Rohden et al., 2012). Another strategy is to deliberately remove or isolate certain components after an initial attack or failure to prevent cascading failures (Witthaut and Timme, 2015; Panteli et al., 2016).

In this paper, a system reliability-based framework (Lim et al., 2022; Kwon and Song, 2023) is applied to evaluate the seismic resilience of the power system against major failure scenarios. Then, the causal diagram describing the cascading failures in flow-based networks is incorporated into the resilience evaluation. Based on the components identified as those with negative contributions to seismic resilience from a causal viewpoint, we demonstrate the practicality of guiding operational decisions to improve the resilience of power grids. The paper concludes with a discussion of the seismic resilience analysis of power grids and the applicability of causality-based decision support.

2. THEORETICAL BACKGROUND

2.1. *Disaster resilience analysis of networks from a system reliability perspective*

Lim et al. (2022) proposed the system-reliability-based disaster resilience analysis (S-DRA) framework for civil infrastructure systems, which was later applied for *infrastructure networks* scale by Kwon and Song (2023). This framework comprehensively considers the three aspects of the network's ability to withstand hazards – Reliability, Redundancy, and Recoverability. Figure 1 provides a concise illustration of the three network resilience criteria within the framework.

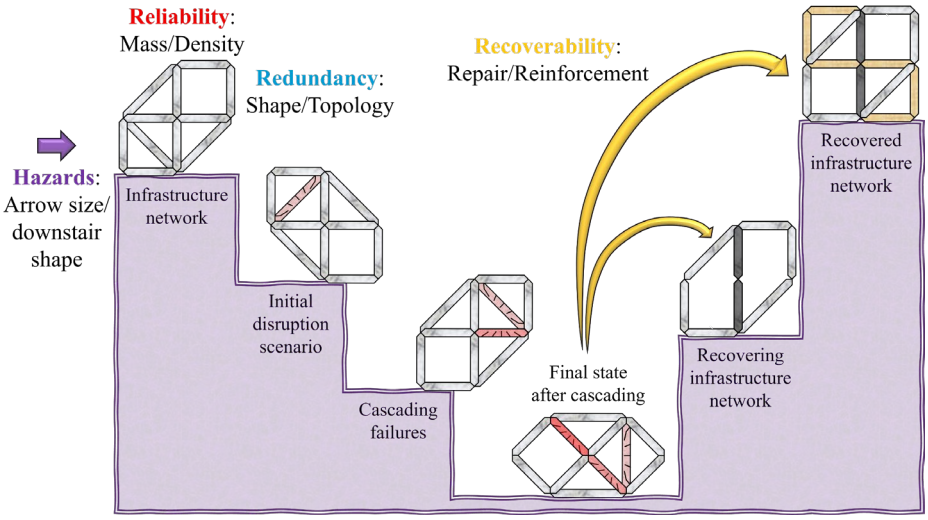

Figure 1 Disaster resilience criteria of infrastructure networks in the S-DRA framework

In the S-DRA framework, the reliability and redundancy criteria are evaluated using generalized reliability indices. For the ith initial disruption scenario among failures of k components, F_i^k, given the hazard H, the pair of the reliability index β_i^k and the redundancy index π_i^k is defined as

$$\left(\pi_i^k, \beta_i^k\right) = \left(-\Phi^{-1}\left(P\left(F_{sys}\middle|F_i^k, H\right)\right), -\Phi^{-1}\left(P\left(F_i^k\middle|H\right)\right)\right) \quad (1)$$

where $\Phi^{-1}(\cdot)$ is the inverse of the standard normal cumulative distribution function (CDF) and F_{sys} denotes the system-level failure event. The framework provides the disaster resilience constraint (domain) to identify the non-critical scenarios where the probability of system failure $F_{sys,i}^k$ is kept below the *de minimis* risk threshold P_{dm}, i.e.,

$$\mathcal{D}_{\lambda_H}: \Phi\left(-\pi_i^k\right)\Phi\left(-\beta_i^k\right) = \frac{P\left(F_{sys,i}^k\right)}{\lambda_H} < \frac{P_{dm}}{\lambda_H} \quad (2)$$

where $\Phi(\cdot)$ is the standard normal CDF and λ_H is the mean occurrence rate of H. P_{dm} is set to 10^{-7}/year in this paper. The scatter plot of the pairs $\left(\pi_i^k, \beta_i^k\right)$ from Eq. (1) with the resilience constraints in Eq. (2) is referred to as a β-π diagram, and the process of evaluating two resilience indices is termed β-π analysis.

2.2. *Cascading failure*

Simulating cascading failures in a power grid depends on describing the line protection mechanisms, i.e., line tripping. The overall process of cascading failures considered in this paper is described as follows:

1. *Physical disruption*: The structural failure of components caused by seismic hazards initiates cascading failures. The physical states of the lines are analyzed, which can be represented by structural damage to transmission towers. Possible disruption scenarios are identified, and their reliability indices are calculated.
2. *Identification/control of line states*: If the power flow on a line exceeds its capacity, the circuit breaker on the line trips to isolate the line from the grid, effectively taking it out of service. Each line is evaluated for its functionality and is controlled if necessary.
3. *Power flow analysis*: After removing the inoperative lines from the grid topology, the power flows in the lines are calculated. If the grids are divided into several islands, the power flow analysis is performed on each island separately.
4. *Evaluation of cascading failures*: Steps 2 and 3 are repeated until there are no active generators or additional overloads on all lines in each island. Finally, the effects of the initial scenario on the final degraded grid are analyzed to calculate the system reliability.

2.3. *Causal diagram and do-calculus*

To analyze the causal impact of component interventions on system resilience effectively, we employ a causal diagram, i.e., a directed acyclic graph (DAG) where nodes and arrows represent random variables and the causal influence between these variables, respectively. A well-constructed causal diagram plays a crucial role in answering causality-related queries regarding policy application (Pearl, 2009).

For variables X and Y, the causality of $Y = y$ under the control of $X = x$ is expressed as

$$P\left(Y = y\middle|do(X = x)\right) = P_{X=x}(Y = y) = P_x(y) \quad (3)$$

where $do(X = x)$ represents the intervention of setting X as x. The term in Eq. (3) is different from $P(Y = y|X = x)$ in that the former assesses the direct causality excluding the spurious association arising

from the confounders, the common sources influencing both X and Y. The causal effect of X on Y can be quantified by the difference or change ratio between the term in Eq. (3) and the term caused by the other outcome, $X = x'$, i.e., $P_x(y) - P_{x'}(y)$ or $P_x(y)/P_{x'}(y)$.

Do-calculus facilitates the computation of such queries using conditional probabilities from the system before the interventions. Among various methods in do-calculus, this paper employs a simple graphical test known as the "backdoor criterion." A pair (X, Y) in a DAG satisfies the backdoor criterion if a set of variables Z meets the following conditions: (1) no element of Z is a child of X, and (2) Z blocks all paths between X and Y that contain an arrow pointing to X. Such a set Z, known as an admissible set, can be used to determine the causality of the pair. The causality in Eq. (3) is calculated using all possible outcomes of Z, i.e.,

$$P\big(Y = y \big| do(X = x)\big) = \sum_{z} P(Y = y | X = x, Z = z) P(Z = z) \tag{4}$$

3. S-DRA OF A POWER GRID

3.1. *β-π analysis of a power grid*

Figure 2 shows a power grid near a seismic source and its β-π diagram for F_i^k $(k = 1, 2, 3)$ obtained from the β-π analysis. The reliability indices of lines are evaluated by structural analysis as [1.631, 1.850, 1.850, 1.946, 2.201, 2.121, 2.420, 2.504, 2.616, 2.736]. These values depend on the distances from the midpoint of the lines to the epicenter. The covariance matrix of the line states, $\mathbf{Z} \sim \mathcal{N}(\mathbf{0}, \mathbf{\Sigma})$ is formulated assuming that the correlation of Z_e of two lines with center distance Δ (km) is estimated as $\exp(-\Delta^{0.5})$.

The power grid operates with four generators supplying real power 125MVA and five load buses consuming real power 100MVA. In the direct current (DC) power flow analysis, the total power capacity of all lines is set to 125MVA×1.6=200MVA. A system-level failure is defined when the system-level performance falls below a threshold $\varepsilon = 1/3$ for the power grid.

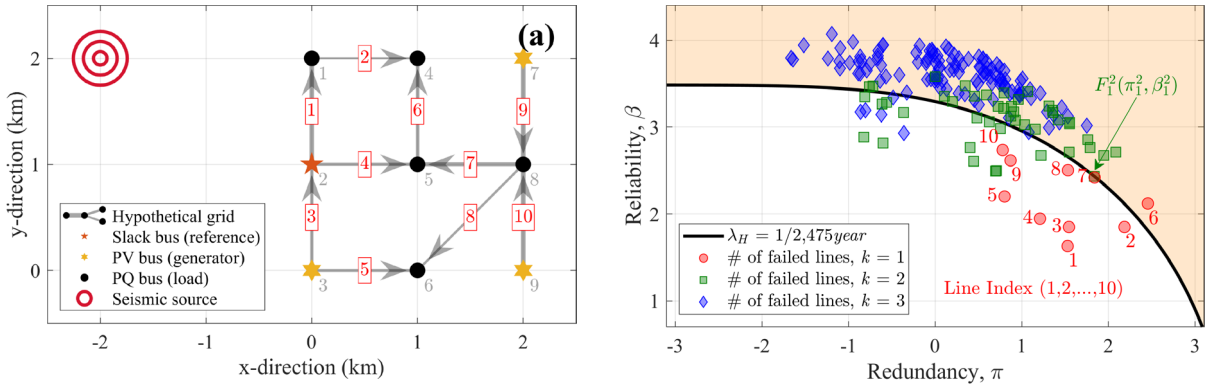

Figure 2 Example power grid: (a) configuration and (b) β-π diagram

The β-π diagram includes the makers representing disruption scenarios and the outside of resilience domains for the occurrence rate $\lambda_H = 1/2{,}475$year. This multi-dimensional diagram provides valuable insights into the criticality of the scenarios, facilitating effective system-level maintenance and rehabilitation strategies. For instance, for $k = 1$, line 6 has a lower reliability index than lines 7, 8, 9, and 10, while it falls within $D_{\lambda_H = 2{,}475\text{year}}$, due to its relatively high redundancy index.

3.2. *Causality-based importance measures for lines in a flow-based power grid*

Identifying the causal mechanisms that govern the network's response to external hazards is crucial for component-wise actions. Figure 3 shows the causal diagram for four stages of a flow-based network at from the component level to the system level implying the cascading failures by hazards. In this paper, the variables S_i, A_e, and C_e are Bernoulli random variables whose values are 1 for an occurrence or a failure and 0 otherwise.

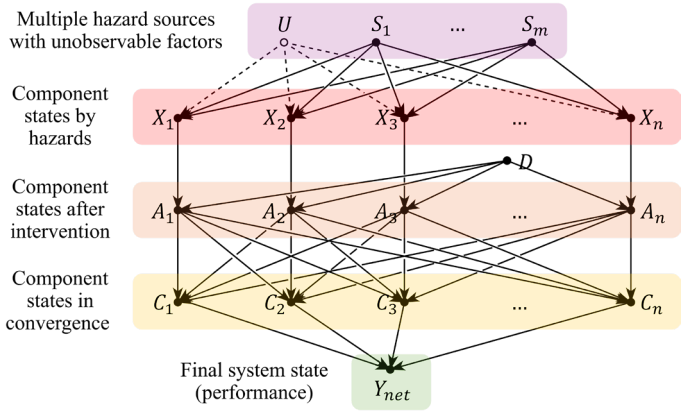

Figure 3 Causal diagram for a flow-based network affected by hazards

To support the operational decisions made at the component level, the β-π analysis results for multi-component failure scenarios need to be tailored. Thus, the causal contribution of line e along with other lines in scenario F to the final system's performance Y_{net} is quantified as

$$r_e^k(F) = 1 - \frac{P(Y_{net} \le \varepsilon | do(X_e = 0), F, H)}{P(Y_{net} \le \varepsilon | do(X_e = 1), F, H)} = 1 - \frac{P_{\bar{e}}\left(F_{sys} \middle| F, H\right)}{P_e\left(F_{sys} \middle| F, H\right)} \tag{5}$$

For a set consisting of mutually exclusive and collectively exhaustive (MECE) events with the states of the components in F_i^k excluding e, $\mathcal{F}_{i,e}^k$, the causal contributions in Eq. (5) are merged through the weighted sum incorporating the likelihood of its elements, i.e.,

$$MCC_{i,e}^k = \sum_{F \in \mathcal{F}_{i,e}^k} r_e^k(F) P(F|H) \tag{6}$$

Only for the scenarios outside of $\mathcal{D}_{\lambda_H}$, its system-level criticality, $\Phi\left(-\pi_i^k\right)\Phi\left(-\beta_i^k\right)$, is weighted averaged with merged causal contributions (MCCs) in Eq. (6). The causality-based importance measure (CIM) and the normalized CIM (NCIM) are proposed as

$$CIM_e^k = \sum_{i:\,(\pi_i^k, \beta_i^k) \notin \mathcal{D}_{\lambda_H}} \Phi\left(-\pi_i^k\right)\Phi\left(-\beta_i^k\right) MCC_{i,e}^k \tag{7}$$

$$NCIM_e^k = \frac{CIM_e^k}{\max_e\left(\left|CIM_e^k\right|\right)} \tag{8}$$

Figure 4 shows the NCIMs of a power grid for $\mathcal{D}_{\lambda_H = 1/475\text{year}}$, obtained using Eqs. (7) and (8). The positive NCIMs are mainly associated with lines 1, 4, and 5, which have high system-level criticality. It is noteworthy that some lines, e.g., 2, 6, and 7, have negative values for causal importance, whose redundancy indices are significantly high according to the β-π analysis.

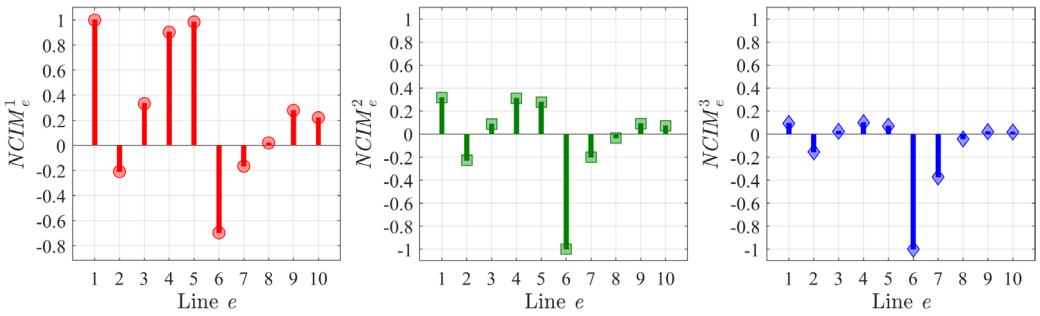

Figure 4 NCIMs of a power grid for $\lambda_H = 1/475\text{year}$

4. OPERATIONAL DECISIONS OF A POWER GRID BASED ON S-DRA

Considering that the signs of NCIMs stem from the causal contribution, the transition of lines 2, 6, and 7 from failure to non-failure adversely affects the system's performance. At the same time, the disaster resilience of the power grid can be improved solely based on its operational policies.

Figures 5 and 6 show the β-π diagram of the power grid with line 6 and lines 2 and 7 intervened as inoperative, i.e., $do(A_6 = 1)$-applied and $do(A_2 = 1, A_7 = 1)$-applied grid using Eq. (4), respectively. Seismic resilience is highly improved as the makers move to the safer resilience domain in the β-π diagram. In the enlarged diagrams, the redundancy indices for all lines except 6 increase for $k = 1$ compared to the original grid, while the reliability indices remain the same.

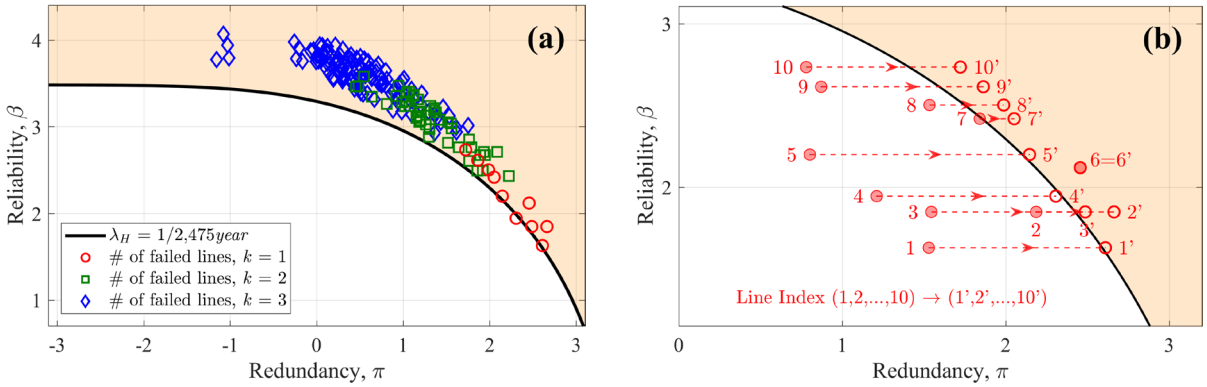

Figure 5 β-π diagrams of a power grid with line 6 intervened as inoperative

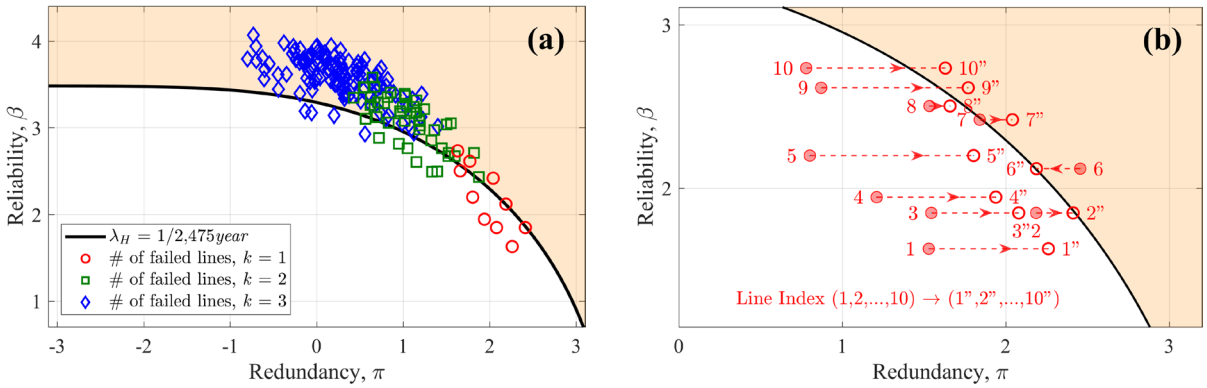

Figure 6 β-π diagrams of a power grid with lines 2 and 7 intervened as inoperative

For both interventions, the system failure probabilities decrease from 4.828×10^{-3} of the original grid to 3.138×10^{-4} and 7.208×10^{-4}, respectively. When balanced, depending on the effort required to control the state of lines 2 and 7 compared to that of line 6, or the imperative to maintain the redundancy of line 6, intervention candidates are deemed appropriate operational decisions for enhancing system reliability-based seismic resilience.

Figure 7 shows the performance of the final system by G_i^k for each k according to the interventions $\{6\}$ and $\{2,7\}$. Here, G_i^k represents a scenario intersecting F_i^k and the non-failures of components not in F_i^k. It is observed that, for each region of k, the maximum survivability is $1-\big(k+n(V)\big)/10$, where $n(V)$ represents the number of interventions. Notably, the fractions of scenarios with maximum survivability in the presence of interventions are smaller than the original grid. However, the fractions that progress to the worst outcome are also smaller.

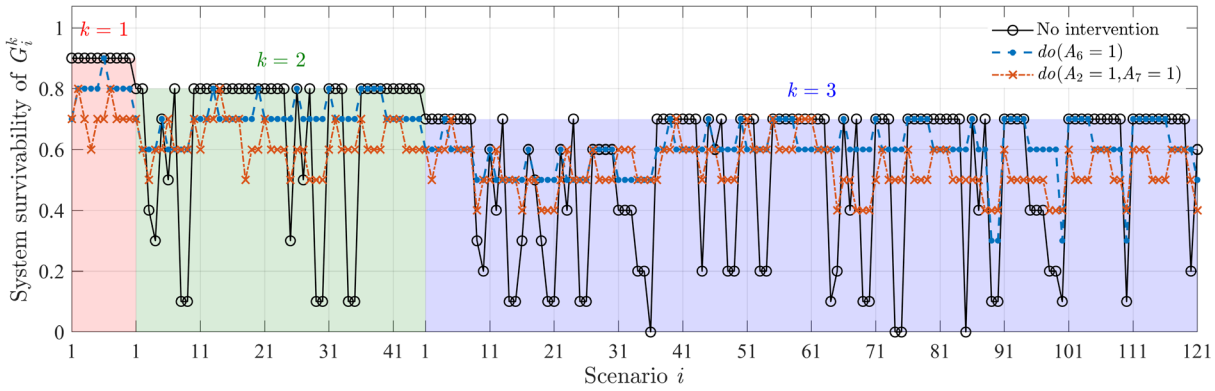

Figure 7 Final system-level performance of power grids according to interventions

Figure 8 and Figure 9 respectively show the NCIMs of a power grid with line 6 intervened and lines 2 and 7 intervened as inoperative for $\lambda_H = 1/475\text{year}$. Remarkably, both figures exhibit positive NCIMs for all lines, with zero values for the intervened components, contrasting with the NCIMs of the original grid in Figure 4. Although the intervention candidate does not encompass all the lines with negative NCIMs, intervening on some of these lines proves sufficient to change the importance of the remaining lines, shifting their NCIMs from negative to positive signs. In addition, the pattern of lines 1, 3, 4, and 5 dominating the positive NCIMs, with line 4 most prominent, is consistent with the results observed in the original grid.

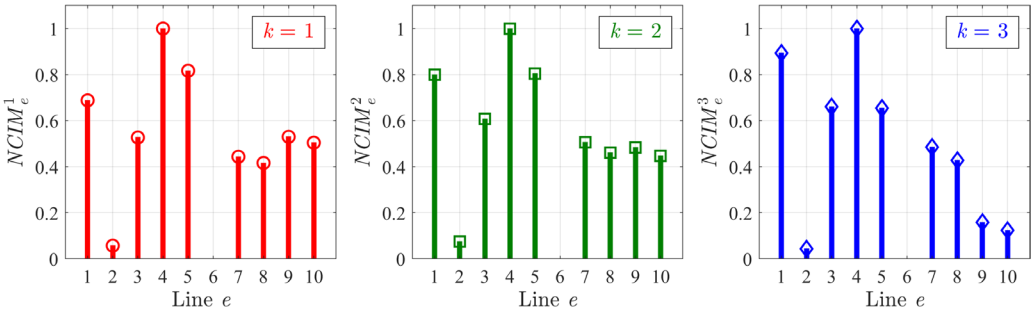

Figure 8 NCIMs of a power grid with line 6 intervened as inoperative for $\lambda_H = 1/475\text{year}$

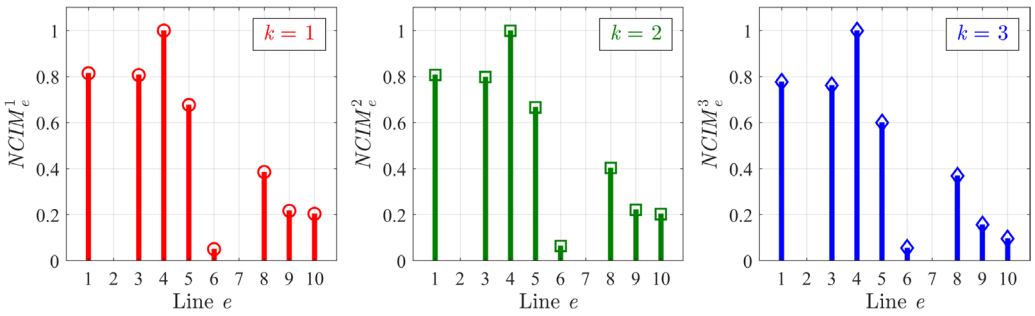

Figure 9 NCIMs of a power grid with lines 2 and 7 intervened as inoperative for $\lambda_H = 1/475$year

5. CONCLUSIONS

This study employed a system-reliability-based framework to assess the seismic resilience of power grids. Through in-depth analysis of the grid's reliability and redundancy, the framework provided a comprehensive perspective on the system's overall resilience to seismic events. Then, a causal diagram was developed to capture the effects of cascading failures from component states on system-level performance, forming the basis for proposing causality-based importance measures of a flow-based network. The proposed measures offer insight into the causal effects of specific components on overall system reliability, proving instrumental in guiding operational decision-making by identifying critical components where interventions could most effectively enhance resilience. The numerical example further substantiates the practicality and utility of these measures in supporting resilience-based decision-making for grid operations.

ACKNOWLEDGMENTS

The authors are supported by the National Research Foundation of Korea (NRF) grant funded by the Korea government (Ministry of Science and ICT, MIST) (Grant No. RS-2022-00144434).

REFERENCES

Dobson, I., Carreras, B. A., Lynch, V. E., and Newman, D. E. (2007). "Complex systems analysis of series of blackouts: Cascading failure, critical points, and self-organization." *Chaos: An Interdisciplinary Journal of Nonlinear Science*, 17(2).

Fang, Y., Pedroni, N., and Zio, E. (2015). "Optimization of cascade-resilient electrical infrastructures and its validation by power flow modeling." *Risk Anal.*, 35(4), 594-607.

Kwon, Y., and Song, J. (2023). "System-reliability-based disaster resilience analysis of infrastructure networks and causality-based importance measure." *ASCE-ASME J. Risk Uncertainty Eng. Syst. Part B: Mech. Eng.*, 9(3), 031104.

Lonapalawong, S., Yan, J., Li, J., Ye, D., Chen, W., Tang, Y., Huang, Y., and Wang, C. (2022). "Reducing power grid cascading failure propagation by minimizing algebraic connectivity in edge addition." *Front. Inf. Technol. Electron. Eng.*, 23(3), 382-397.

Lim, S., Kim, T., and Song, J. (2022). "System-reliability-based disaster resilience analysis: Framework and applications to structural systems." *Struct. Saf.*, 96, 102202.

Panteli, M., Trakas, D. N., Mancarella, P., and Hatziargyriou, N. D. (2016). “Boosting the power grid resilience to extreme weather events using defensive islanding.” *IEEE Trans. Smart Grid*, 7(6), 2913-2922.

Pearl, J. (2009). *Causality*. Cambridge university press.

Rohden, M., Sorge, A., Timme, M., and Witthaut, D. (2012). “Self-organized synchronization in decentralized power grids.” *Phys. Rev. Lett.*, 109(6), 064101.

Witthaut, D., and Timme, M. (2015). “Nonlocal effects and countermeasures in cascading failures.” *Phys. Rev. E*, 92(3), 032809.

UNDERSTANDING PEOPLE'S PSYCHOLOGICAL POLARIZATION DURING HAZARDS

Xiaolei Chu[1], **Guanren Zhou**[1], **Khalid M. Mosalam**[1], **and Ziqi Wang**[*1]

[1]Department of Civil and Environmental Engineering, University of California, Berkeley, United States

Abstract

The increasing connectivity and interaction among individuals significantly influence their collective reactions to stressors. When facing global threats such as pandemics and hurricanes, the interplay between hazards, emotions, and social networks can create a disproportion between the physical impacts of hazards and the emotional responses of individuals. We present a statistical-physics-inspired model to characterize hazard-induced emotional responses, uncover key trends in collective emotions, and identify conditions for emotional polarization. When applied to epidemiological and Twitter/X datasets from the COVID-19 pandemic in the United States, the model reveals the prevalence of negativity bias and underscores the significant role of social interactions in shaping emotional responses across over 80% of states. The model provides actionable insights for decision-makers to monitor, predict, and manage hazard-induced collective emotions and risks of polarization, contributing to the broader goal of building psychologically resilient communities.

Keywords: Community Resilience · Psychological Polarization · Hazards · Statistical Physics · Uncertainty Quantification

1 Introduction

Community resilience has emerged as a critical concern, requiring societies to withstand, adapt to, and recover from disasters[1]. This concept spans multiple dimensions, including physical, economic, and psychological resilience[2]. While the physical and economic impacts of hazards are relatively predictable, the emotional aftermath is more difficult to model. However, post-traumatic stress disorder (PTSD), anxiety, and depression have been widely reported following earthquakes, hurricanes, and pandemics[3,4,5,6,7,8,9,10]. For instance, a survey[5] found that 46% of participants met the screening thresholds for PTSD following Hurricane Harvey, and a study[11] reported that 54% of respondents experienced significant stress during the COVID-19 pandemic. These findings highlight the detrimental psychological impacts of hazards and their potential to trigger collective distress[12,13,14]. Therefore, emotional resilience[15,16,17], a critical facet of psychological resilience, warrants careful quantification and modeling. Despite its significance, computational models—especially interpretable models for characterizing the mechanisms of hazard-emotion-social network interactions—remain underdeveloped.

Qualitatively, emotional reactions to hazards are influenced by hazard intensity, individual emotional stability, and social interactions. The effects of the first two factors are relatively straightforward: a sufficiently destructive hazard can trigger mass hysteria, while emotional stability helps individuals resist stress. The influence of social interactions is shaped by the complex flow of information within social networks[13,18], making it challenging to anticipate. Diverse, heterogeneous information flows in social networks can foster collective rationality in response to hazards. However, pervasive information flows also amplify the viral spread of fear[14]. This calls for a quantitative model to characterize the competition between the risk amplification driven by social interactions and the inertia to align emotional states with the *objective* damage of hazards.

In this study, we formulate a statistical-physics-inspired model to describe hazard-induced emotional responses. We model the interaction of an individual with their environment using a local Hamiltonian function consisting of two groups of terms: (i) those representing emotional interactions on a social network, and (ii) those representing the direct

*Corresponding author. Email: ziqiwang@berkeley.edu

emotional impact of a hazard on a hazard damage-human interaction network. By assuming that collective emotional responses stabilize over the time window of interest (thermodynamic equilibrium) and homogenizing non-reciprocal interactions, we obtain the joint probability distribution of emotional responses in a population, expressed in the form of a Boltzmann distribution [19]. The system Hamiltonian, which characterizes this distribution, offers an analytical lens to study hazard-emotion-social network interactions.

Defining the proportion of high-stress emotions—termed emotional magnetization—as the macroscopic quantity of interest, we apply the Landau theory of phase transitions to the joint distribution model and obtain the mean-field system Hamiltonian and free energy. They reveal six fundamental parameters that influence collective emotion. We generate phase diagrams with different combinations of these six parameters to illustrate the global characteristics and conditions for sudden changes (phase transitions) in collective emotions. Moreover, we introduce a mean-field limit-state function in terms of the six fundamental parameters to characterize the boundary where half of the population is in a high-stress state. This limit-state function offers actionable insights for discerning and mitigating the trend of emotional polarization toward mass panic.

Finally, we apply the proposed model to epidemiological and Twitter/X data on COVID-19 in the United States. By conducting sentiment analysis on Twitter/X posts, we estimate the emotional magnetization for each U.S. state. Combining these estimates with epidemiological and mobility data, we perform Bayesian model inference to quantify two key parameters: the intensity of negativity bias and the relative importance of social interactions. Additionally, we conduct simulated control experiments to demonstrate the application of the proposed limit-state function in mitigating emotional polarization.

This study advances our understanding of the underlying mechanisms driving emotional resilience and polarization under hazards. The proposed probabilistic model characterizes how emotions are shaped by hazards and social interactions, as well as the drivers of emotional polarization. The findings lay a foundation for broader multidisciplinary research, including initiatives to address emotional stress arising from cultural shifts and evolving social norms.

2 Main Results

We present three main results: (i) a statistical-physics-inspired model for emotional responses to hazards; (ii) the mechanism underlying collective emotional responses and emotional polarization; and (iii) an application of the model to COVID-19 datasets.

2.1 Formulation of the Probabilistic Model for the Emotional Responses to Hazards

Hazards can cause physical damage to both people and infrastructure, potentially triggering collective anxiety in communities. To model this process, we consider two sets of discrete vectors: (i) damage states of infrastructures and/or individuals, denoted by $\boldsymbol{x} = [x_1, x_2, \ldots, x_{N_x}] \in \{0, 1, \ldots, L\}^{N_x}$, and (ii) emotional states of individuals, denoted by $\boldsymbol{y} = [y_1, y_2, \ldots, y_{N_y}] \in \{0, 1, \ldots, L\}^{N_y}$. We let 0 represent negligible damage or emotional impact, and L the maximum damage or emotional impact. Since deterministic modeling is infeasible, for a given time window of interest, we seek a probabilistic description of the emotional states given the hazard damage states. As illustrated in Fig. 1, we adopt a statistical-physics-inspired approach by constructing a parsimonious local Hamiltonian for an individual interacting with their environment, formulated as:

$$\mathcal{H}_i = \alpha \sum_{\mathbf{A}_{\boldsymbol{yy}}(j,i)=1} \Big((y_i - y_j)^2 - c\, y_i\, y_j \Big) + (1-\alpha) \sum_{\mathbf{A}_{\boldsymbol{xy}}(j,i)=1} (x_j - y_i)^2, \quad i = 1, 2, \ldots, N_y, \tag{1}$$

where $\alpha \in [0, 1]$ controls the relative importance of social interactions versus hazard damage, $c \in \mathbb{R}$ captures the asymmetry between low- and high-stress states, $\mathbf{A}_{\boldsymbol{yy}}$ is the adjacency matrix of a social interaction network, and $\mathbf{A}_{\boldsymbol{xy}}$ is the biadjacency matrix of a bipartite hazard damage-human interaction network. We make the following remarks on the model:

- **Main assumption**: An individual's emotional state is driven by social interactions and the severity of hazard damage, with α controlling the relative importance of these two drivers.
- **The first summation**: The emotional interaction is characterized by the sum of an empathy [20] term $(y_j - y_i)^2$ and an amplification-attenuation [14] term $-cy_iy_j$. If $c = 0$, the ground state of minimum energy favors y_i to align with the average of $\{y_j\}$ that influence the individual. If $c > 0$, risk amplification is triggered, as the ground state favors y_i to be more stressful than the average of $\{y_j\}$, suggesting that stressful emotions are more contagious, known as the negativity bias; while $c < 0$ suggests the opposite, risk attenuation.

- **The second summation**: The direct emotional impact of hazard damage is characterized by the sum of the squared differences between the damage states x_j and the emotional state y_i. As a result, the ground state favors an alignment between the physical damage and the emotional state, which is consistent with common sense. Amplification-attenuation terms are not introduced here because we assume that only emotional interactions may exhibit complex behaviors such as risk amplification[14].
- **Networks**: Two directed networks are encoded in the model: the social interaction network, characterized by an $N_y \times N_y$ adjacency matrix $\mathbf{A}_{\boldsymbol{yy}}$, and the hazard damage-human interaction network, characterized by an $N_x \times N_y$ biadjacency matrix $\mathbf{A}_{\boldsymbol{xy}}$. We define $\mathbf{A}_{\boldsymbol{yy}}(j,i) = 1$ if the emotional state y_j of the j-th individual affects the emotional state of the i-th individual, and $\mathbf{A}_{\boldsymbol{yy}}(j,i) = 0$ otherwise. Similarly, $\mathbf{A}_{\boldsymbol{xy}}(j,i) = 1$ if the damage state x_j affects the emotional state of the i-th individual.
- **Parsimony and homogeneity**: In principle, α and c should vary across individuals and pairs of individuals, and additional weights should be introduced into the first and second summations to account for the heterogeneity in the (y_j, y_i) and (x_j, y_i) interactions. However, we seek a parsimonious representation for effective parameter inference and prediction of macroscopic behaviors. Therefore, the heterogeneities are homogenized into global parameters (α, c).

Using the local Hamiltonian in Eq. (1), we formulate a Gibbs simulation model (Algorithm 1) for emotional states. This model generalizes the Boltzmann distribution[19] to systems with non-reciprocal interactions[21,22]. The initial configuration $\boldsymbol{y}^{(0)}$ is set to the integer part of the average damage exposure, i.e., $y_i^{(0)} = \lfloor \frac{\sum_{\mathbf{A}_{\boldsymbol{xy}}(j,i)=1} x_j}{\sum_{j=1}^{N_x} \mathbf{A}_{\boldsymbol{xy}}(j,i)} \rceil$, where $\lfloor \cdot \rceil$ denotes round to the nearest integer.

Algorithm 1 Gibbs Simulation Model for Emotional States

- Given the current configuration $\boldsymbol{y}^{(k)}$, randomly select $i \in \{1, 2, \ldots, N_y\}$ and compute its local Hamiltonian $\mathcal{H}_i$.
- Randomly perturb $y_i^{(k)}$ in $\boldsymbol{y}^{(k)}$ to obtain a proposal $\boldsymbol{y}'$, then compute its local Hamiltonian $\mathcal{H}_i'$ and $\Delta\mathcal{H}_i = \mathcal{H}_i' - \mathcal{H}_i$.
- Accept the proposal $\boldsymbol{y}^{(k+1)} \leftarrow \boldsymbol{y}'$, with probability $\min\{1, \exp(-\beta\Delta\mathcal{H}_i)\}$, where $\beta = 1/(k_B T)$, T is the thermodynamic temperature, and the Boltzmann constant is set to $k_B = 1$ throughout the paper. If $\boldsymbol{y}'$ is not accepted, $\boldsymbol{y}^{(k+1)} \leftarrow \boldsymbol{y}^{(k)}$.

As an approximation for analytical tractability, we use $\mathcal{H}_i$ to construct an effective Boltzmann distribution:

$$\begin{aligned} p_{\mathbf{Y}|\mathbf{X}}(\boldsymbol{y}|\boldsymbol{x}) =& \frac{1}{Z}\exp\left(-\beta\mathcal{H}\right) \\ =& \frac{1}{Z}\exp\left(-\beta\Big(\frac{\alpha}{2}\sum_{\substack{1\le i\le N_y \\ \mathbf{A}_{\boldsymbol{yy}}(j,i)=1}}((y_i-y_j)^2 - cy_iy_j) + (1-\alpha)\sum_{\substack{1\le i\le N_y \\ \mathbf{A}_{\boldsymbol{xy}}(j,i)=1}}(x_j-y_i)^2\Big)\right), \end{aligned} \tag{2}$$

where $\mathcal{H}$ is the system Hamiltonian and Z is the partition function. The Boltzmann distribution model is strictly consistent with the Gibbs simulation model when $\mathbf{A}_{\boldsymbol{yy}}$ is symmetric. In this context, the Hammersley-Clifford theorem[23] guarantees the form of Eq. (2), and the Gibbs simulation model simply performs Gibbs sampling for the Boltzmann distribution. However, when $\mathbf{A}_{\boldsymbol{yy}}$ is asymmetric, the Boltzmann model homogenizes the Gibbs simulation model by replacing non-reciprocal interactions with reciprocal ones and averaging directed interaction energies into undirected equivalents. As an approximation of reality, Eq. (2) can be reasonable when emotional interactions reach a steady state that closely mimics thermodynamic equilibrium. This occurs when there are no abrupt internal or external changes within the system during the time window of interest, and the emotional interactions relax rapidly. In this work, we employ the Gibbs simulation model for numerical simulations and the Boltzmann distribution model to derive analytical approximations.

To study emotional polarization within a population, we define the macroscopic quantity of interest, or order parameter, as the *emotional magnetization*: $m(\boldsymbol{y}) \coloneqq \sum_{i=1}^{N_y} \mathbb{1}(y_i)/N_y$, where $\mathbb{1}$ is a binary indicator function for stressful emotional states. Emotional magnetization can be interpreted as the proportion of the population that is emotionally stressed by the hazard. Focusing further on the binary states and following the Landau theory of phase transitions[19,24] (see *Methods and Materials* for details), we construct the mean-field system Hamiltonian for Eq. (2):

$$\mathcal{H}_{\text{MF}}\left[m(\boldsymbol{y})\right] = N_y\Big(-\frac{1}{2}\alpha c m^2\langle k\rangle_{\mathbf{A}_{\boldsymbol{yy}}} + (1-\alpha)m^2\langle k_{\boldsymbol{y}}\rangle_{\mathbf{A}_{\boldsymbol{xy}}} - 2(1-\alpha)m\langle x\rangle_{\mathbf{A}_{\boldsymbol{xy}}}\Big), \tag{3}$$

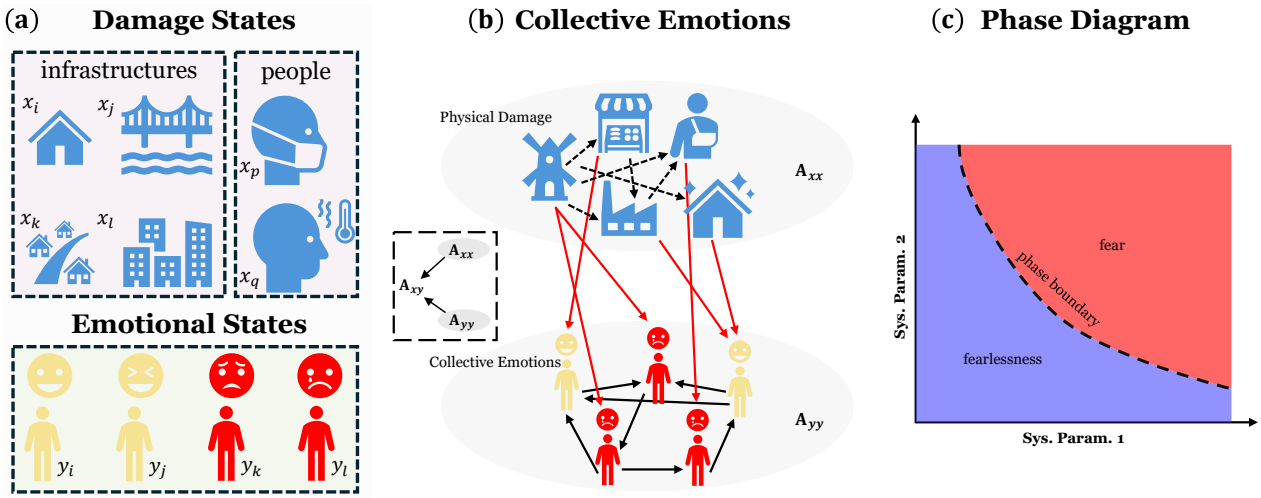

Figure 1: Illustration of collective emotional responses to hazards. Panel (a) illustrates that individuals' emotional states are influenced by both tangible damage states and the emotional states of others. **Panel (b)** shows a sample structure of the hazard damage–human interaction network, represented by $\mathbf{A}_{\boldsymbol{xy}}$, and the social interaction network, represented by $\mathbf{A}_{\boldsymbol{yy}}$. The intra-layer edges depict interactions among hazard damage (black dashed lines) and among individual emotions (black lines), while inter-layer edges (red lines) characterize the impact of hazard damage on emotions. This study focuses on intra-layer emotional interactions within the social network and inter-layer interactions between hazard damage and emotions, treating hazard damage as prior knowledge derived from domain-specific models and data. **Panel (c)** presents a conceptual phase diagram parameterized by global quantities such as the average network degree and average damage rate. The objective is to identify the critical factors that shape hazard-induced collective emotions and trigger sudden shifts (phase transitions) in the collective emotional states.

where $\langle k\rangle_{\mathbf{A}_{\boldsymbol{yy}}}$ represents the average in-degree of the social interaction network, $\langle k_{\boldsymbol{y}}\rangle_{\mathbf{A}_{\boldsymbol{xy}}}$ denotes the average in-degree of $\boldsymbol{y}$-nodes in the hazard damage-human interaction network, and $\langle x\rangle_{\mathbf{A}_{\boldsymbol{xy}}}$ represents the average total damage states affecting each individual's emotional state. Using the mean-field system Hamiltonian, the partition function is approximated by:

$$Z \approx N_y \int \mathrm{d}m \cdot \Omega\,(m) \exp\left(-\beta \mathcal{H}_{\mathrm{MF}}[m(\boldsymbol{y})]\right) = N_y \int_0^1 \exp\left(-\beta N_y f(m)\right) \mathrm{d}m\,, \tag{4}$$

where $\Omega\,(m) = \frac{N_y!}{(mN_y)!((1-m)N_y)!}$ is the volume of the phase space for a specific emotional magnetization m, and the free energy density $f(m)$ is derived as:

$$\begin{aligned} f(m) &= \beta\big((1-\alpha)\langle k_{\boldsymbol{y}}\rangle_{\mathbf{A}_{\boldsymbol{xy}}} - \frac{1}{2}\alpha c\langle k\rangle_{\mathbf{A}_{\boldsymbol{yy}}}\big)m^2 - 2\beta(1-\alpha)\langle x\rangle_{\mathbf{A}_{\boldsymbol{xy}}} m + m\ln m + (1-m)\ln(1-m) \\ &\propto -\beta A\big(m-\frac{1}{2}\big)^2 - \beta(A+B)\big(m-\frac{1}{2}\big) + m\ln m + (1-m)\ln(1-m), \end{aligned} \tag{5}$$

where the second line introduces two composite parameters, A and B, defined as follows:

$$A := -(1-\alpha)\langle k_{\boldsymbol{y}}\rangle_{\mathbf{A}_{\boldsymbol{xy}}} + \frac{1}{2}\alpha c\langle k\rangle_{\mathbf{A}_{\boldsymbol{yy}}}\,, \tag{6a}$$

$$B := 2(1-\alpha)\langle x_{\boldsymbol{y}}\rangle_{\mathbf{A}_{\boldsymbol{xy}}} \equiv 2(1-\alpha)p\langle k_{\boldsymbol{y}}\rangle_{\mathbf{A}_{\boldsymbol{xy}}}\,, \tag{6b}$$

where $p := \frac{\langle x\rangle_{\mathbf{A}_{\boldsymbol{xy}}}}{\langle k_{\boldsymbol{y}}\rangle_{\mathbf{A}_{\boldsymbol{xy}}}}$, A can be positive or negative, but B is always nonnegative. According to Landau theory, A acts as the coupling constant, while the combination $A+B$ represents the effective external field. The saddle point approximation for Eq. (4) leads to the self-consistency condition for the emotional magnetization:

$$\frac{\partial f(m)}{\partial m}\Big|_{m=\langle m\rangle} = 2\beta\big((1-\alpha)\langle k_{\boldsymbol{y}}\rangle_{\mathbf{A}_{\boldsymbol{xy}}} - \frac{1}{2}\alpha c\langle k\rangle_{\mathbf{A}_{\boldsymbol{yy}}}\big)\langle m\rangle - 2\beta(1-\alpha)\langle \boldsymbol{x}\rangle_{\mathbf{A}_{\boldsymbol{xy}}} + \ln\frac{\langle m\rangle}{1-\langle m\rangle} = 0\,. \tag{7}$$

We use the mean-field formulas to study the mechanisms of collective emotional response.

2.2 Application to COVID-19 Datasets in the United States

2.2.1 Background and Data Acquisition

In this section, we apply the proposed model to two datasets related to COVID-19 in the United States, representing emotional responses and epidemiological data for different U.S. states, covering August 2020 and December 2021. We use the Twitter/X follow graph[25] to represent the topology of the social interaction network. We incorporate contact patterns to construct the hazard damage-human interaction network, accounting for variations in household, workplace, and school contacts across different states, using data from the United Nations Population Division 2022. The average damage rate p is approximated by the virus prevalence rate, retrieved from the Center for Systems Science and Engineering at Johns Hopkins University[26]. Emotional data are obtained via sentiment classification of posts on Twitter/X using a fine-tuned large language model. Using the information retrieved above, we calibrate the parameters α and c for each U.S. state. To illustrate the insights provided by the proposed model, we also conduct simulated control experiments to explore strategies for mitigating collective stress.

2.2.2 Distribution of α and c Induced by COVID-19

We use the mean-field approximation and Bayesian parameter estimation to infer the posterior distribution of (α, c), as shown in Fig. 2. In the parameter inference, we assume that: (1) α and c remain stable across the two observed periods, and (2) the effect of inter-state transport is negligible. The first assumption is reasonable because α and c are intrinsic properties of a community and are unlikely to change significantly over a short timeframe. The second assumption is justified by the travel restrictions implemented during the COVID-19 pandemic. Recall that α represents the relative importance of social interaction over hazard damage, with $\alpha = 1$ indicating that social interactions dominate the emotional response. The parameter c quantifies the asymmetry between low- and high-stress emotions: $c > 0$ reflects negativity bias and risk amplification, while $c < 0$ indicates positivity bias and risk attenuation. Parameter inference results reveal that all states have an average $\alpha > 0.5$, with some states (e.g., DE, IA, MN, NE) exhibiting high values exceeding 0.8, highlighting the dominant influence of social interactions on the collective emotional response in the U.S. Additionally, all states show $c > 0$, confirming the prevalence of negativity bias. Significant negativity bias is observed in AK, HI, NH, and VA. Another observation is that α and c appear to be negatively correlated, with states exhibiting higher α values tending to have lower c values.

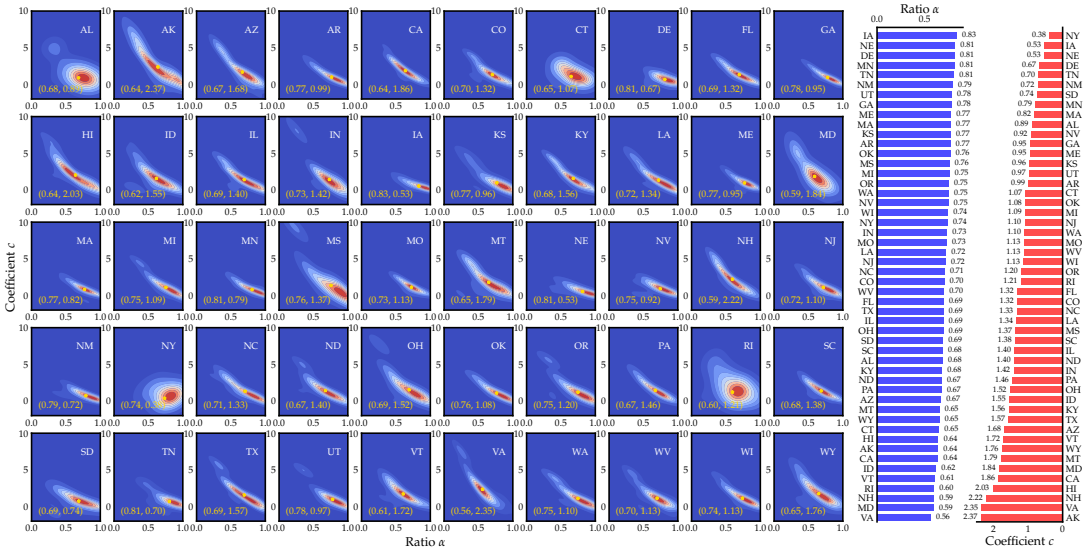

Figure 2: The joint posterior distributions of α and c for each state in the United States. The joint posterior distributions of α and c are obtained from Bayesian inference, accounting for both aleatory and epistemic uncertainties. Each subplot corresponds to a specific state, with contours representing the density of plausible parameter values. The yellow markers indicate the mean values of (α, c) for each state. The bar plots on the right display the mean values of α and c for each state, sorted in descending and ascending order, respectively.

References

[1] Maria Koliou, John W van de Lindt, Therese P McAllister, Bruce R Ellingwood, Maria Dillard, and Harvey Cutler. State of the research in community resilience: Progress and challenges. *Sustainable and resilient infrastructure*, 5 (3):131–151, 2020.

[2] Fikret Berkes and Helen Ross. Community resilience: Toward an integrated approach. *Society & natural resources*, 26(1):5–20, 2013.

[3] Hirooki Yabe, Yuriko Suzuki, Hirobumi Mashiko, Yoko Nakayama, Mitsuru Hisata, Shin-Ichi Niwa, Seiji Yasumura, Shunichi Yamashita, Kenji Kamiya, Masafumi Abe, et al. Psychological distress after the great east japan earthquake and fukushima daiichi nuclear power plant accident: results of a mental health and lifestyle survey through the fukushima health management survey in fy2011 and fy2012. *Fukushima journal of medical science*, 60(1):57–67, 2014.

[4] Rebecca M Schwartz, Cristina Sison, Samantha M Kerath, Lisa Murphy, Trista Breil, Daniel Sikavi, and Emanuela Taioli. The impact of hurricane sandy on the mental health of new york area residents. *American journal of disaster medicine*, 10(4):339–346, 2015.

[5] Rebecca M Schwartz, Stephanie Tuminello, Samantha M Kerath, Janelle Rios, Wil Lieberman-Cribbin, and Emanuela Taioli. Preliminary assessment of hurricane harvey exposures and mental health impact. *International journal of environmental research and public health*, 15(5):974, 2018.

[6] Wil Lieberman-Cribbin, Bian Liu, Samantha Schneider, Rebecca Schwartz, and Emanuela Taioli. Self-reported and fema flood exposure assessment after hurricane sandy: association with mental health outcomes. *PloS one*, 12 (1):e0170965, 2017.

[7] Ana Fernandez, John Black, Mairwen Jones, Leigh Wilson, Luis Salvador-Carulla, Thomas Astell-Burt, and Deborah Black. Flooding and mental health: a systematic mapping review. *PloS one*, 10(4):e0119929, 2015.

[8] Jonathan Laugharne, Gill Van de Watt, and Aleksandar Janca. After the fire: the mental health consequences of fire disasters. *Current opinion in psychiatry*, 24(1):72–77, 2011.

[9] AL Hansen, Peng Bi, Monika Nitschke, Philip Ryan, Dino Pisaniello, and Graeme Tucker. The effect of heatwaves on mental health in a temperate australian city. *Epidemiology*, 19(6):S85, 2008.

[10] Ana Luisa Pedrosa, Letícia Bitencourt, Ana Cláudia Fontoura Fróes, Maria Luíza Barreto Cazumbá, Ramon Gustavo Bernardino Campos, Stephanie Bruna Camilo Soares de Brito, and Ana Cristina Simões e Silva. Emotional, behavioral, and psychological impact of the covid-19 pandemic. *Frontiers in psychology*, 11:566212, 2020.

[11] Cuiyan Wang, Riyu Pan, Xiaoyang Wan, Yilin Tan, Linkang Xu, Cyrus S Ho, and Roger C Ho. Immediate psychological responses and associated factors during the initial stage of the 2019 coronavirus disease (covid-19) epidemic among the general population in china. *International journal of environmental research and public health*, 17(5):1729, 2020.

[12] Cass R Sunstein. *Republic. com*. Princeton university press, 2001.

[13] Michela Del Vicario, Gianna Vivaldo, Alessandro Bessi, Fabiana Zollo, Antonio Scala, Guido Caldarelli, and Walter Quattrociocchi. Echo chambers: Emotional contagion and group polarization on facebook. *Scientific reports*, 6(1):37825, 2016.

[14] Roger E Kasperson, Ortwin Renn, Paul Slovic, Halina S Brown, Jacque Emel, Robert Goble, Jeanne X Kasperson, and Samuel Ratick. The social amplification of risk: A conceptual framework. *Risk analysis*, 8(2):177–187, 1988.

[15] Hiroyuki Hikichi, Jun Aida, Toru Tsuboya, Katsunori Kondo, and Ichiro Kawachi. Can community social cohesion prevent posttraumatic stress disorder in the aftermath of a disaster? a natural experiment from the 2011 tohoku earthquake and tsunami. *American journal of epidemiology*, 183(10):902–910, 2016.

[16] Walter Cullen, Gautam Gulati, and Brendan D Kelly. Mental health in the covid-19 pandemic. *QJM: An International Journal of Medicine*, 113(5):311–312, 2020.

[17] Susan L Cutter, Christopher G Burton, and Christopher T Emrich. Disaster resilience indicators for benchmarking baseline conditions. *Journal of homeland security and emergency management*, 7(1), 2010.

[18] Fabian Baumann, Philipp Lorenz-Spreen, Igor M Sokolov, and Michele Starnini. Modeling echo chambers and polarization dynamics in social networks. *Physical Review Letters*, 124(4):048301, 2020.

[19] Lev Davidovich Landau and Evgenii Mikhailovich Lifshitz. *Statistical Physics: Volume 5*, volume 5. Elsevier, 2013.

[20] Mark H Davis. *Empathy: A social psychological approach*. Routledge, 2018.

[21] Alejandro D Sánchez, Juan M López, and Miguel A Rodriguez. Nonequilibrium phase transitions in directed small-world networks. *Physical review letters*, 88(4):048701, 2002.

[22] Adam Lipowski, António Luis Ferreira, Dorota Lipowska, and Krzysztof Gontarek. Phase transitions in ising models on directed networks. *Physical Review E*, 92(5):052811, 2015.

[23] Pierre Brémaud. *Markov chains: Gibbs fields, Monte Carlo simulation, and queues*, volume 31. Springer Science & Business Media, 2013.

[24] Igor S Aranson and Lorenz Kramer. The world of the complex ginzburg-landau equation. *Reviews of modern physics*, 74(1):99, 2002.

[25] Seth A Myers, Aneesh Sharma, Pankaj Gupta, and Jimmy Lin. Information network or social network? the structure of the twitter follow graph. In *Proceedings of the 23rd international conference on world wide web*, pages 493–498, 2014.

[26] Ensheng Dong, Hongru Du, and Lauren Gardner. An interactive web-based dashboard to track covid-19 in real time. *The Lancet infectious diseases*, 20(5):533–534, 2020.

Disclaimer

The opinions, findings, and conclusions or recommendations expressed in this publication are those of the author(s) and do not necessarily reflect the views of the study sponsor(s), the Pacific Earthquake Engineering Research Center, or the Regents of the University of California.

The Pacific Earthquake Engineering Research Center (PEER) is a multi-institutional research and education center with headquarters at the University of California, Berkeley. Investigators from over 20 universities, several consulting companies, and researchers at various state and federal government agencies contribute to research programs focused on performance-based earthquake engineering.

These research programs aim to identify and reduce the risks from major earthquakes to life safety and to the economy by including research in a wide variety of disciplines including structural and geotechnical engineering, geology/seismology, lifelines, transportation, architecture, economics, risk management, and public policy.

PEER is supported by federal, state, local, and regional agencies, together with industry partners.

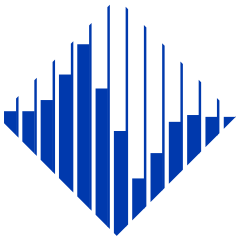

PEER Core Institutions

University of California, Berkeley (Lead Institution)
California Institute of Technology
Oregon State University
Stanford University
University of California, Davis
University of California, Irvine
University of California, Los Angeles
University of California, San Diego
University of Nevada, Reno
University of Southern California
University of Washington

Pacific Earthquake Engineering Research Center
University of California, Berkeley
325 Davis Hall, Mail Code 1792
Berkeley, CA 94720-1792
Tel: 510-642-3437
Email: peer_center@berkeley.edu

ISSN 2770-8314
https://doi.org/10.55461/VVLL8567